AN IN-SILICO STUDY OF THERMO-ACOUSTIC COMPUTED TOMOGRAPHY FOR EXTERNAL AND INTERNAL IMAGING GEOMETRY

By

SOVANLAL MUKHERJEE

Bachelor of Engineering in Electronics and
Communication Engineering
University of Burdwan
West Bengal, India
2002

Master of Technology in Electrical Engineering
Indian Institute of Technology, Kanpur
Kanpur, U.P., India
2005

Submitted to the Faculty of the
Graduate College of the
Oklahoma State University
in partial fulfillment of
the requirements for
the Degree of
DOCTOR OF PHILOSOPHY
December, 2013

AN IN-SILICO STUDY OF THERMO-ACOUSTIC COMPUTED TOMOGRAPHY FOR EXTERNAL AND INTERNAL IMAGING GEOMETRY

Dissertation Approved:

Dr. Charles Bunting

Dissertation Adviser

Dr. Daqing Piao

Dr. James C. West

Dr. Arvind Santhanakrishnan

ACKNOWLEDGEMENTS

First of all, I would like to express my deepest gratitude to my Dissertation adviser Dr. Charles Bunting for his continuous support and help throughout my Ph.D. work. It's been a wonderful experience for me working with Dr. Bunting as he is the most enthusiastic and of course the friendliest adviser I have ever had. I am really proud to have him as my mentor who consistently encouraged me to achieve my research goals.

I would like to thank my Dissertation co-adviser Dr. Daqing Piao for his in-depth knowledge in biomedical field that helped me understand the concepts of thermo-acoustic tomography. I am really grateful to him for all the valuable suggestions that he provided to me throughout my Ph.D. work.

I would like to thank my committee member Dr. James C. West for his guidance and encouragement that helped me learn Electromagnetics and numerical methods. I am also grateful to Dr. Santhanakrishnan for all his valuable feedbacks and for considering being my committee member in spite of a very short notice from me.

I would also like to thank my lab mates Q, Gary and Andrew for all valuable technical discussions, my friends Nitin, Rahul, Ashok, Corey, Logan, David and Fahad for making my staying at OSU exciting.

Last but not the least, I am indebted to my parents, my elder brother, sister-in-law and my cute nephew "Nick" for their love, support and encouragement that made me think about earning a Ph.D.

Name: SOVANLAL MUKHERJEE

Date of Degree: December, 2013

Title of Study: AN IN-SILICO STUDY OF THERMO-ACOUSTIC COMPUTED TOMOGRAPHY FOR EXTERNAL AND INTERNAL IMAGING GEOMETRY

Major Field: ELECTRICAL ENGINEERING

Abstract: This work investigates a complete forward and inverse model of thermo-acoustic computed tomography (TACT) for the reconstruction of electrical conductivity distribution within an external and internal imaging geometry. The external imaging geometry that resembles a geometry used for the breast cancer detection and the internal imaging geometry that resembles a geometry used for the prostate cancer detection is illuminated by an electromagnetic (EM) source at a microwave frequency and the generated acoustic wave within the geometry due to EM illumination is detected by an array of ultrasonic transducers. From the detected acoustic wave, the absorbed energy density profile within the geometry and hence the electrical conductivity which is directly related to the energy density is reconstructed. It has been well proved that cancerous tissue exhibits different conductivity profile from normal tissue due to different concentration of ions and water in the cancerous tissue. As a result of this, cancerous tissue absorbs microwave energy differently and a reconstructed image based on an absorbed microwave energy density or conductivity profile can give a precise location of the cancerous tissue. A finite element method (FEM) based complete reconstruction algorithm is investigated and various simulated reconstructed images based on different conductivity profile between cancerous and normal tissue are shown.

TABLE OF CONTENTS

Chapter Page

Chapter Page

LIST OF TABLES

Table Page

Table Page

LIST OF FIGURES

Figure Page

Figure Page

Figure Page

Figure Page

Figure Page

Figure Page

CHAPTER I

INTRODUCTION

1.1. Background

Recently, medical imaging modalities have seen significant attention for the diagnosis of the cancerous tissues inside human body. One crucial advantage of the medical imaging technique relies on the fact that it is non-invasive and therefore does not involve any physical penetration of the skin. Some common medical imaging modalities include X-ray mammography, ultrasound imaging (or Ultrasonography), X-ray computed tomography (CT) and magnetic resonance imaging (MRI). Other imaging modalities such as diffuse optical tomography (DOT) [1], microwave imaging [2, 3], Thermo/Photo-acoustic tomography (TAT/PAT) [4, 5] are emerging as a promising new addition to the existing medical imaging techniques.

Various non-invasive medical imaging modalities stated above have successfully been applied for imaging breast [6-9] and prostate cancer [10, 11] which is the leading cause of death in the United States [12]. Each imaging modality has its own unique advantages and limitations. For example, X-ray mammography that uses ionizing X-ray radiation to create images of human breast has widely been used for detecting early breast cancer, but the rate of "false-negative" and "false-positive" cases in mammography is quite high [13] and the radiation exposure can be excessive to human body [13]. Figure 1.1 shows a mammographic image of human breast tumor. Ultrasonography which is an ultrasound based medical imaging modality gives a high resolution but low contrast images

of human tissues [14]. Figure 1.2 shows ultrasonic images of a breast cyst and prostate tumor. X-ray computed tomography (CT) that utilizes computer-processed low-energy X-rays, produces the high-contrast 3D cross-sectional images or "slices" of specific part of human body but suffers from low to moderate resolution and the "blurring" of object boundaries [15]. Magnetic resonance imaging or MRI that uses a high intensity magnetic field and the pulses of radio wave energy [16] to provide the images of internal organs of human body provides a good contrast of soft tissues and has widely been used to image brain and breast tumors, blood vessels, prostate tumor etc. The limitation of MRI is its low "sensitivity" i.e. probability of a positive test is low [16].

Recently introduced optical imaging modality like diffuse optical tomography (DOT) exploits high absorption rate of near-infrared (NIR) (wavelength of 600-1000 nm) light by oxygenated and deoxygenated hemoglobin [1, 6] to provide high contrast images of cancerous cells. Since blood concentration in cancerous tissues is considerably higher than in normal tissues, DOT provides a good contrast between cancerous and normal cells. Microwave imaging which exploits the dielectric properties (i.e. relative permittivity and electrical conductivity) of cancerous tissues [2, 3] also provides high contrast images of cancerous tissues. Both DOT and microwave imaging provide high contrast images but suffer from low resolution.

Thermo-acoustic computed tomography (CT), also known as Microwave-induced thermo-acoustic tomography (MI-TAT) or simply thermo-acoustic tomography (TAT) is an emerging medical imaging modality that combines both microwave and ultrasound imaging [5, 8] to provide a high-contrast and high-resolution images of cancerous cells. This dissertation primarily focuses on MI-TAT for developing an image reconstruction algorithm for a potential application in breast and prostate cancer imaging. It begins with introducing the fundamental concepts of MI-TAT and then delves into the details of the image reconstruction algorithm.

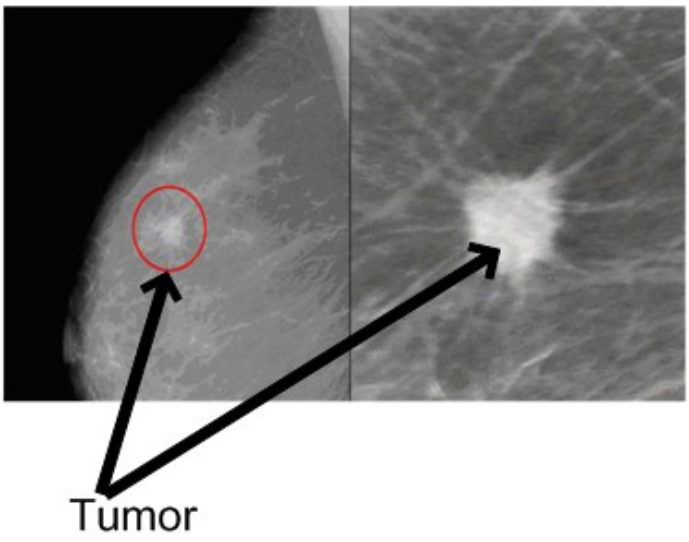

Figure 1.1 Mammographic image of breast tumor [13].

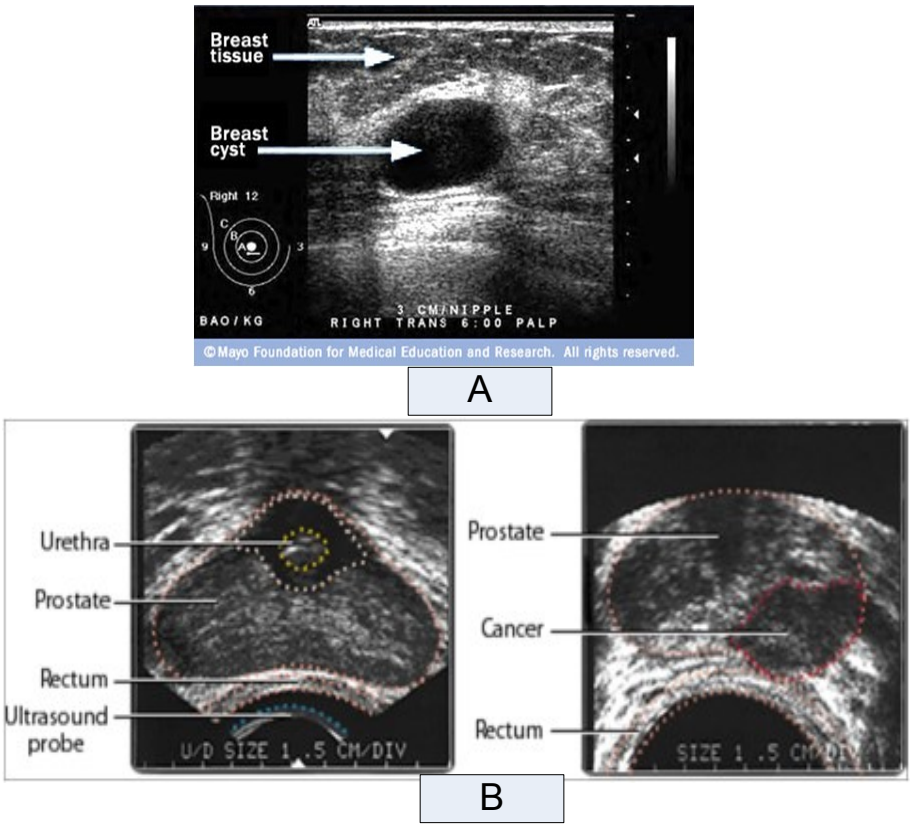

Figure 1.2.A Ultrasonic image of breast cyst [14].

Figure 1.2.B Ultrasonic image of Prostate cancer [17].

1.2. Thermo-acoustic computed tomography (CT): An overview

Thermo-acoustic computed tomography (CT) or microwave-induced thermo-acoustic tomography (MI-TAT) or simply thermo-acoustic tomography (TAT) is an emerging non-invasive medical imaging modality that combines the potentially high contrast of microwave imaging with the high resolution rendered by the ultrasound imaging [5,8]. In TAT, the biological tissues are irradiated by short pulses of microwave energy. The absorption of the microwave energy causes a thermo-elastic expansion of the tissues which in turn results in transient pressure rise inside the tissues. This rise in pressure propagates as an acoustic wave that originates from the location of the microwave absorption. This phenomenon is shown in figure 1.3. The detection of this ultrasonic/acoustic wave by ultrasonic receivers can give crucial functional and morphological information about the tissues. As malignant tissue differs from normal tissue in dielectric properties (e.g. malignant tissue usually possesses more electrical conductivity) as a result of differences in ion concentrations and water content, malignant tissue absorbs microwave energy differently [18] from normal tissue. Microwave-induced thermo-acoustic tomography (MI-TAT) exploits this different energy absorption characteristic to reveal a contrast between malignant and normal tissues, as having been manifested for breast cancer detection [5, 8] and brain imaging [19].

In MI-TAT, the acoustic signal detected by the ultrasonic receivers is used to reconstruct the distribution of the absorbed energy within the irradiated tissue. Since malignant tissue absorbs more microwave energy than normal tissue, a reconstructed image based on the contrast of the absorbed energy density profile can show a precise location of the malignant tissue. This thesis primarily focuses on applying MI-TAT on two kinds of geometries namely external imaging geometry which is most commonly used for breast cancer imaging and internal or trans-rectal imaging geometry which is commonly used for prostate cancer imaging.

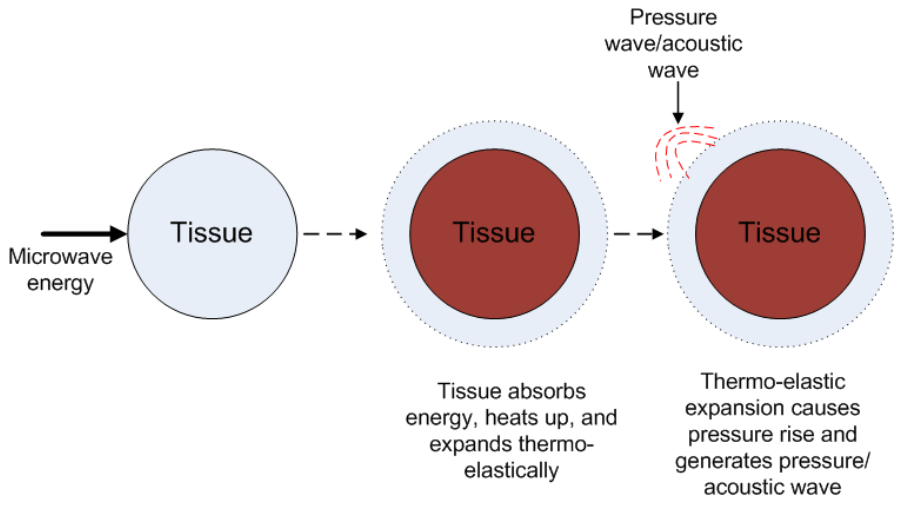

Figure 1.3 Schematic illustration of thermo-acoustic phenomenon

MI-TAT for external imaging geometry (Fig. 1.4) and internal or trans-rectal imaging geometry (Fig. 1.5) differs in two ways. First, in external imaging geometry, an externally applied electromagnetic (EM) plane wave that is incident on the external boundary of the geometry uniformly illuminates the entire surface of the imaging medium, while in trans-rectal or internal imaging geometry, the EM source is likely arranged as a point-source inside the geometry and therefore the illumination of the medium is non-uniform and position or depth dependent with respect to the irradiating source. Second, in external imaging geometry, the acoustic detectors/receivers are placed as an array across the external boundary of the geometry and enclose the object to be imaged and therefore every receiver can actually "see" the object, while in trans-rectal geometry, the receivers are placed as an array on a convex boundary that is located below the object and therefore the visibility of the object by the receivers is limited.

In this study, a MI-TAT based algorithm for the reconstruction of the power loss density in external and internal imaging geometry is developed. The electrical conductivity distribution is decoupled from the reconstructed power loss density by computing the electrical field in the given geometry.

1.3. Motivation behind the work

TAT has been explored extensively for breast cancer study [5, 7, 8] but no TAT based work has been reported so far for reconstructing the conductivity distribution in a prostate-like geometry. Applying microwave induced thermo-acoustic tomography (MI-TAT) in an internal or trans-rectal imaging geometry has an ultimate goal of imaging the cancerous human prostate. Prostate cancer is the most common non-dermatologic cancer in American men with 238,590 estimated new cases and 29,720 estimated deaths reported in the United States in 2013[12]. Prostate cancer screening is usually performed by the measurement of serum prostate-specific antigen (PSA) [20], digital rectal examination (DRE) or by the combination both these tests [21]. When PSA values are elevated or the outcome of the DRE is abnormal, trans-rectal ultrasound (TRUS) guided needle biopsy is usually performed. The biopsy protocol includes 10 to 12 samples of tissue obtained throughout the prostate for the initial assessment [22]. However, prostate biopsy usually has a low diagnostic yield and if a persistent prostate cancer is suspected after negative biopsies, more extensive biopsies (up to 24 samples of tissue) are performed as necessary assessment procedure [23].

Enhancing the specificity of imaging guidance to the biopsy, such as augmenting the high ultrasonic resolution that TRUS provides with a high imaging contrast that microwave imaging [2, 3] could render, provides the potential to improve the biopsy yield. As MI-TAT provides a high tissue-contrast of microwave absorption at a resolution limited by acoustics [5, 8], it could become an alternative imaging mechanism for prostate cancer detection. In this simulation study, MI-TAT is explored for the first time for reconstructing the electrical conductivity distribution in a trans-rectal geometry for a potential application of prostate cancer imaging.

1.4. Review of literatures

Thermo-acoustic effect was first introduced by Alexander Graham Bell in 1880 [24]. During his experiment, Bell et al. observed that an audible acoustic wave could be created by illuminating sunlight intermittently onto a rubber sheet. Thermo-acoustic effect in biological tissues was first reported by Bowen et al. [25]. Bowen et al. studied the absorption properties of human tissues that were exposed to electromagnetic radiation. Since the invention of thermo-acoustic effect, microwave-induced thermo-acoustics was explored by several investigators in the 1980's for imaging of biological tissues [26-30].But these early works did not produce any tomographic images. Thermo-acoustic tomography was first introduced by Kruger et al. [5] as an imaging modality that combines ultrasound imaging to give a high resolution and microwave imaging to give high contrast images of cancerous cells. Later Kruger et al. [8] explored thermo-acoustic computed tomography for in-vivo breast cancer imaging. Thermo-acoustic tomography generates images based on the map of local EM energy deposition in the object to be imaged [5] and usually operates in the range of 434 MHz- 3 GHz.

Since the invention of the thermo-acoustic tomography, it was explored by various investigators for breast [5, 7, 8] and brain [19] and prostate [31] imaging. It has been well proved that the electrical conductivity of malignant or cancerous cells is considerably different from normal cells [32, 33]. *Ex vivo* studies at RF spectra (up to 3 GHz) have demonstrated a contrast of 4:1 to 6:1 in tissue conductivity between malignant and normal tissues, of breast [34]. A recent large-scale study has shown that the electrical conductivity contrast between malignant tissue and normal adipose dominated tissue, of breast, is as large as 10:1 [35]. Because of different conductivity profile, malignant tissues usually absorb EM energy differently from normal tissues when illuminated by EM source and give a contrast for thermo-acoustic image.

Because of its capability for producing high-contrast and high-resolution images, much effort has been made to explore the theoretical and experimental applicability of thermo-acoustic tomography. Xu et al. showed the analytical solution of frequency-domain thermo-acoustic tomography (TAT) for a planar [36], cylindrical [37] and time-domain TAT for spherical [38] external imaging geometry for an application in breast cancer imaging. Mukherjee et al. [39] explored the analytical solution of frequency-domain TAT for a trans-rectal imaging geometry for a potential application of prostate cancer imaging. Yao et al. [7] showed a finite element method (FEM) based TAT image reconstruction algorithm for reconstructing heterogeneous conductivity distribution inside an external imaging geometry. Huang et al. [40] showed an experimental demonstration of conductivity reconstruction based on the algorithm developed by Yao. Mukherjee et al. [41] demonstrated a FEM based algorithm for reconstructing heterogeneous conductivity distribution in a trans-rectal imaging geometry. Zhang et al. [42] and Zhu et al. [43] explored a finite-difference time-domain (FDTD) based TAT image reconstruction algorithm.

Photo-acoustic tomography (PAT) [44] or Opto-acoustic tomography (OAT) [45] is a general form of thermo-acoustic tomography (TAT) when the illuminating source is purely optical (e.g. LASER). PAT/OAT exploits different optical absorption characteristics of malignant and normal tissue for imaging contrast and was explored for imaging biological tissues as well. Wang et al. [46] demonstrated laser-induced PAT for in-vivo imaging of rat brain. Kolkman et al. [47] explored PAT for imaging blood vessels on human wrist. Wang et al. [48] provided experimental demonstration of PAT for a canine prostate imaging. Jiang et al. [49] developed a FEM based image reconstruction algorithm of PAT pertaining to an external imaging geometry for application in breast cancer imaging.

1.5. Novelty of the work

Although thermo-acoustic and photo-acoustic tomography was explored extensively for imaging the biological tissues of various human organs as described by the literatures in the previous section, the application of thermo-acoustic tomography (TAT) for reconstructing conductivity distribution in a prostate-like geometry was never explored and remains an open topic for the research. In this study, TAT for trans-rectal geometry is explored for the first time for a potential application of prostate cancer imaging. The geometry is illuminated by an EM point-source and the generated electric field (E-field) and the acoustic pressure inside the geometry due to EM illumination is computed. The finite element method (FEM) is adopted as a numerical tool for solving the scalar wave equation and thermo-acoustic wave equation to compute the E-field and acoustic pressure respectively. The numerically computed E-field is validated with the Green's function solution [50]. Various reconstructed images with the objects of different sizes and at different depths are shown. The percentage error between the true and reconstructed conductivity of the object is computed. The effect of various levels of Gaussian noise on the reconstructed images is explored. The contrast-to-noise ratio (CNR) which is an important parameter for determining the detectability [51] of an object is also computed. Finally, certain limitations of the presented work with respect to the reconstruction of the deeper objects are discussed.

1.6. Microwave-induced thermo-acoustic tomography (MI-TAT) for external and internal imaging geometry

In this section, two types of imaging geometries namely external imaging and internal imaging geometry are defined. These geometries are used for TAT based reconstruction of the electrical conductivity in a breast [7] and prostate-like geometry [41] respectively.

1.6.1. External imaging geometry

Figure 1.4 shows an external imaging geometry with a target or object located at a certain distance from the center of the geometry. The target and background can be considered as malignant and normal tissue and characterized by their relative dielectric constant and conductivity as $(\varepsilon_r, \sigma_1)$ and $(\varepsilon_r, \sigma_2)$ respectively. The heterogeneity of conductivity ($\sigma_1 > \sigma_2$) between the target and background reveals a contrast between the malignant (σ_1) and normal tissue (σ_2) respectively. In this study, ε_r is considered as 80 and σ_1, σ_2 is considered as 0.3 S/m and 0.1 S/m respectively for the external imaging geometry according to the literature [7]. The geometry is illuminated by an incident electromagnetic (EM) plane wave which is impinging upon the external boundary of the geometry. The illumination by an electromagnetic (EM) wave gives rise to the acoustic wave due to the thermal expansion and is detected by various acoustic/ultrasonic detectors that are placed uniformly across the boundary of the geometry. From the detected acoustic wave, the absorbed power density profile and hence the conductivity can be reconstructed. This geometry is used for imaging breast cancer [5, 7].

1.6.2 Internal or trans-rectal imaging geometry

Figure 1.5 shows an internal imaging or trans-rectal imaging geometry. The geometry is illuminated by an EM point-source which is located on a convex boundary as shown in the figure. A target is located on top of the convex boundary. The target and background is characterized by their relative permittivity and conductivity as $(\varepsilon_r, \sigma_1)$ and $(\varepsilon_r, \sigma_2)$ respectively. As for external imaging geometry, the heterogeneity of conductivity ($\sigma_1 < \sigma_2$) between the target and background reveals a contrast between the malignant (σ_1) and normal tissue (σ_2).In this study, ε_r is considered as 60.5 and σ_1, σ_2 is considered as 0.608 S/m and 1.216 S/m respectively. This permittivity and conductivity is chosen according to the data reported [52] for a normal human

prostate at 915MHz. The detailed criterion for selecting these parameters is discussed in chapter VI.

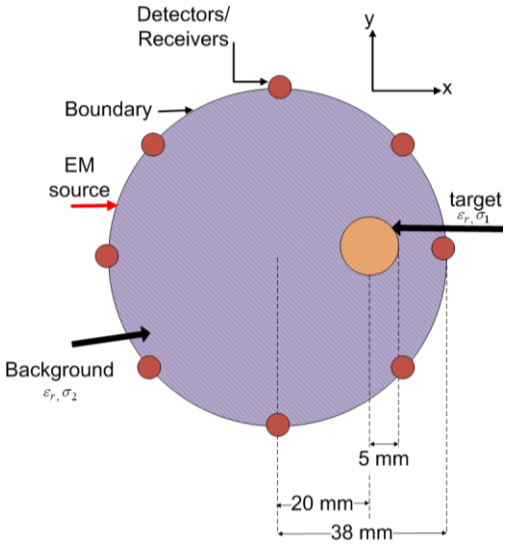

Figure 1.4: External-imaging geometry

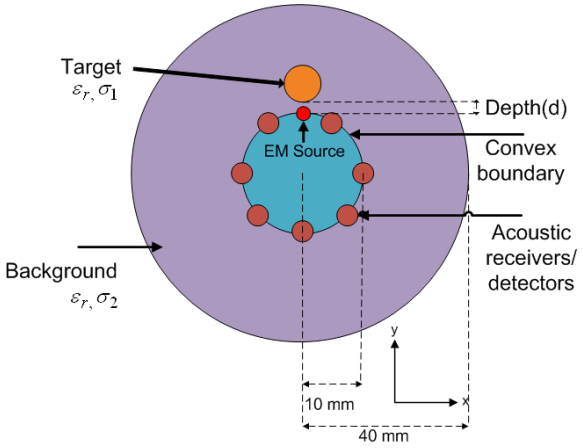

Figure 1.5: Internal or trans-rectal imaging geometry

A convex array of ultrasonic detectors that detect the acoustic wave generated inside the geometry as a result of EM illumination are placed along the convex region that is located below the target. From the detected acoustic wave, the absorbed power density profile and hence the electrical conductivity within the geometry can be reconstructed. This geometry set-up has a potential application for imaging prostate cancer.

1.7. Steps of complete reconstruction algorithm of MI-TAT for reconstructing conductivity profile

Reconstructing the conductivity distribution using MI-TAT involves multiple steps and the steps can be divided into three major tasks 1. "Measure" the true acoustic pressure 2. The forward problem 3. The inverse problem. Each major step includes various sub-steps that are described below.

1. "Measure" the true acoustic pressure

Measuring the true acoustic pressure involves the following sub-steps :

A. Set the true conductivity profile σ^m for the target/object and background.

B. Solve the scalar wave equation to find E-field E_z^m using set conductivity profile σ^m .

C. Calculate the power loss density s^m using $s^m = \sigma^m \left| E_z^m \right|^2$.

D. Solve the thermo-acoustic wave equation using s^m to calculate the true or "measured" acoustic pressure p_t^m in time-domain.

E. Add some random noise to the true acoustic pressure.

2. Forward problem

The forward problem of MI-TAT reconstruction algorithm includes following sub-steps:

A. Initialize conductivity σ_o .

B. Solve the scalar wave equation using σ_o to find E-field E_z^c .

C. Calculate the power loss density s^c using $s^c = \sigma_0 \left| E_z^c \right|^2$.

D. Solve the thermo-acoustic wave equation using s^c to find calculated acoustic pressure p_t^c in time domain.

3. Inverse problem

The inverse problem of the reconstruction algorithm has following sub-steps:

A. Calculate the "Jacobian" or "Sensitivity" matrix and reconstruct the power loss density s and conductivity σ.

B. Compare σ^m and σ . If the rms error is sufficiently small, the power loss density and hence the conductivity is reconstructed or update σ_o using $\sigma_o = \frac{s}{\left|E_z^c\right|^2}$ and continue steps (2)-(3) until a small error is achieved.

Figure 1.6 shows the steps described above in a flow diagram.

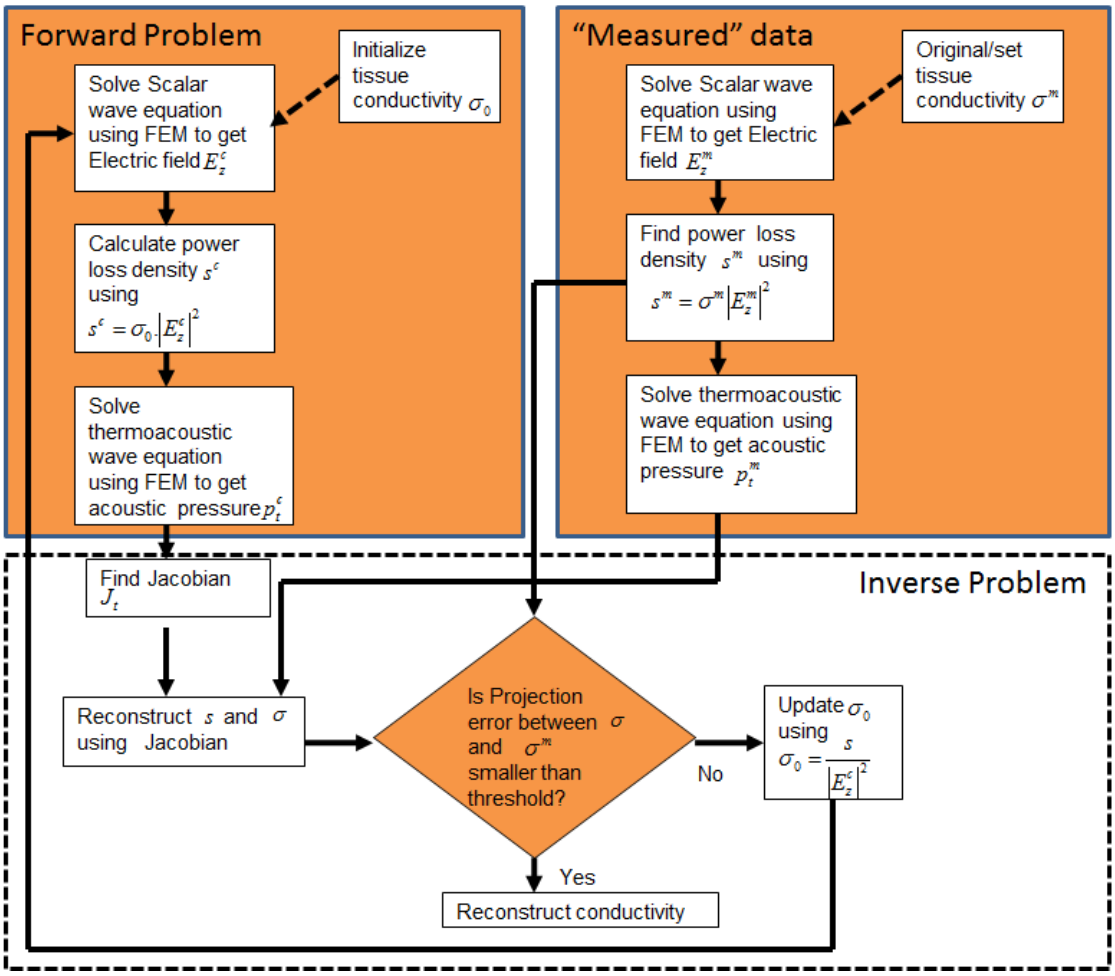

Fig. 1.6 Flow diagram of reconstruction algorithm of MI-TAT

1.8. Organization of the Thesis

This thesis is organized as follows. Chapter II describes the scattering analysis of electromagnetic (EM) wave from an external imaging geometry. This chapter shows the solution of the scalar EM wave equation to find the total E-field inside the external imaging geometry. A lossy dielectric cylinder is considered as an external imaging geometry. The dielectric cylinder is illuminated by an EM plane wave that is incident on the external boundary of the dielectric. The finite element method (FEM) along with Bayliss-Turkel absorbing boundary condition (ABC) is used for the computational purpose. The FEM solution is validated with the analytical solution for two standard geometries namely a single lossy dielectric cylinder and a concentric lossy dielectric cylinder. Chapter III discusses the solution of the thermo-acoustic wave equation using FEM to find the acoustic pressure generated inside the external imaging geometry. The solution of the acoustic pressure is shown at four different receiver locations placed along the boundary of the geometry. Chapter IV describes the computation of "Jacobian" matrix and shows various reconstructed images pertaining to the external imaging geometry. Chapter V shows the solution of the total E-field in an internal imaging geometry. The geometry is illuminated a by an EM point-source located on a convex boundary that is internal to the geometry. The finite element method (FEM) along with absorbing boundary condition is used for solving E-field inside the geometry. The procedure for solving E-field inside an external and internal imaging geometry differs in the position and type of the EM source. The FEM solution of the E-field is validated with the analytical solution for a standard homogeneous geometry with the same relative permittivity and conductivity considered everywhere throughout the geometry. Chapter V also discusses the solution of the acoustic pressure in an internal imaging geometry and shows the solution of the acoustic pressure at three different receivers placed on the convex boundary. Chapter VI shows various reconstructed images along with the line profiles of the true and reconstructed conductivity pertaining to internal imaging geometry. Various reconstructed images for both single and double objects at different

depths are shown. A contrast-to-noise ratio (CNR) plot is also shown for an object of different diameters and with a varying ratio of conductivity between the object and background. Chapter VI also points out the future works, challenges and limitations pertaining to the presented work. Appendix is given at the end of the thesis. Appendix describes the analytical solutions of different integrals resulted as a part of the finite element method, the analytical solutions of the total E-field inside a single lossy and a concentric lossy dielectric cylinder. Various MATLAB® codes are also included in the appendix.

CHAPTER II

SCATTERING OF ELECTROMAGNETIC WAVE FROM AN EXTERNAL IMAGING GEOMETRY

2.1. Introduction

The initial step of reconstructing the conductivity distribution in an imaging geometry (external or internal) using TAT is to solve for the absorbed Electric field (E-field) inside the geometry by as described in section 1.7 of chapter I. The E-field is usually computed by solving the scalar EM wave equation in a chosen computational domain (external or internal imaging geometry in this study) using an appropriate computational method. The electromagnetic (EM) wave that impinges on a geometry subjects to the scattering and the geometry serves as a scatterer. Total E-field inside the geometry can be represented by a sum of the incident E-field and the scattered E-field. This chapter investigates the scattering of an EM wave from an external imaging geometry illuminated by a TM^z plane wave. The scattering of EM wave from an external imaging geometry can be considered as the scattering from a lossy dielectric cylinder. The scattering from dielectric cylinders has been an important research topic for so many years and explored by various researchers. Some of them include the scattering from a dielectric cylinder of arbitrary cross-sections by Richmond et al. [53], the scattering of a TM plane wave from a lossless dielectric cylinder and a dielectric coated conducting cylinder of circular cross-section by Peterson et al. [54]. In this work, the scattering from lossy dielectric cylinders of circular cross-

section is considered and total E-field inside the dielectric is solved. This serves the purpose of solving steps 1-(B) and (C) and 2-(B) and (C) of section 1.7 in chapter I. The E-field solution is shown for four different geometries namely, 1. A single lossy dielectric cylinder 2. Two layered concentric lossy dielectric cylinder 3. Two layered lossy dielectric cylinder with an offset inner dielectric 4. Two layered lossy dielectric cylinder with two inner dielectrics-one at the center and another offset from the center. The finite element method (FEM) along with the Bayliss-Turkel absorbing boundary condition (ABC) [55] is applied for calculating the E-field.

2.2. Vector and scalar wave equation

The electromagnetic wave propagation through a medium characterized by a relative permittivity ε_r and permeability μ_r satisfies the following vector wave equation [56-59]

$$\nabla(\nabla \bullet \vec{E}(\vec{r},t)) - \nabla^2 \vec{E}(\vec{r},t) + \frac{1}{c^2}\mu_r \varepsilon_r \frac{\partial^2 \vec{E}(\vec{r},t)}{\partial t^2} = -\mu_0 \mu_r \frac{\partial J_i(\vec{r},t)}{\partial t} \tag{2.1}$$

For an electrical charge-free and homogeneous medium,

$$\varepsilon_0 \varepsilon_r (\nabla \bullet \vec{E}(\vec{r},t)) = 0 \tag{2.2}$$

Using (2.2), equation (2.1) can be written as,

$$\frac{1}{\mu_r}\nabla^2 \vec{E}(\vec{r},t) - \frac{1}{c^2}\varepsilon_r \frac{\partial^2 \vec{E}(\vec{r},t)}{\partial t^2} = \mu_0 \frac{\partial \vec{J}_i(\vec{r},t)}{\partial t} \tag{2.3}$$

In equation (2.1)-(2.3), $\vec{E}(\vec{r},t)$ is the electric field at position $\vec{r}$ and time t, c is the speed of light through free space (3 x 10^8 m/s), μ_0 is the permeability of free space (4π x 10^{-7} H/m) and $\vec{J}_i(\vec{r},t)$ is the excitation electric current density (A/m^2) at position $\vec{r}$ and time t.

Changing equation (2.3) from time-domain to frequency domain and considering TM^z propagation through a homogeneous medium, vector equation (2.3) can be transformed to a scalar wave equation as

$$\frac{1}{\mu_r}\nabla^2 E_z(\vec{r}) + k_0^2 \varepsilon_r E_z(\vec{r}) = j\omega\mu_0 J_{iz}(\vec{r}) \tag{2.4}$$

In equation (2.4), k_0 is the wave-number (m^{-1}) of free space= $\frac{\omega}{c}$ and ω is the radian frequency (rad/sec).

For a medium with dielectric losses and with finite conductivity σ S/m, equation (2.4) can be modified as

$$\frac{1}{\mu_r}\nabla^2 E_z(\vec{r}) + k^2 E_z(\vec{r}) = j\omega\mu_0 J_{iz}(\vec{r}) \tag{2.5}$$

Where $k = k_0\sqrt{\varepsilon_c}$ and ε_c = complex permittivity = $\varepsilon_r - j\frac{\sigma}{\omega\varepsilon_0}$

Equation (2.5) is known as the scalar EM wave equation and to be used for solving the E-field E_z

2.3. Weak form of the scalar wave equation [57]

In this section, a weak form of the scalar wave equation obtained in the previous section is constructed. Developing weak form of any equation is the first step of finite element solution process of the same equation.

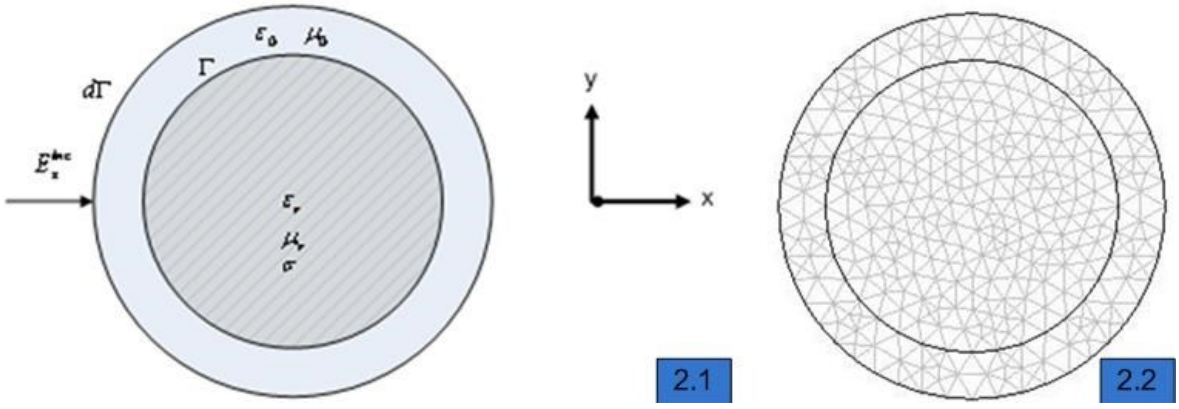

Fig 2.1. Cross section of a dielectric cylinder (ε_r, μ_r, σ) illuminated by TM wave. Fig 2.2 2D FEM mesh of a dielectric cylinder

A cylindrical lossy dielectric scatterer characterized by a relative permittivity ε_r , permeability μ_r and conductivity σ is considered as a computational domain for solving the E-field and is shown in figure 2.1. The scatterer is illuminated by a normally incident TM^z plane wave E_z^{inc} . The scalar wave equation (2.5) holds throughout region Γ containing the scatterer and must be augmented with a boundary condition on the surface $d\Gamma$ as shown in Figure 2.1 for obtaining a complete solution. The boundary conditions on $d\Gamma$ serve to couple the incident field into the FEM formulation of equation (2.5) and to ensure that the scattered field represents an outward-propagating solution [57]. Equation (2.5) is a "strong" form of the scalar wave equation as the unknown E-field appears within a second-order differential operator (∇^2). To make this equation more amenable to the numerical solution, it can be converted to a "weak" form by multiplying both sides of equation (2.5) by a weighting or testing function W_m and performing integration over surface Γ [57]. This gives rise to

$$\iint_{\Gamma} \frac{1}{\mu_r} W_m(\vec{r})(\nabla \bullet \nabla E_z(\vec{r}) + k^2 E_z(\vec{r}))ds = j\omega\mu_0 \iint_{\Gamma} W_m(\vec{r}) J_{iz}(\vec{r})ds \tag{2.6}$$

Using Vector identity

$$W_m \nabla \bullet \overline{A} = \nabla \bullet (W_m \overline{A}) - \nabla W_m \bullet \overline{A} \tag{2.7}$$

and Gauss's divergence theorem

$$\iint_{\Gamma} \nabla \bullet \overline{A} ds = \oint_{d\Gamma} \overline{A} \bullet \hat{n} dl \tag{2.8}$$

equation (2.6) can be simplified to

$$\iint_{\Gamma} (\frac{1}{\mu_r} \nabla W_m \bullet \nabla E_z - k^2 W_m E_z)ds = \oint_{\partial\Gamma} \frac{1}{\mu_r} W_m \frac{\partial E_z}{\partial n} dl - j\omega\mu_0 \iint_{\Gamma} W_m J_{iz} ds \tag{2.9}$$

In equation (2.9), $\vec{r}$ is omitted from $W_m(\vec{r})$, $E_z(\vec{r})$ and $J_{iz}(\vec{r})$ for simplicity. Equation (2.9) is known as the "weak" form of the scalar wave equation as now the order of differentiation of unknown E- field is less than that of the original scalar wave equation (2.5).

2.4. Finite element formulation of the scalar wave equation: A Galerkin's approach [57,60-62]

This section describes the finite element formulation of the scalar wave equation for a 2D geometry. The finite element method (FEM) is a numerical technique for obtaining approximate solutions to the boundary-value problems. In this method, the computational domain is discretized into elements of simple shapes e.g. triangle for 2D and tetrahedron for 3D domain. Appropriate interpolation functions also known as shape or basis functions are used to approximate the unknown function within each element. Readers are encouraged to refer the standard books on finite element method [57, 60-62] to understand the method in details.

2.4.1. FEM formulation for a dielectric cylinder [57, 60-62]

Figure 2.2 shows a 2D FEM mesh used for a dielectric cylinder that is discretized with triangular elements. If the mesh contains N nodes (i.e. the vertices of each triangle), the E-field representation can be written as

$$E_z(\vec{r}) = \sum_{n=1}^{N} e_n B_n(\vec{r}) \tag{2.10}$$

Where e_n is the unknown coefficient and represents the E-field value at a node n, B_n is known as the shape or basis function, N is the total number of nodes in the mesh. Substituting equation (2.10) into (2.9), we obtain

$$\sum_{n=1}^{N}\iint_{\Gamma}\left(\frac{1}{\mu_r}\nabla W_m(\vec{r})\bullet\nabla B_n(\vec{r})-k^2W_m(\vec{r})B_n(\vec{r})\right)e_n ds=\oint_{\partial\Gamma}\frac{1}{\mu_r}W_m(\vec{r})\frac{\partial E_z}{\partial n}dl-j\omega\mu_0\iint_{\Gamma}W_m(\vec{r})J_{iz}(\vec{r})ds$$

(2.11)

Setting weighting function W_m as basis function B_m (also known as Galerkin's approach), equation (2.11) can further be written as

$$\sum_{n=1}^{N}\iint_{\Gamma}\left(\frac{1}{\mu_r}\nabla B_m\bullet\nabla B_n-k^2B_mB_n\right)e_n ds=\oint_{\partial\Gamma}\frac{1}{\mu_r}B_m\frac{\partial E_z}{\partial n}dl-j\omega\mu_0\iint_{\Gamma}B_mJ_{iz}ds$$

$$m=1,2,3...N$$
$$n=1,2,3...N$$

(2.12)

In equation (2.12), $\vec{r}$ is omitted from $B_m(\vec{r})$, $B_n(\vec{r})$ and $J_{iz}(\vec{r})$ for simplicity. Equation (2.12) is a complete FEM formulated equation of (2.5).

2.4.2. Incorporation of the Boundary Condition

The Wave equation (2.5) provides solutions for the scattered field that represents both outgoing and incoming waves. In classical electromagnetic analysis, a form of the Sommerfeld radiation boundary condition (RBC) [57]

$$\lim_{\rho\to\infty}\frac{\partial E_z^s}{\partial\rho}=-jkE_z^s \qquad (2.13)$$

is imposed on the boundary at infinity to ensure that the scattered wave is an outward-propagating wave or to suppress the inward-propagating wave. In equation (2.13), ρ is the radius of boundary, k is the wave-number of the medium and E_z^s is the scattered E-field. Since Sommerfeld condition is applied at an infinite distance from the scatterer, this is not very practical for near-field use. In an attempt to approximate Sommerfeld condition to near-field RBC, several approximate RBCs

have been developed. One near-field RBC has been proposed by Bayliss and Turkel [55, 57] and of the form

$$\frac{\partial E_z^s}{\partial \rho} = \alpha(\rho) E_z^s + \beta(\rho) \frac{\partial^2 E_z^s}{\partial \phi^2} \tag{2.14}$$

Where α and β are two coefficients and are given by

$$\alpha(\rho) = \frac{-jk - \frac{3}{2\rho} + \frac{j3}{8kp^2}}{1 - \frac{j}{k\rho}} \tag{2.15}$$

$$\beta(\rho) = \frac{-\frac{j}{2k\rho^2}}{1 - \frac{j}{k\rho}} \tag{2.16}$$

Total E-field E_z in equation (2.5) is the sum of scattered E-field (E_z^s) and incident E-field (E_z^{inc}) and can be written as

$$E_z = E_z^s + E_z^{inc} \tag{2.17}$$

Substituting equations (2.14) - (2.17) into equation (2.12), it can be written in a matrix form

$$[A]\{e\} = \{b\} \tag{2.18}$$

with the individual entries of matrix A and b is given by,

$$a_{mn} = \iint_{\Gamma} \left(\frac{1}{\mu_r} \nabla B_m \bullet \nabla B_n - k^2 B_m B_n\right) ds - \int_{\partial\Gamma} \left(\alpha B_m B_n - \beta \frac{\partial B_m}{\partial \phi} \frac{\partial B_n}{\partial \phi}\right) \rho d\phi$$

$$m = 1,2,3 \ldots N$$
$$n = 1,2,3 \ldots N \tag{2.19}$$

$$b_m = \int_{d\Gamma} B_m \left(\frac{\partial E_z^{inc}}{\partial \rho} - \alpha E_z^{inc} - \beta \frac{\partial^2 E_z^{inc}}{\partial \phi^2}\right) \rho d\phi \quad - j\omega\mu_0 \iint_{\Gamma} B_m J_{iz} ds \tag{2.20}$$

Analytical solutions of integrals in (2.19) are given in appendix A. For a source-free region Γ as shown in figure 2.1 for the scattering analysis of a dielectric cylinder, J_{iz} can be considered as zero and equation (2.20) can be modified accordingly as

$$b_m = \int_{d\Gamma} B_m \left(\frac{\partial E_z^{inc}}{\partial \rho} - \alpha E_z^{inc} - \beta \frac{\partial^2 E_z^{inc}}{\partial \phi^2}\right) \rho d\phi \tag{2.21}$$

As will be shown later, the excitation electric current density J_{iz} is considered in equation (2.21) when we solve for the E-field inside an internal imaging geometry that has an EM excitation source present in the region.

For a plane-wave incidence, $E_z^{inc} = e^{-jk[x\cos\theta + y\sin\theta]} = e^{-jk\rho\cos(\theta-\phi)}$, equation (2.21) can be written as [57],

$$b_m = \int_{\partial\Gamma} - B_m[(\alpha + (1+\beta\rho)jk\cos(\theta-\phi) - \beta k^2\rho^2\sin^2(\theta-\phi)]e^{-jk\rho\cos(\theta-\phi)}\rho d\phi \tag{2.22}$$

In integral (2.22), θ is the angle of plane-wave incidence.

Equation (2.18) along with (2.19) and (2.22) can be solved to find the total E-field inside the dielectric. This will serve the purpose of solving the E-field and hence the power loss density inside an external imaging geometry as stated in steps 1 and 2 of section 1.7.

2.5. Results: Solution of E-field for dielectric cylinders

In this section, the FEM solution of total E-field inside different dielectric cylinders is shown. The dielectric cylinders are illuminated by a normally incident plane-wave. Four different configurations of dielectric cylinders namely 1. A single lossy dielectric cylinder (Fig. 2.3) 2. A

concentric lossy dielectric cylinder (Fig. 2.5) 3. A non-concentric lossy dielectric cylinder (Fig. 2.7) 4. Three lossy dielectrics with one concentric and one non-concentric dielectric (Fig. 2.9) are considered.

2.5.1. Solution of E-field for a single lossy dielectric cylinder

Figure 2.3 shows a lossy dielectric cylinder of radius 38 mm with a relative permittivity ε_r =80, relative permeability μ_r =1 and conductivity $\sigma = 0.2S/m$. A TM^z plane wave E_z^{inc} is incident normally upon a boundary which is located at the distance of 45 mm from the center. The Bayliss-Turkel ABC is applied at this boundary. Figure 2.4 shows the calculated magnitude of total E field at y = 0 mm cut of the cylinder. The FEM solution is compared with the analytical solution at f= 0.5 GHz. The analytical solution [58, 59] for the geometry is given in appendix B.2.

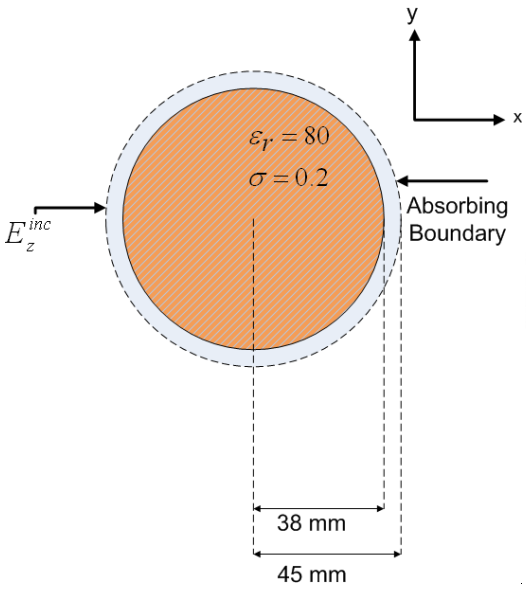

Fig. 2.3

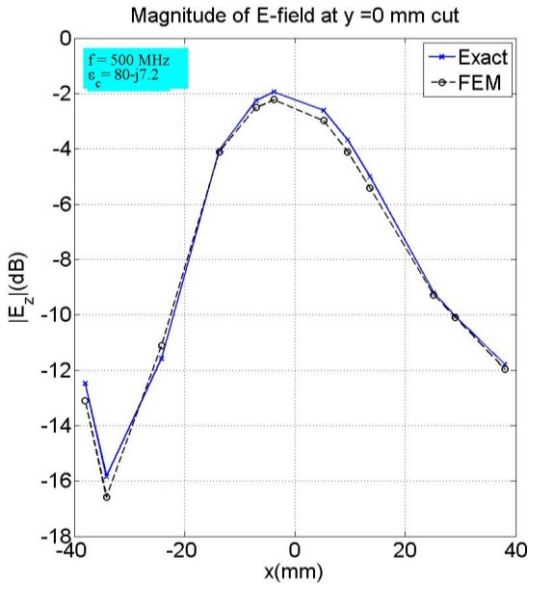

Fig. 2.4

Fig. 2.3 A lossy dielectric cylinder illuminated by a TM^z wave, Fig. 2.4 Magnitude of E-field at y =0 mm cut.

2.5.2. Solution of E-field for a concentric lossy dielectric cylinder

Figure 2.5 shows a concentric lossy dielectric cylinder illuminated by a normally incident

TM^z plane wave. The center dielectric and the surrounding dielectric are considered to have the same real relative permittivity of 80 but a different conductivity of 0.2 S/m and 0.1 S/m respectively. The radius of the center and surrounding dielectric is 5 mm and 38 mm respectively. A TM^z plane wave impinges on an absorbing boundary which is located at 45 mm away from the center. The Bayliss-Turkel ABC is applied at the absorbing boundary. Figure 2.6 shows the FEM and analytical solution of E-field through y = 0 mm cut. The analytical solution [58, 59] of the E-field for this geometry is shown in appendix B.3.

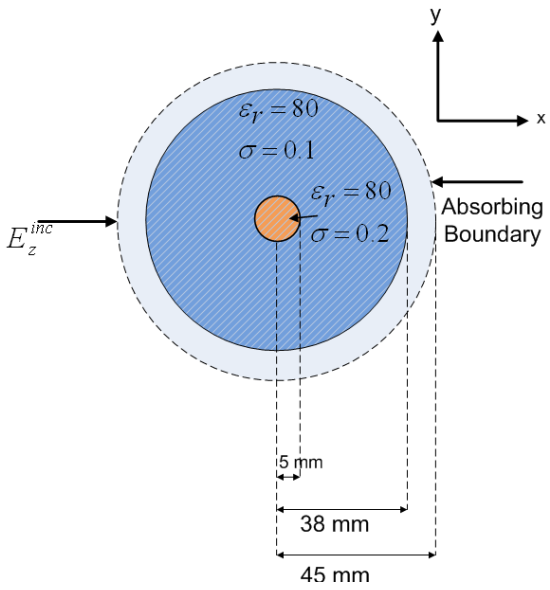

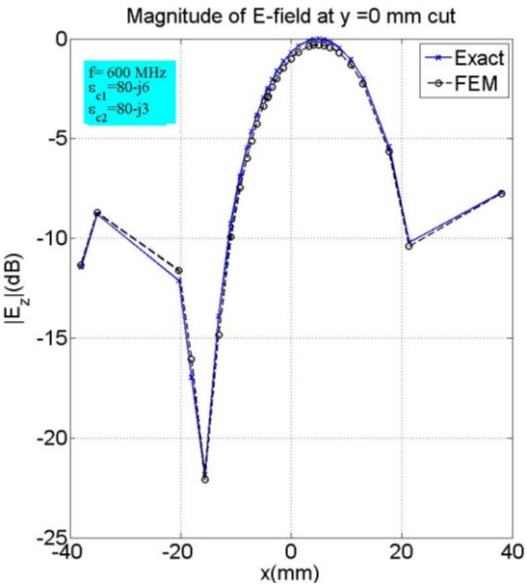

Fig. 2.5 Fig. 2.6

Fig. 2.5 Concentric lossy dielectrics illuminated by a TM^z wave, Fig. 2.6 Magnitude of E-field at y = 0 mm cut.

2.5.3. Solution of E-field for a non-concentric lossy dielectric cylinder

Figure 2.7 shows the structure of such dielectric. The offset inner dielectric is placed at 20 mm away from the center. The offset dielectric and the surrounding dielectric are considered to have the same real relative permittivity but a different conductivity. The radius of the offset and surrounding dielectric is 5 mm and 38 mm respectively. The Bayliss-Turkel ABC is applied at 45 mm away from the center. The real relative permittivity of both the offset and surrounding dielectric

is 80 and the conductivity of the offset and surrounding dielectric is 0.2 S/m and 0.1 S/m respectively. Figure 2.8 shows FEM solution of the E-field at y =0 mm cut of the structure at f =0.6 GHz. Since analytical solution of the E-field for this structure is difficult to achieve, only the FEM solution is shown here.

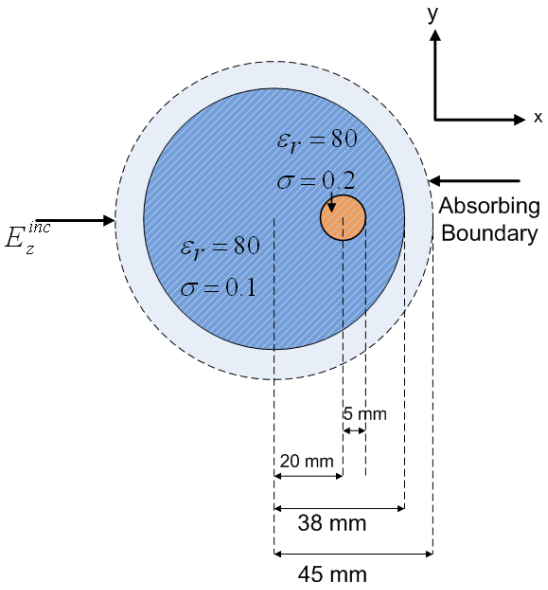

Fig. 2.7

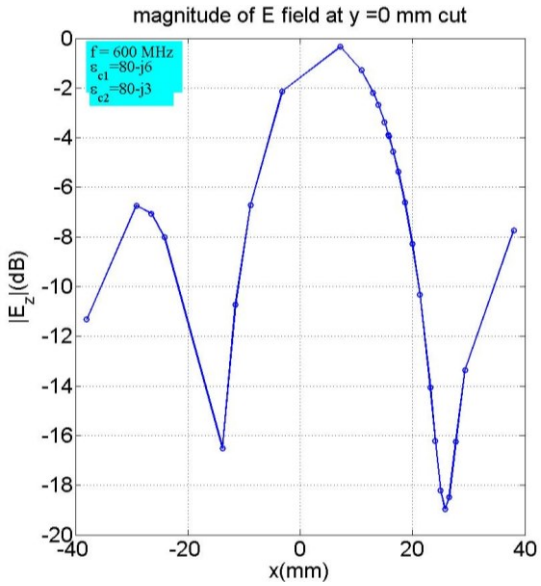

Fig. 2.8

Fig. 2.7 Non-concentric lossy dielectrics illuminated by TM^z wave, Fig. 2.8 Magnitude of E-field at y = 0 mm cut.

2.5.4. Solution of E-field for three lossy dielectrics with one concentric and one non-concentric dielectric

Figure 2.9 shows the structure of this geometry. The offset dielectric is placed at 20 mm away from the center dielectric. The radius of both the center and offset dielectric is 5 mm and the surrounding dielectric is 38 mm respectively. The Bayliss-Turkel ABC is applied at 45 mm away from the center. The real relative permittivity of the center/offset and the surrounding dielectric is considered as 80 and the conductivity of the center/offset and the surrounding dielectric is considered as 0.2 S/m and 0.1 S/m respectively. Figure 2.10 shows the FEM solution of the E-field

at y =0 mm cut of the structure at f =0.6 GHz. Since analytical solution of E-field for this structure is difficult to achieve, only the FEM solution is shown here.

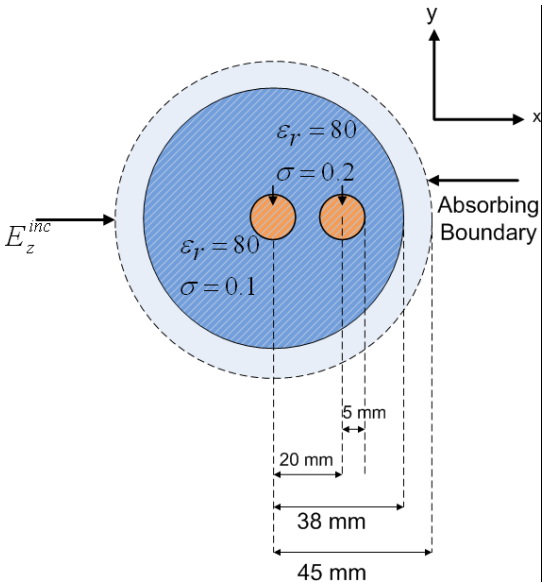

Fig. 2.9

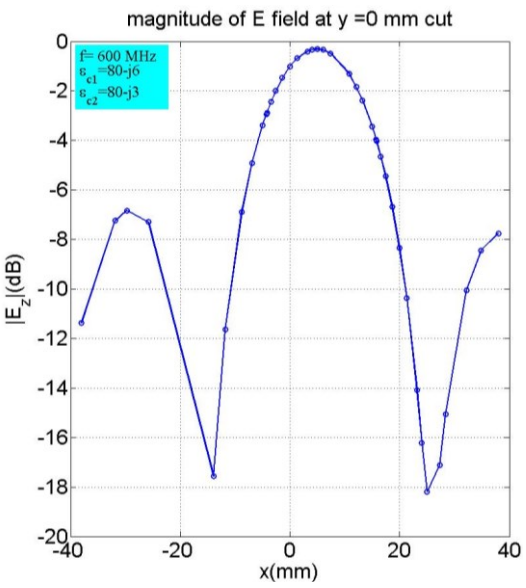

Fig. 2.10

Fig. 2.9 Three lossy dielectrics with one concentric and one non-concentric dielectric illuminated by TM^z wave, Fig. 2.10 Magnitude of E-field at y = 0 mm cut.

2.6. Conclusion

This chapter describes the scattering of electromagnetic wave from an external-imaging geometry which can be considered as a lossy dielectric cylinder. The scalar wave equation is solved using the finite element method (FEM) to find the total E-field inside the geometry. The Bayliss-Turkel absorbing boundary condition (ABC) is adopted along with the FEM modeling. The FEM solution of the E-field for a single lossy dielectric cylinder and a concentric lossy dielectric cylinder is validated with the analytical solution. Achieving the analytical solution of the E-field for a non-concentric dielectric is a challenging task, so only the FEM solution is shown. However, the proximity of the FEM solution to the analytical solution for the first two geometries suggests that the FEM solution is not expected to deviate much from the analytical solution for other two

geometries. The calculation of the E-field is the first step of for reconstructing conductivity distribution inside an external imaging geometry.

CHAPTER III

SOLUTION OF THERMO-ACOUSTIC WAVE EQUATION IN AN EXTERNAL IMAGING GEOMETRY

3.1. Introduction

This chapter describes the solution of the thermo-acoustic wave equation in an external imaging geometry. In thermo-acoustic tomography (TAT), the biological tissues that can be considered as lossy dielectrics are irradiated by short pulses of microwave energy. The absorption of the microwave energy is converted to a transient pressure rise via thermo-elastic expansion that induces an acoustic wave originating from the location of the microwave absorption. The acoustic signal is then detected by various surface acoustic detectors and is used to reconstruct the distribution of the absorbed microwave energy and hence the electrical conductivity within the irradiated tissue. The generation of the acoustic wave via transient pressure rise can be described mathematically by thermo-acoustic wave equation. The solution of this wave equation is the second intermediate step after solving the E-field and the power loss density as described in chapter I. In this chapter, the Finite-element method (FEM) is adopted again along with the Bayliss-Turkel absorbing boundary condition (ABC) to solve the thermo-acoustic equation. The FEM solution of the acoustic pressure is shown at various receiver/detector positions with respect to the time.

3.2. Thermo-acoustic wave equation

The acoustic pressure generated by the absorption of the microwave energy can be determined by the thermo-acoustic wave equation [7],

$$\nabla^2 p(\vec{r},t) - \frac{1}{v_s^2}\frac{\partial^2}{\partial t^2} p(\vec{r},t) = -\frac{\beta_e \sigma}{C_p}\frac{\partial}{\partial t}\left|E(\vec{r},t)\right|^2 \tag{3.1}$$

In equation (3.1), transient electric field $E(\vec{r},t)$ and can be written as

$$E(\vec{r},t) = E_z(\vec{r})\hat{P}(t) \tag{3.2}$$

Where $E_z(\vec{r})$ is the position dependent E-field calculated from chapter II and $\hat{P}(t)$ is the microwave pulse function.

Substituting equation (3.2) into (3.1), it can be written as

$$\nabla^2 p(\vec{r},t) - \frac{1}{v_s^2}\frac{\partial^2}{\partial t^2} p(\vec{r},t) = -\frac{\beta_e}{C_p} s(\vec{r}).2\hat{P}(t).\frac{d\hat{P}(t)}{dt} \tag{3.3}$$

In equation (3.3),

$p(\vec{r},t)$ is the acoustic pressure (Pa) at position $\vec{r}$ and time t.

β_e is the volume expansion coefficient (K^{-1}) (~ 4 x 10^{-4} K^{-1} for muscle) [63].

v_s is the acoustic speed (m/s). (~ 1500 m/s through water) [63].

C_p is the specific heat capacity (J / (Kg K) at constant pressure (~4000 J/(Kg K) for muscle) [63].

$s(\vec{r}) = \sigma\left|E_Z(\vec{r})\right|^2$ = power loss density (W/m^3).

σ = conductivity (S/m).

3.3. FEM formulation of the thermo-acoustic wave equation

This section describes the FEM formulation [7] of the thermo-acoustic wave equation. Using FEM, the acoustic pressure p(r,t) can be represented with N unknown coefficients and basis functions as

$$p(\vec{r},t) = \sum_{j=1}^{N} p_j(t)\psi_j(\vec{r}) \tag{3.4}$$

p_j is the time-dependent unknown coefficient of the acoustic pressure, ψ_j is the position dependent basis function or shape function and N is the total number of nodes used in the FEM mesh.

Following Galerkin's approach as in chapter II and using (3.4), equation (3.2) can be expressed as [7]

$$\sum_{j=1}^{N} p_j \left[\int_s \nabla\psi_i . \nabla\psi_j dS \right] + \sum_{j=1}^{N} \ddot{p}_j \left[\int_s \frac{1}{v_s^2} \psi_i \psi_j dS \right] - \oint_l \psi_i \nabla p . \hat{n} dl = \int_s \frac{\beta_e s}{C_p} . 2\hat{P} \frac{\partial \hat{P}}{\partial t} \psi_i dS$$

$$i = 1,2,...N \qquad (3.5)$$

In equation (3.5), $\vec{r}$ is omitted from $\psi(\vec{r})$, $s(\vec{r})$ and t is omitted from $p(t)$ and $\hat{P}(t)$ for simplicity.

3.4. Incorporation of the boundary condition

As described in chapter II, since Sommerfeld radiation boundary condition is applied at an infinite distance from the scatterer, this is not very practical for near-field use. As for E-field in chapter II, a near-field Bayliss-Turkel [55] absorbing boundary condition (ABC) is applied for the solution of the thermo-acoustic wave equation. The ABC for thermo-acoustic wave equation is of the form

$$\nabla p.\hat{n} = -\frac{1}{v_s}\frac{\partial p}{\partial t} - \frac{p}{2r} \tag{3.6}$$

where r is the radius of the boundary.

Substituting equation (3.6) in (3.5), it can be written in a matrix form

$$[K]\{p\} + [C]\{\dot{p}\} + [M]\{\ddot{p}\} = \{B\} \tag{3.7}$$

with the entries of individual matrices are given by

$$K_{ij} = \int_s \nabla \psi_i . \nabla \psi_j dS + \frac{1}{2r}\oint_l \psi_i \psi_j dl \tag{3.8}$$

$$C_{ij} = \frac{1}{v_s}\oint_l \psi_i \psi_j dl \tag{3.9}$$

$$M_{ij} = \frac{1}{v_s^{\,2}}\int_s \psi_i \psi_j dS \tag{3.10}$$

$$B_i = \frac{\beta_e}{C_p}\int_s \psi_i \left(\sum_k \psi_k s_k\right) dS.2\hat{P}\frac{\partial \hat{P}}{\partial t}$$

$$k = 1,2,3...N \tag{3.11}$$

$$\{p\} = \{p_1, p_2, ...p_N\}^T \tag{3.12}$$

$$\{\dot{p}\} = \left\{\frac{\partial p_1}{\partial t}, \frac{\partial p_2}{\partial t}, ... \frac{\partial p_N}{\partial t}\right\}^T \tag{3.13}$$

$$\{\ddot{p}\} = \left\{\frac{\partial^2 p_1}{\partial t^2}, \frac{\partial^2 p_2}{\partial t^2}, ... \frac{\partial^2 p_N}{\partial t^2}\right\}^T \tag{3.14}$$

Analytical solutions [60-62] of integrals (3.8) to (3.11) are given in appendix A.

3.5. The Newmark's time-stepping algorithm for calculating acoustic pressure in time-domain

Since the FEM formulated equation (3.7) has a time-component, the Newmark's time stepping algorithm [61] is used for discretizing the time-dimension.

Using the Newmark's method, the pressure and its derivatives at any time instant t is related to pressure and its derivatives at subsequent instant $t+\Delta t$ by a recurrence relationship

$$\{p\}_{t+\Delta t} = \{p\}_t + \{\dot{p}\}_t \Delta t + [(\frac{1}{2} - \gamma)\{\ddot{p}\}_t + \gamma\{\ddot{p}\}_{t+\Delta t}]\Delta t^2 \tag{3.15}$$

$$\{\dot{p}\}_{t+\Delta t} = \{\dot{p}\}_t + [(1-\delta)\{\ddot{p}\}_t + \delta\{\ddot{p}\}_{t+\Delta t}]\Delta t \tag{3.16}$$

$$\{\ddot{p}\}_{t+\Delta t} = \frac{1}{\gamma\Delta t^2}(\{p\}_{t+\Delta t} - \{p\}_t) - \frac{1}{\gamma\Delta t}\{\dot{p}\}_t - \left(\frac{1}{2\gamma} - 1\right)\{\ddot{p}\}_t \tag{3.17}$$

Where

Δt =time step

γ, δ =parameters for determining the accuracy and stability of the Newmark's algorithm.

$\{p\}_t, \{\dot{p}\}_t, \{\ddot{p}\}_t$ are the values of the pressure and its derivatives at time t and $\{p\}_{t+\Delta t}, \{\dot{p}\}_{t+\Delta t}, \{\ddot{p}\}_{t+\Delta t}$ are the values of the pressure and its derivatives at the subsequent instant $t+\Delta t$.

Assuming $K, C, M, \gamma, \delta, \Delta t$ is constant, substituting equations (3.15) - (3.17) into (3.7), we obtain

$$\left([K]+\frac{1}{\gamma\Delta t^2}[M]+\frac{\delta}{\gamma\Delta t}[C]\right)\{p\}_{t+\Delta t}=\{B\}_{t+\Delta t}+[M]\times\left[\frac{1}{\gamma\Delta t^2}\{p\}_t+\frac{1}{\gamma\Delta t}\{\dot{p}\}_t+\left(\frac{1}{2\gamma}-1\right)\{\ddot{p}\}_t\right]$$

$$+[C]\times\left[\frac{\delta}{\gamma\Delta t}\{p\}_t+(\frac{\delta}{\gamma}-1)\{\dot{p}\}_t+\left(\frac{\delta}{2\gamma}-1\right)\Delta t\{\ddot{p}\}_t\right] \quad (3.18)$$

The time-stepping parameters were taken as $\delta=0.5,\ \gamma=0.25$ [61]. Equations (3.18) along with (3.15) - (3.17) can be solved to find the acoustic pressure at each time instant.

3.6. Results

3.6.1. Solution of the acoustic pressure in time-domain with NO object present in the medium

In this section, the solution of the acoustic pressure at various receiver locations is shown with no object present in the medium. Figure 3.1 shows the structure of the geometry. The radius of the geometry is considered as 38 mm. The conductivity and relative permittivity of the entire medium is considered as 0.1 S/m and 80 respectively. The geometry is illuminated with a Gaussian pulse of full-width half-maximum (FWHM) of 2 μs and with a peak occurs at 25 μs as shown in figure 3.2. A TM^z plane wave E_z^{inc} is impinging normally upon the external boundary of the geometry at p = 38 mm and θ= 0°. The acoustic pressure wave which is generated inside the geometry as a result of EM illumination is detected by four receivers Rx A, Rx B, Rx C and Rx D located at 3'o clock (x= 38 mm, y=0 mm), 12'o clock (x =0 mm, y=38 mm), 9'o clock (x= -38 mm, y= 0 mm) and 6'o clock (x =0 mm, y= -38 mm) position respectively. Figure 3.3 shows the normalized captured pressure at four different receivers. The captured pressure at all receivers is normalized with respect to the maximum captured pressure.

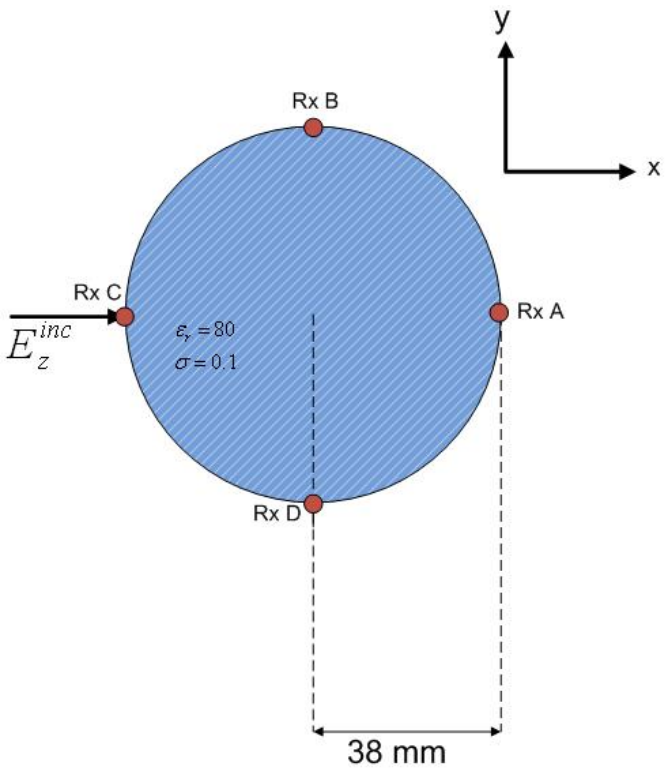

Fig 3.1 External imaging geometry with no object present in the medium

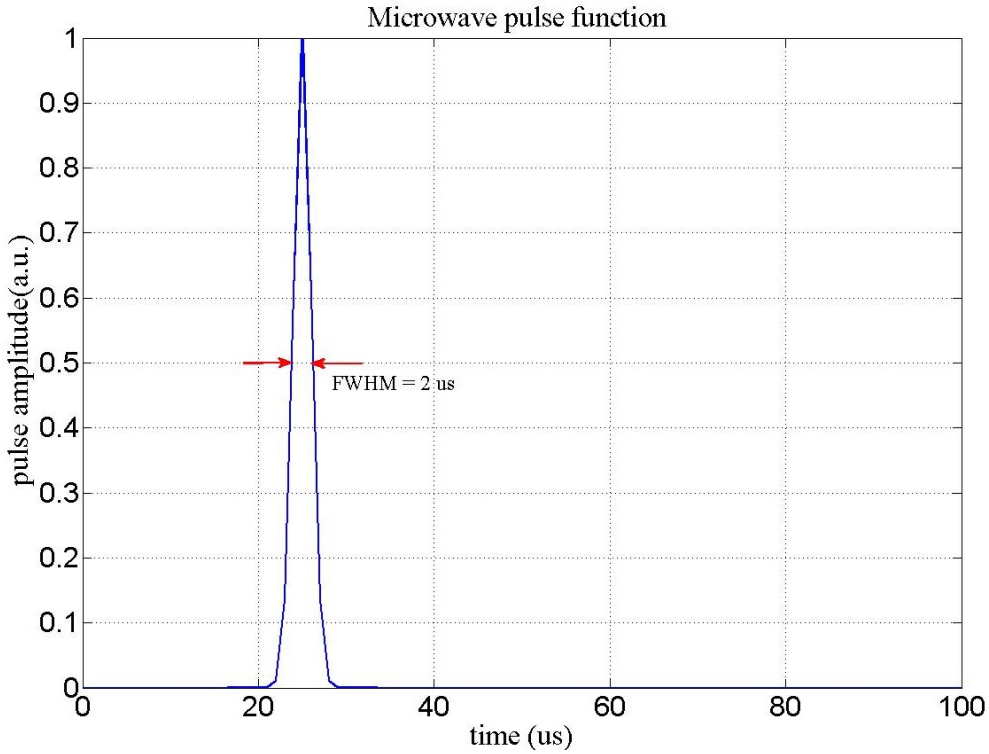

Fig 3.2 Pulse function

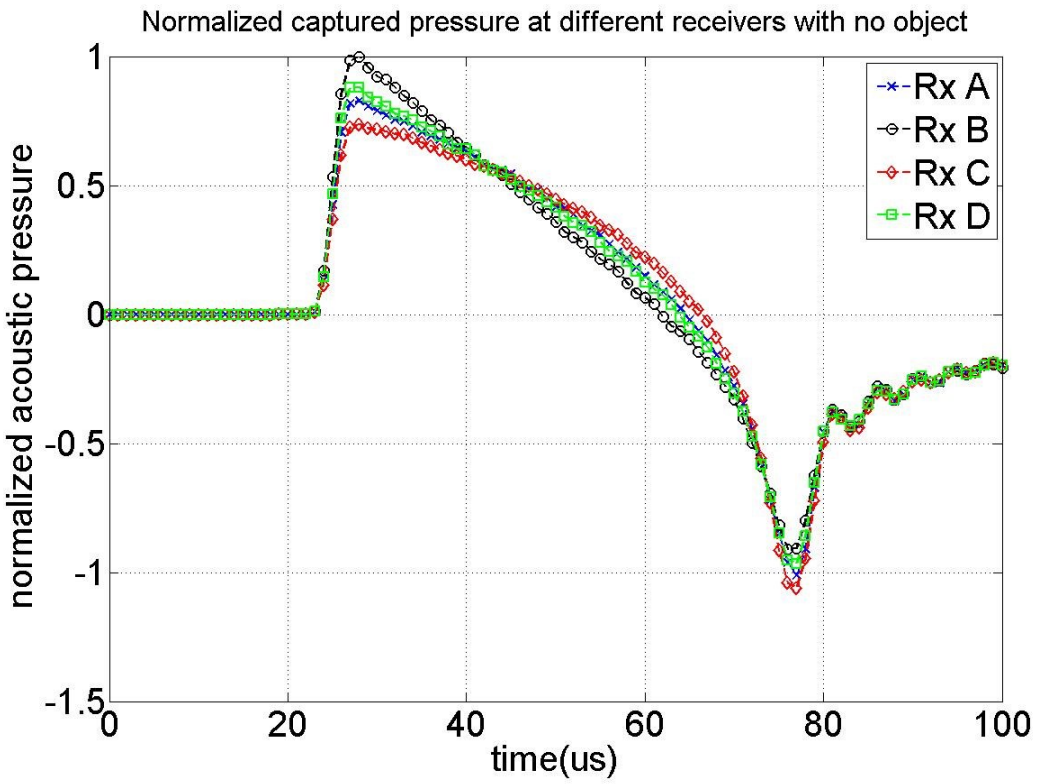

Fig 3.3 Captured acoustic pressure at four different receivers with no object present in the medium

For calculating the acoustic pressure as shown in figure 3.3, ehe E-field and hence the power loss density $s(\vec{r})$ which appears on the right hand side of equation (3.3) is calculated for a frequency of 1GHz using the procedure described in chapter II.

3.6.2. Solution of the acoustic pressure in time-domain with an object located at the center

In this section, the solution of the acoustic pressure at various receiver locations with an object located at the center is shown and discussed. Figure 3.4 shows the structure of an external imaging geometry of radius 38 mm. An object of radius 5 mm which can be considered as a tumor mimicking object is located at the center. The object is enclosed by the background which can be

considered as surrounding normal tissues. The Conductivity of the object and background is considered as 0.3 S/m and 0.1 S/m respectively [7]. The relative permittivity of both the object and background is considered as 80.

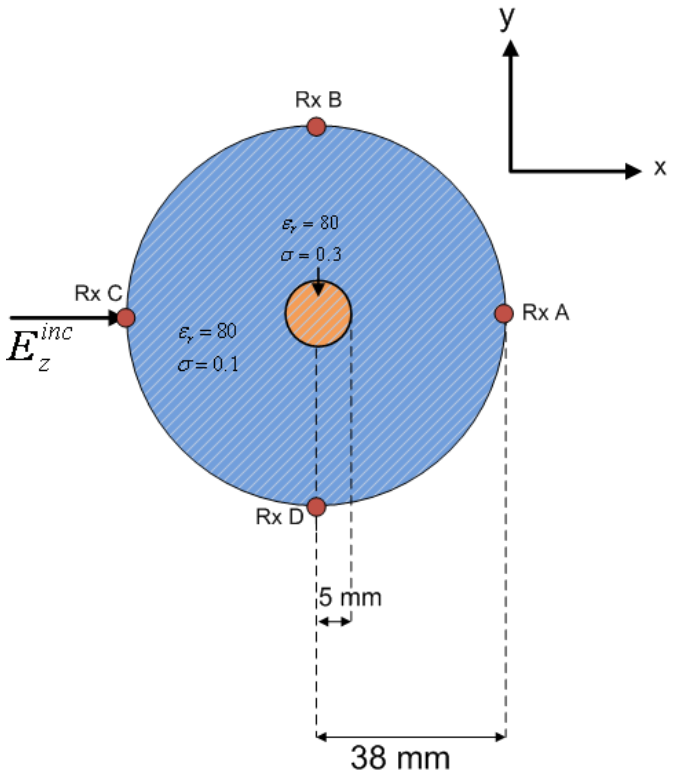

Fig 3.4 External imaging geometry with a central object

The geometry is illuminated with a Gaussian pulse of full-width half-maximum (FWHM) of 2 μs and with a peak occurs at 25 μs as shown in figure 3.2. A TM^z plane wave E_z^{inc} is impinging normally upon the external boundary of the geometry at p = 38 mm and θ= 0°. The acoustic pressure wave which is generated inside the geometry as a result of EM illumination is detected by four receivers Rx A, Rx B, Rx C and Rx D located at 3'o clock (x= 38 mm, y=0 mm), 12'o clock (x =0 mm, y=38 mm), 9'o clock (x= -38 mm, y= 0 mm) and 6'o clock (x =0 mm, y= -38 mm) position respectively.

Figure 3.5 shows the calculated acoustic pressure at four receiver locations. The E-field and hence the power loss density $s(\vec{r})$ which appears on the right hand side of equation (3.3) is calculated for a frequency of 1GHz using the procedure described in chapter II. Table 1 summarizes the calculated and actual propagation time of the acoustic wave to reach different receivers.

Table 1: Calculated and actual propagation time for the acoustic wave to reach different receiverswith a central object

Receivers	Calculated propagation time (μs) from the center of the object to Rx	Actual propagation time (μs) from the object to Rx
Rx A	25.3	49-25=24
Rx B	25.3	49-25=24
Rx C	25.3	49-25=24
Rx D	25.3	49-25=24

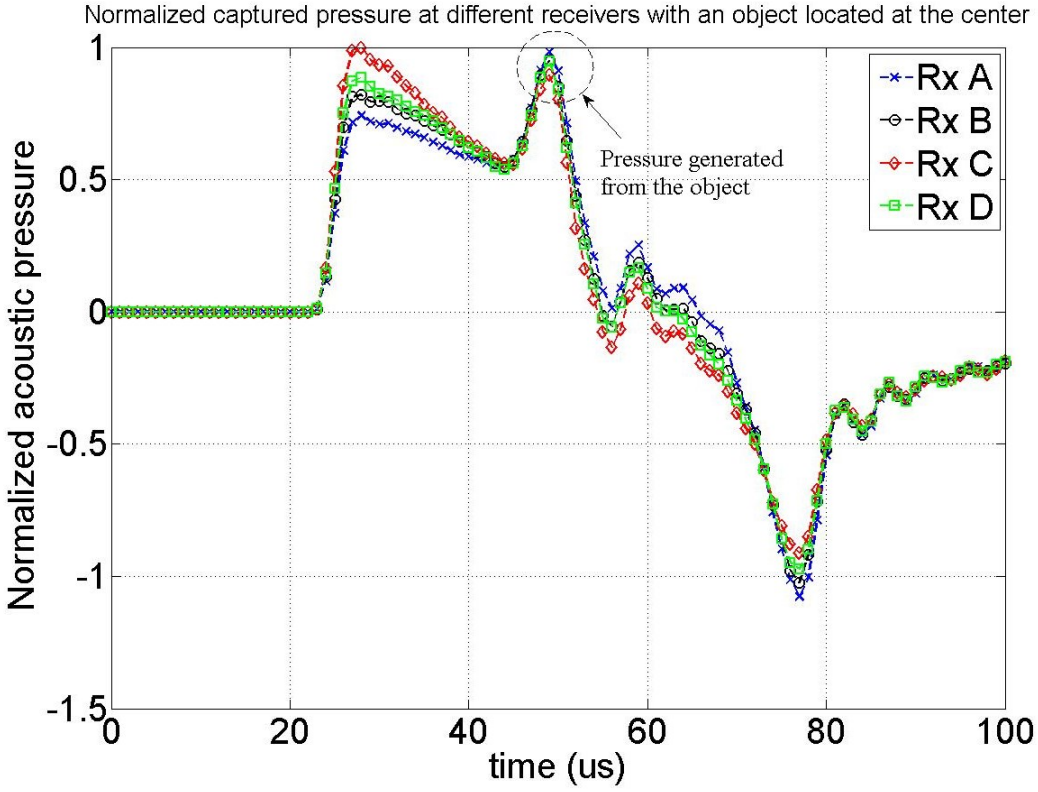

Fig 3.5 Captured acoustic pressure at four different receivers

3.6.3. Solution of the acoustic pressure in time-domain with an object away from the center

Figure 3.6 shows an external imaging geometry with an object of 5 mm radius located 20 mm away from the center. The Radius of the geometry is considered as 38 mm. The Conductivity of the object and background is considered as 0.3 S/m and 0.1 S/m respectively [7]. The relative permittivity of both the object and background is considered as 80. The Figure 3.7 shows the calculated acoustic pressure at Rx A, B, C and D positions. The geometry is illuminated with a Gaussian pulse of full-width half-maximum (FWHM) of 2 μs and with a peak occurs at 25 μs as shown in figure 3.2. A TM^z plane wave E_z^{inc} is impinging normally upon the external boundary of the geometry. The pressure at four receivers is calculated at 1 GHz.

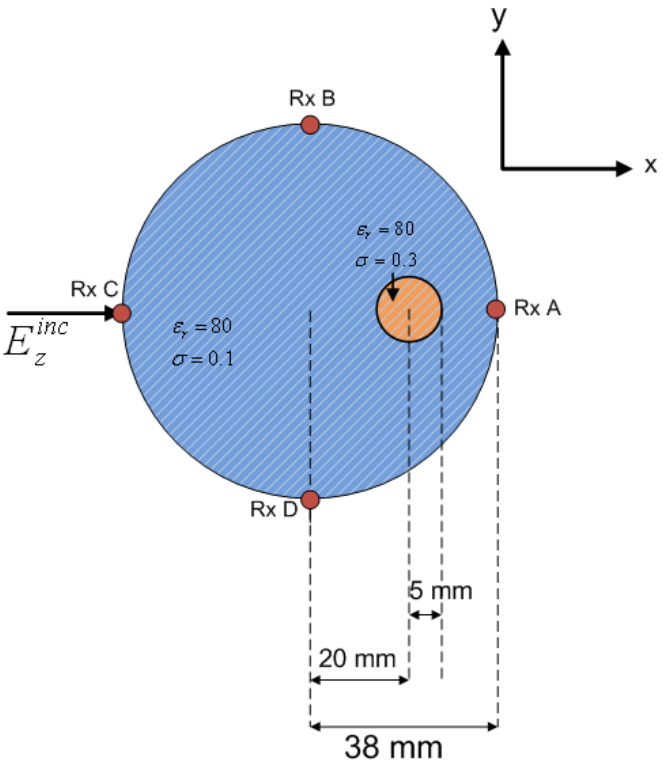

Fig 3.6 External imaging geometry with a shifted object

Table 2: Calculated and actual propagation time for the acoustic wave to reach different receivers with a shifted object

Receivers	Calculated propagation time (μs) from the center of the object to Rx	Actual propagation time (μs) from the object to Rx
Rx A	12	35-25=10
Rx B	28.6	52-25=27
Rx C	38.7	62-25=37
Rx D	28.6	52-25=27

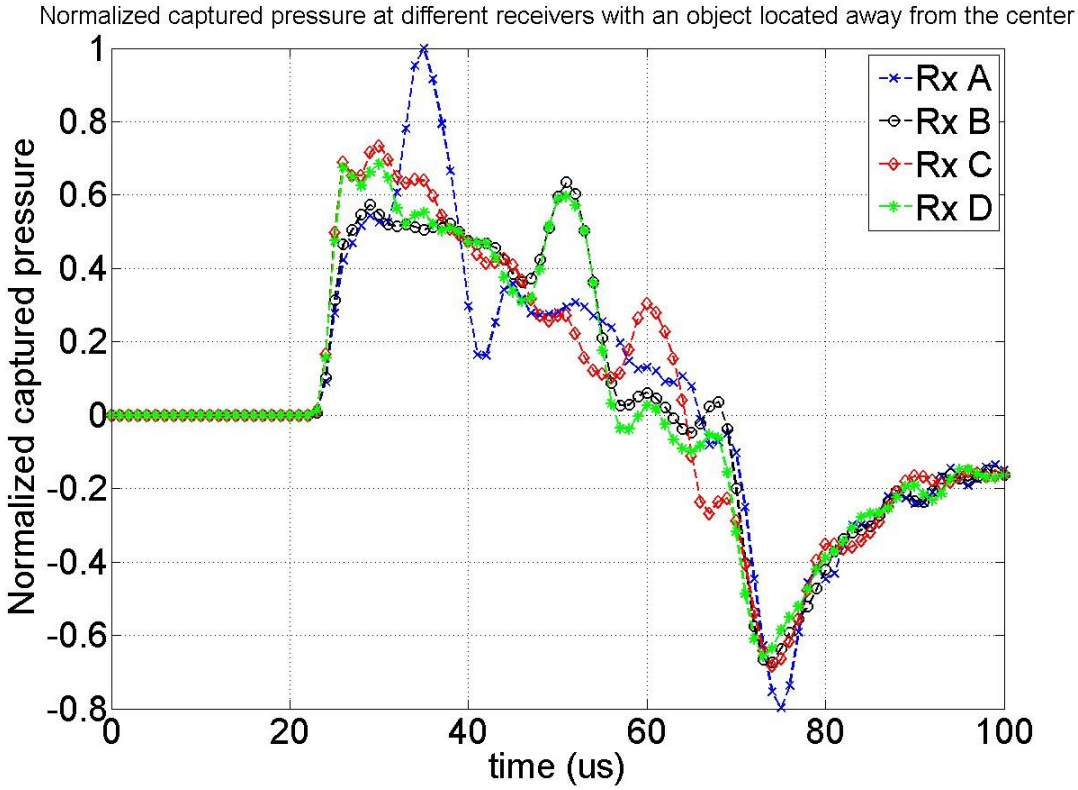

Fig 3.7 Acoustic pressure at four different Rx locations for an external geometry with a shifted object

Table 2 summarizes the calculated and actual propagation time of acoustic wave to reach different receivers.

3.7. Discussion

In this chapter, the acoustic pressure which is generated due to electromagnetic illumination inside an external geometry is computed. The computed pressure that is captured at different

receivers is plotted with respect to time. The pressure is computed for three different external geometries, namely, 1. An external imaging geometry with no object (Fig. 3.1) 2. An external imaging geometry with an object at the center (Fig. 3.4). 3. An external geometry with an object away from the center (Fig. 3.6).

Figure 3.3 shows the captured pressure with no object present in the medium. Because of the absence of the object, the calculated pressure that is shown in figure 3.3 is entirely generated from the background that has a finite relative permittivity and conductivity.

Figure 3.5 shows the computed pressure at four different receivers for an external imaging geometry that has an object at the center. The pressure generated from the object is represented by a single peak that has occurred at 49 μs as shown in figure 3.5. Table 1 summarizes the calculated and actual propagation time of the acoustic wave to reach different receivers from the object. The calculated propagation time t_c is determined by $t_c = d/ v_{s.,}$ where d is the distance from the center of the object to the receiver and $v_{s.}$ = acoustic speed (~1500 m/s is considered in this study). For example, t_c for receiver A is $t_c = 38\text{mm}/1500\text{e}3 \sim 25.3$ μs. The actual propagation time is considered after 25 μs when the peak of the illuminating pulse occurs. It is worth mentioning that we have used point receivers in this study for feasibility. So, the dimension of the receiver is negligible.

For the geometry of figure 3.4, Since all the four receivers are located at equal distance (38 mm) from the object (origin of the acoustic pressure), the actual propagation time of the acoustic wave to reach the receivers from the object is the same (24 μs) as shown in table 1. The difference between the actual and calculated propagation time is due to the fact that the calculated propagation time assumes the acoustic wave to propagate from the center of the object, but it actually may propagate from the center or certain point away from the center (e.g. edge) of the object.

Figure 3.7 shows the computed pressure at four different receivers for an external imaging geometry that has an object located at 20 mm away from the center of the geometry. The pressure

generated from the object and captured at four different receivers Rx A, B, C and D as shown in figure 3.6. The pressure that is generated from the object and captured at four receivers is represented by multiple peaks that occurred at different time instants as shown in figure 3.7. Table 2 shows the calculated and actual propagation time of the acoustic wave to reach the receivers from the object. The calculated propagation time t_c is determined by $t_c = d / v_{s.}$, where d is the distance from the center of the object to the receiver and $v_{s.}$ = acoustic speed (~1500 m/s is considered in this study).

Since Rx A is the closest (18 mm from the center of the object) to the object, the acoustic wave reaches faster (10 μs actual time) to Rx A from the object than other receivers. Rx B and D is at the same "hypotenuse" distance (~ 43 mm) from the center of the object, so the actual propagation time is the same (27μs actual time). Rx C is located furthest (58 mm) from the center of the object, so the acoustic wave takes the longest time (37 μs actual time) to reach this receiver.

The difference between the actual and calculated propagation time is due to the fact that the calculated propagation time assumes the acoustic wave to propagate from the center of the object, but it actually may propagate from the center or certain point away from center (e.g. edge) of the object.

3.8. Conclusion

This chapter shows the calculation of the pressure/acoustic wave using the finite element method (FEM) along with the Newmark's time-stepping algorithm and absorbing boundary condition. The calculated acoustic pressure is shown at four various receiver locations. The propagation time of the pressure wave from the object to various receivers depends on the distance of the receivers from the object. Since the object is considered to be the location from where the pressure/acoustic wave is generated, the propagation time of the pressure wave to reach the receivers that are close to the

object should be faster than to those located far from the object. The calculation of the thermo-acoustic wave equation is the second step to TAT image reconstruction algorithm.

CHAPTER IV

RECONSTRUCTION OF CONDUCTIVITY IN AN EXTERNAL IMAGING GEOMETRY

4.1. Introduction

This chapter describes the final step for reconstructing conductivity in an external imaging geometry. This step involves finding a "Sensitivity" or "Jacobian" matrix which represents the change of pressure with respect to the change of power loss density. The calculated Jacobian is an "ill-posed" matrix and poses singularities while performing the inversion. To overcome this difficulty, the Levenberg-Marquardt algorithm is applied for regularizing Jacobian matrix. Once the Jacobian is found, the power loss density and hence conductivity can be reconstructed.

4.2. The calculation of "Jacobian" or "Sensitivity" matrix

The "Jacobian" or "Sensitivity" matrix represents the change in acoustic pressure with respect to the change in power loss density and is represented by $\frac{\partial p}{\partial s}$ where ∂p is the change in pressure and ∂s is the change in power loss density.

Differentiating both sides of equations (3.15) - (3.18) with respect to s, we obtain

$$\left([K]+\frac{1}{\gamma\Delta t^2}[M]+\frac{\delta}{\gamma\Delta t}[C]\right)\left[\frac{\partial p}{\partial s}\right]_{t+\Delta t}=[\frac{\partial B}{\partial s}]_{t+\Delta t}+[M]$$

$$\times\left[\frac{1}{\gamma\Delta t^2}\left[\frac{\partial p}{\partial s}\right]_t+\frac{1}{\gamma\Delta t}(\frac{\partial}{\partial s}\left\{\frac{\partial p}{\partial t}\right\}_t)\ +\left(\frac{1}{2\gamma}-1\right)(\frac{\partial}{\partial s}\left\{\frac{\partial^2 p}{\partial t^2}\right\}_t)\right]+[C]$$

$$\times\left[\frac{\delta}{\gamma\Delta t}\left[\frac{\partial p}{\partial s}\right]_t+(\frac{\delta}{\gamma}-1)(\frac{\partial}{\partial s}\left\{\frac{\partial p}{\partial t}\right\}_t)\ +\left(\frac{\delta}{2\gamma}-1\right)\Delta t(\frac{\partial}{\partial s}\left\{\frac{\partial^2 p}{\partial t^2}\right\}_t)\right] \tag{4.1}$$

$$\left\{\frac{\partial p}{\partial s}\right\}_{t+\Delta t}=\left\{\frac{\partial p}{\partial s}\right\}_t+(\frac{\partial}{\partial s}\left\{\frac{\partial p}{\partial t}\right\}_t)\Delta t+[(\frac{1}{2}-\gamma)(\frac{\partial}{\partial s}\left\{\frac{\partial^2 p}{\partial t^2}\right\}_t)+\gamma(\frac{\partial}{\partial s}\left\{\frac{\partial^2 p}{\partial t^2}\right\}_{t+\Delta t})]\Delta t^2 \tag{4.2}$$

$$(\frac{\partial}{\partial s}\left\{\frac{\partial p}{\partial t}\right\}_{t+\Delta t})\ =(\frac{\partial}{\partial s}\left\{\frac{\partial p}{\partial t}\right\}_t)+\Delta t(1-\delta)(\frac{\partial}{\partial s}\left\{\frac{\partial^2 p}{\partial t^2}\right\}_t)\ +\delta\Delta t(\frac{\partial}{\partial s}\left\{\frac{\partial^2 p}{\partial t^2}\right\}_{t+\Delta t}) \tag{4.3}$$

$$(\frac{\partial}{\partial s}\left\{\frac{\partial^2 p}{\partial t^2}\right\}_{t+\Delta t})=\frac{1}{\gamma\Delta t^2}(\left[\frac{\partial p}{\partial s}\right]_{t+\Delta t}-\left[\frac{\partial p}{\partial s}\right]_t)-\frac{1}{\gamma\Delta t}(\frac{\partial}{\partial s}\left\{\frac{\partial p}{\partial t}\right\}_t)\ -\left(\frac{1}{2\gamma}-1\right)(\frac{\partial}{\partial s}\left\{\frac{\partial^2 p}{\partial t^2}\right\}_t)$$

(4.4)

Where

$$\frac{\partial B_i}{\partial s_k}=\frac{\beta_e}{C_p}\int_s\psi_i\psi_k dS.2\hat{P}\frac{d\hat{P}}{dt} \qquad \begin{matrix} i=1,2,3...N \\ k=1,2,3...N \end{matrix} \tag{4.5}$$

Equations (4.1) along with (4.2)-(4.5) can be solved to calculate $\frac{\partial p}{\partial s}$ at each time instant.

4.3. Structure of a Jacobian Matrix

Jacobian matrix J, represented by $\frac{\partial p}{\partial s}$ is an N x M matrix where N is the number of FEM nodes and M is the total number of acoustic receivers. Structure of a Jacobian matrix is of the form

$$J = \begin{bmatrix} \frac{\partial p_1}{\partial s_1} & \frac{\partial p_2}{\partial s_1} & \frac{\partial p_3}{\partial s_1} \cdots & \frac{\partial p_M}{\partial s_1} \\ \frac{\partial p_1}{\partial s_2} & \frac{\partial p_2}{\partial s_2} & \frac{\partial p_3}{\partial s_2} \cdots & \frac{\partial p_M}{\partial s_2} \\ \vdots & \vdots & \vdots & \vdots \\ \frac{\partial p_1}{\partial s_N} & \frac{\partial p_2}{\partial s_N} & \frac{\partial p_3}{\partial s_N} & \frac{\partial p_M}{\partial s_N} \end{bmatrix} \tag{4.6}$$

4.4. The Levenberg-Marquardt (LM) method [64, 65]

Jacobian matrix J shown above is an "ill-posed" matrix and poses singularities while performing inversion. To overcome this difficulty, a regularization parameter λ is added to the diagonal elements of the Hessian matrix which is defined by the product of the Jacobian matrix and its transpose. This process is the Levenberg-Marquardt regularization method and using this method we can write,

$$(J_t^T J_t + \lambda I)\Delta s = J_t^T (p_t^m - p_t^c) \tag{4.7}$$

Where,

J_t = Assembly of J for all time-steps

J_t^T = Transpose of J_t

$J_t^T J_t$ = Hessian matrix

λ =Regularization parameter

I =Identity matrix

p_t^m = Assembly of true acoustic pressure for all time steps. This pressure is found only once by solving the acoustic wave equation using the set conductivity profile.

p_t^c = Assembly of calculated acoustic pressure for all time steps. This pressure is found in every iteration by solving the acoustic wave equation using the updated conductivity profile.

Δs =update vector and is represented by $\Delta s = \Delta s_1, \Delta s_2, \bullet\bullet\bullet \quad \Delta s_N$

Equation (4.7) can be used to find update vector Δs . After finding Δs , calculated power loss density is updated as

$$s^{update} = s^c + \Delta s \tag{4.8}$$

From the updated power loss density, conductivity can be calculated as

$$\sigma^{update} = \frac{s^{update}}{\left|E_z^c\right|^2} \tag{4.9}$$

where E_z^c is the electric field calculated with the updated conductivity profile.

4.5. Results and discussions

In this section, various images of reconstructed conductivity profile in an external imaging geometry are shown. An external imaging geometry with single and multiple objects/targets and with a 3:1 contrast ratio of conductivity [7] between the object and background is considered. Figure 4.1 and 4.4 shows an external imaging geometry with single and multiple objects respectively. The reconstructed images shown are for a frequency of 1 GHz and total 88 acoustic receivers are evenly placed across the external boundary of the geometry. The regularization parameter λ used was 0.8 [7].

4.5.1. Reconstruction of Conductivity with a single target

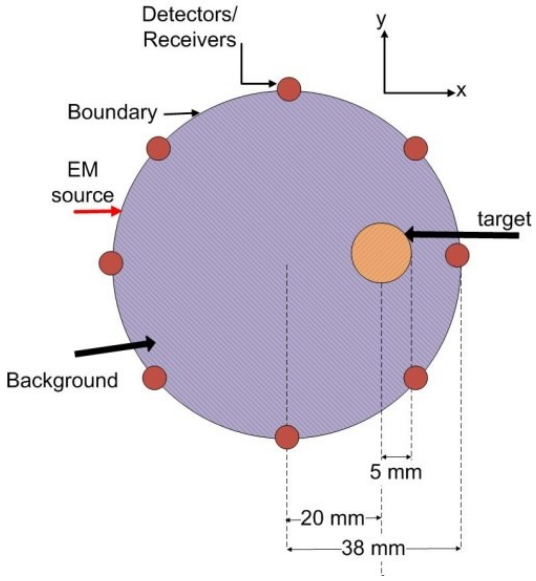

Figure 4.1 External imaging geometry with a single target

Figure 4.1 shows the structure of an external imaging geometry with a single target. A target of 5 mm radius is located at 20 mm away from the center of the geometry. A TM^z plane wave impinges on the boundary of the geometry. Various acoustic receivers are placed around the boundary of the geometry to capture the acoustic wave generated within the geometry as a result of EM illumination. From the captured acoustic pressure and following the steps 1-3 in chapter I, the conductivity distribution inside the geometry is reconstructed.

Figure 4.2.A shows the image of true conductivity profile that needs to be reconstructed. True conductivity profile serves the purpose of mimicking real cancerous cells and helps in computing the true E-field E_z^m and hence computing the true or "measured" acoustic pressure p_t^m. A 3:1 ratio [7] of conductivity between target and background is considered. The radius of the target and background is considered as 5 mm and 38 mm respectively. The center to center distance of the target and background is 20 mm. Table 3 shows the dimensions and dielectric properties used for the geometry. The relative permittivity of both the background and target is considered as 80. The

conductivity of the target and background is considered as 0.3 S/m and 0.1 S/m respectively. The frequency of operation is 1 GHz. Figure 4.2.B. shows the image of the reconstructed conductivity profile and figure 4.2.C shows the line plot of true and reconstructed conductivity profile through y = 2mm cut. Maximum reconstructed conductivity for the target and background is 0.3492 S/m and 0.1039 S/m respectively. Table 4 lists the reconstructed conductivities for both the target and background along with the percentage errors. The regularization parameter used for the simulation is 0.8. As can be seen from the reconstructed image, TAT can accurately locate the shape and position of the target or "tumor-mimicking" object in an external imaging geometry.

Table 3: Dimensions and electrical properties used for external imaging geometry with single target and with a 3:1 contrast ratio

Medium	Radius (mm)	Relative Permeability	Relative Permittivity	Conductivity σ (S/m)
Background	38	1	80	0.1
Target/Object	5	1	80	0.3

Table 4: Original and reconstructed conductivity for external imaging geometry with a single target and with a 3:1 contrast ratio

Medium	σ_{orig} (S/m)	σ_{recons} (S/m)	% error
Background	0.1	0.1039	3.9
Target/Object	0.3	0.3492	16.40

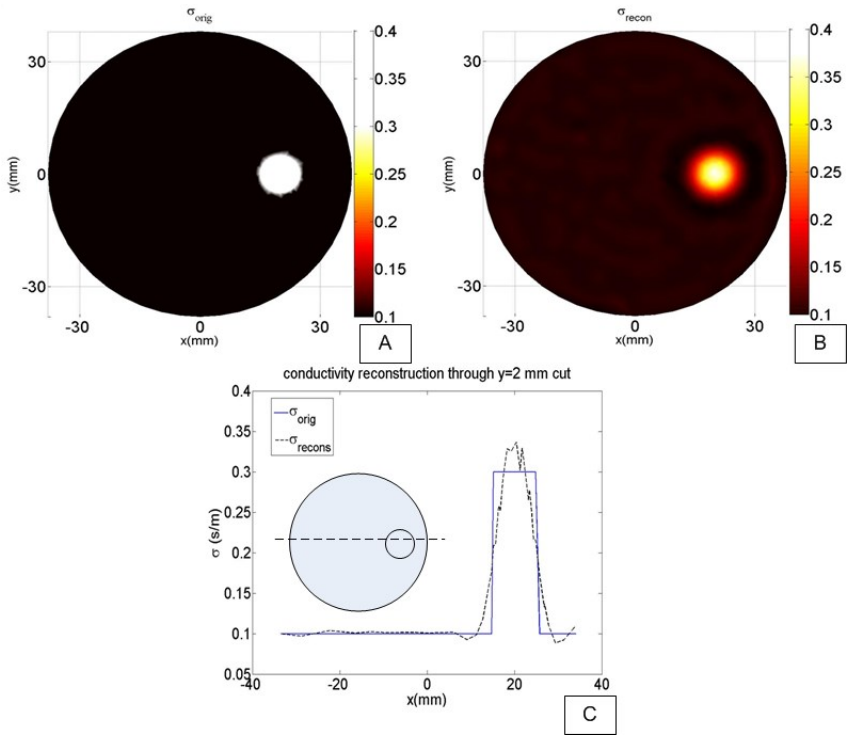

Figure 4.2.A: Image of original conductivity with a 3:1 contrast, Figure 4.2.B: Image of reconstructed conductivity, Figure 4.2.C: Line plot of original and reconstructed conductivity through y =2 mm cut.

4.5.2. Reconstruction of Conductivity with TWO targets

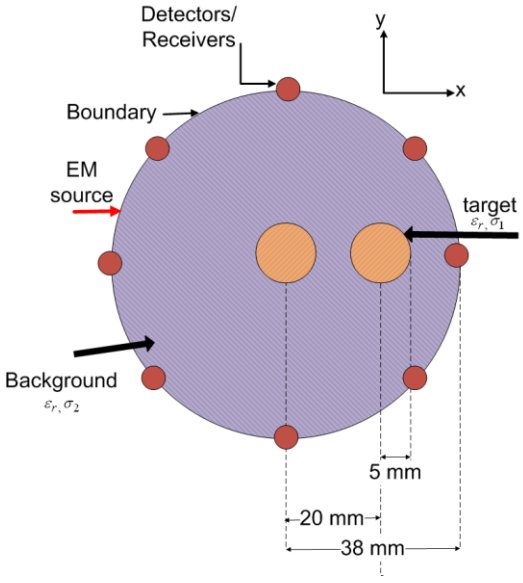

Figure 4.3 External imaging geometry with two targets

Figure 4.3 shows the structure of an external imaging geometry with two targets. The center to center distance of two targets is 20 mm and the radius of each target is 5 mm. The radius of the background is considered as 38 mm. A TM^z plane wave impinges on the boundary of the geometry. Various acoustic receivers are placed around the boundary of the geometry to capture acoustic wave generated within the geometry as a result of EM illumination. From the captured acoustic pressure and following the steps 1-3 in chapter I, the power loss density and hence the conductivity distribution inside the geometry is reconstructed.

Figure 4.4.A shows the image of true conductivity profile with two targets and with a 3:1 ratio of conductivity between the target and background. The dimensions and electrical properties used for the geometry are the same as for the geometry with single target. The relative permittivity of the background and both the targets is considered as 80. The conductivity of the target and background is considered as 0.3 S/m and 0.1 S/m respectively. Figure 4.4.B. shows the image of the reconstructed conductivity profile and figure 4.4.C shows the line plot of true and reconstructed conductivity profile through y = 2mm cut. The regularization parameter used was 0.8. As can be seen from the reconstructed image, TAT can accurately locate the position and the shape of multiple targets in an external imaging geometry. Maximum reconstructed conductivity for targets located at the center and 20 mm away from center is 0.3492 S/m and 0.3489 S/m respectively. Table 5 shows the maximum reconstructed conductivity for background and targets along with the percentage errors.

Table 5: Original and reconstructed conductivity for external imaging geometry with two targets and with a 3:1 contrast ratio

Medium	σ_{orig} (S/m)	σ_{recons} (S/m)	% error
Background	0.1	0.1120	12
Target 1	0.3	0.3492	16.40
Target 2	0.3	0.3489	16.30

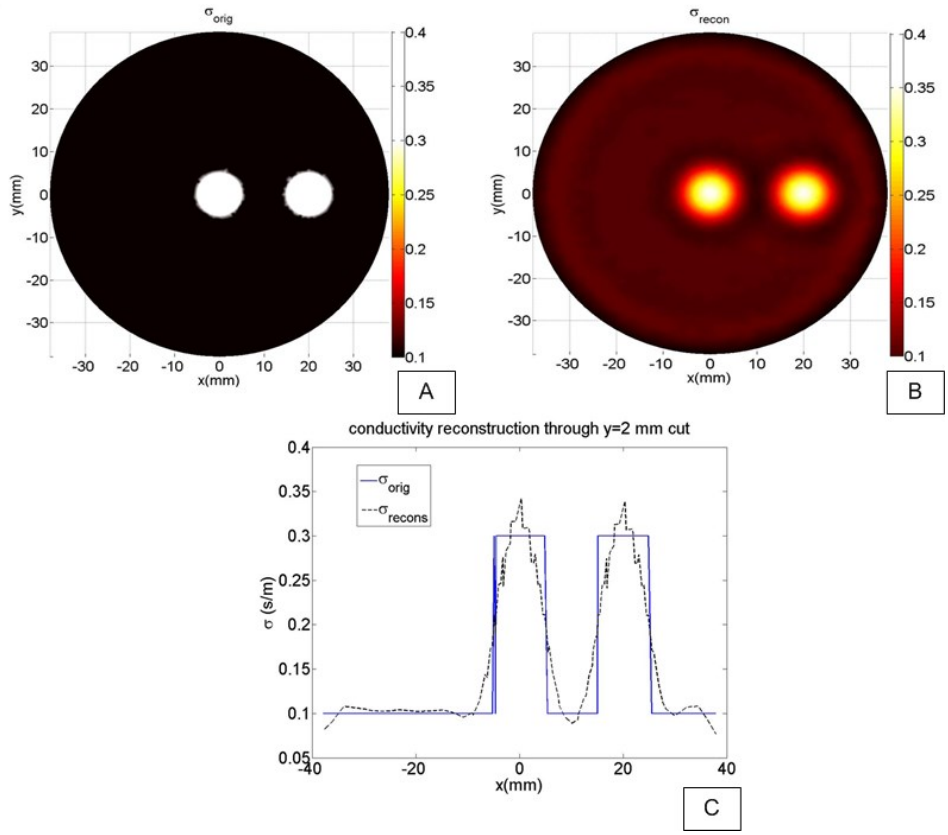

Figure 4.4.A: Image of original conductivity with a 3:1 contrast, Figure 4.4.B: Image of reconstructed conductivity, Figure 4.4.C: Line plot of original and reconstructed conductivity through y =2 mm cut.

4.6. Conclusion

An external-imaging geometry with single and double targets and with 3:1 ratio of conductivity between target and background was considered. Various images of reconstructed conductivity profile were shown. The image of true conductivity profile can be considered as "actual" location of cancerous cell and the image of reconstructed conductivity profile serves the purpose of locating that cancerous cell both qualitative and quantitatively. Reconstructing conductivity information

using thermo-acoustic tomography is an iterative process and it continues until a threshold error is achieved. In this study, the number of iteration for the reconstruction routine pertaining to external imaging geometry was 50 and each iteration took ~ 40 seconds. The simulation was run in MATLAB™ with a 3GHz Intel® Xeon™ processor and a memory of 3 GB. Since the cancerous tissues usually possess more conductivity than the normal tissues, reconstructing conductivity can give a precise location of the cancerous tissues. Reconstructing conductivity in an external imaging geometry has an application in breast cancer imaging and has been studied by various research groups. In the following chapters, a novel internal or trans-rectal imaging geometry which has a potential application in prostate cancer imaging is explored.

CHAPTER V

SOLUTION OF SCALAR EM WAVE AND THERMO-ACOUSTIC WAVE EQUATION IN AN INTERNAL IMAGING GEOMETRY

5.1. Internal imaging geometry: An overview

Internal imaging geometry also known as a trans-rectal geometry is a novel geometry which has a potential application for prostate cancer imaging. In previous chapters, an external imaging geometry which has widely been used by various research groups for breast cancer imaging was discussed. Thermo-acoustic tomography (TAT) for external imaging (Fig. 1.4) and internal imaging geometry (Fig. 1.5) differs in two ways. First, in external imaging geometry, an externally applied electromagnetic source uniformly illuminates the entire surface of the imaging medium, but in internal imaging geometry, the source is likely arranged as either a line or a point illuminator inside the geometry as shown in figure 1.5, therefore the local EM fluence in the geometry is non-uniform and position or depth dependent with respect to the irradiating source. Second, in external imaging geometry, acoustic detectors/receivers are placed as an array across the external boundary of the geometry and enclose the target, but in internal imaging geometry, receivers are placed as an array on a convex boundary which is located below the target and therefore do not enclose the target. Because of the position of the receivers, the visibility of the target by the receivers is limited and the quality of the reconstructed image is target-depth dependent.

5.2. Ultrasonic image of human prostate and resemblance to internal imaging geometry

This section shows the actual ultrasonic image of a human prostate and describes the resemblance of the actual image to an internal or trans-rectal imaging geometry that is used for TAT prostate imaging. Figure 5.1 shows a diagram of human anatomy of the prostate [66] which is located in front of the rectum and below the bladder. Figure 5.2 shows an actual ultrasonic image [67] of the human prostate. An internal or trans-rectal imaging geometry which resembles the actual ultrasonic image of the prostate and rectum set-up was shown in figure 1.5 and is shown again in figure 5.3. The geometry is illuminated by a point EM source located on a convex boundary that resembles the rectum wall. The convex boundary also houses an array of acoustic receivers that capture the acoustic wave generated within the geometry because of EM illumination. A target or a "prostate-tumor" mimicking object is located on top the convex boundary. The object is surrounded by background which can be considered as normal cells (including the bladder).

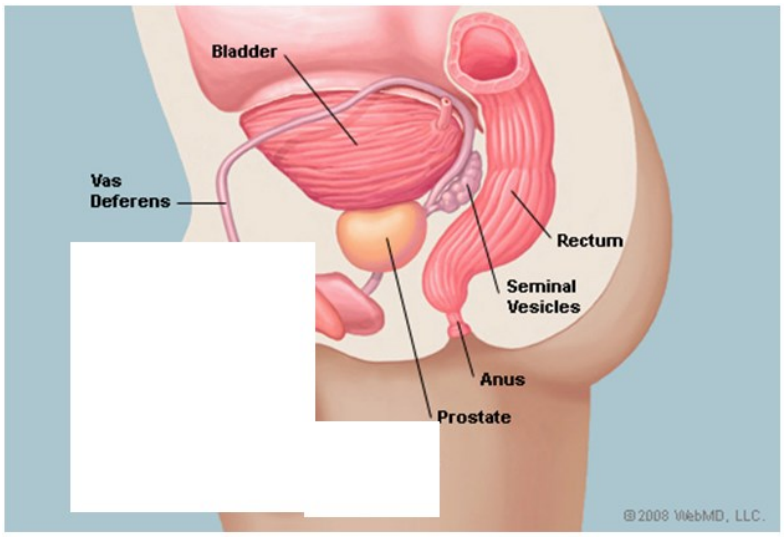

Figure 5.1 Human anatomy of the prostate gland [66]

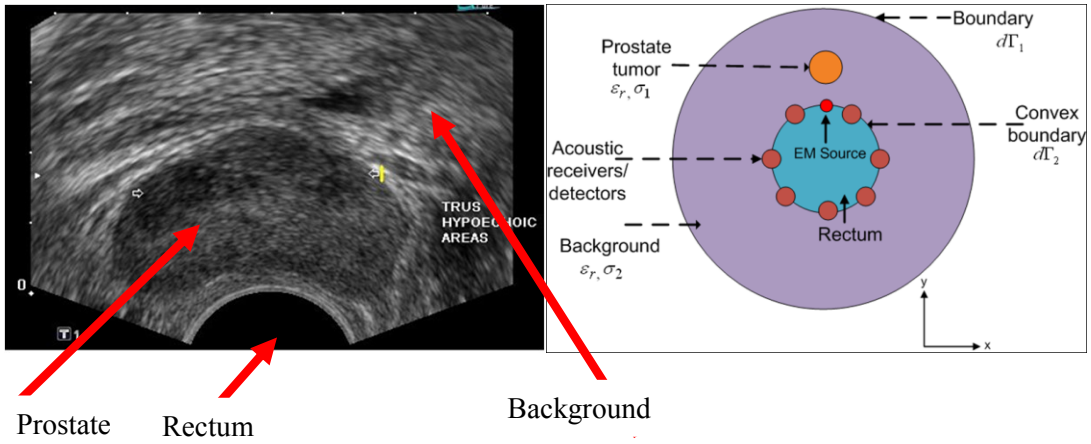

Figure 5.2 Ultrasonic image of Prostate [67]

Figure 5.3 Internal or trans-rectal imaging geometry

5.3. Scattering of EM wave from a trans-rectal or internal imaging geometry

In this section, the electromagnetic (EM) scattering from an internal or trans-rectal imaging geometry is considered. As for an external imaging geometry, computation of the electric field (E-field) is the first step for conductivity reconstruction process in an internal imaging geometry. The scattering analysis in an internal imaging geometry follows the same procedure as external imaging geometry i.e. solving the scalar wave equation using the finite element method to solve for total E-field inside the geometry.

Figure 5.3 shows a trans-rectal or internal imaging geometry which is illuminated by an EM point source located on a convex boundary which can be considered as rectum wall. The boundary also houses an array of acoustic detectors/ receivers that detect acoustic pressure wave generated within the geometry. A target which can be considered as a tumor mimicking object is located on top of the convex boundary. The target and background is characterized by their dielectric constant and conductivity as (εr, σ1) and (εr, σ2) respectively where σ1 < σ2 [68]. In this study, ε_r is considered as 60.5 and σ_1, σ_2 is considered as 0.608 S/m and 1.216 S/m respectively. This permittivity and conductivity is chosen according to the data reported [52] for a normal human prostate at 915MHz.

5.3.1. Finite element formulation [54, 57, 60-62] of the scalar EM wave equation in internal imaging geometry:

The scattering analysis of EM wave from an internal imaging geometry is essentially the same as external geometry which has already been described in details in Chapter II. As for external imaging geometry, the scalar EM wave equation of (2.5) can be solved using the finite element method (FEM) to solve for total E-field inside the internal imaging geometry. The only difference between external and internal imaging geometry in scattering analysis lies in the type and the location of the EM source. In external imaging geometry, an EM plane-wave E_z^{inc} that is incident on the external boundary of the geometry is considered as the illuminating source, while in internal imaging geometry, an EM excitation electric current density that is positioned on the convex boundary inside the geometry is considered as the illuminating source. While solving for E-field inside an internal imaging geometry, equation (2.19) will remain the same but equation (2.20) should be modified accordingly to include the excitation electric current density. The resulted finite element formulation of the EM wave equation for internal imaging geometry can be written as

$$[A]\{e\} = \{b\} \tag{5.1}$$

with the entries of individual matrices are given by,

$$a_{mn} = \iint_{\Gamma} \left(\frac{1}{\mu_r} \nabla B_m \bullet \nabla B_n - k^2 B_m B_n\right) ds - \oint_{\partial\Gamma_1} \frac{1}{\mu_r} \left(\alpha B_m B_n - \beta \frac{\partial B_m}{\partial \phi} \frac{\partial B_n}{\partial \phi}\right) \rho d\phi$$

$$m = 1,2,3 \ldots N$$
$$n = 1,2,3 \ldots N \tag{5.2}$$

$$b_m = -j\omega\mu_0 \iint_{\Gamma} B_m J_{iz}(\vec{r}) ds \tag{5.3}$$

Where α and β are two coefficients given by (2.15) and (2.16) respectively.

For a point excitation source, $J_{iz}(\vec{r}) = \delta(\vec{r} - \vec{r}')$, equation (5.3) can be written as

$$b_m = -j\omega\mu_0 \iint_{\Gamma} B_m \delta(\vec{r} - \vec{r}')ds \tag{5.4}$$

Equation (5.1) along with (5.2) and (5.4) can be solved to find the E-field inside the internal or trans-rectal imaging geometry. For feasibility, a homogeneous Neumann's boundary condition $\frac{\partial E}{\partial n} = 0$ is assumed on the convex boundary $d\Gamma_2$ while solving for the E-field.

5.3.2. Results: Solution of the E-field

In this section, the solution of the E-field inside a trans-rectal geometry for a point source located at 10 mm distance from the center of the geometry is shown. Figure 5.4 shows an internal imaging geometry along with the dimensions. The radius of the convex boundary and background is considered as 10 mm and 40 mm respectively. A target of 3 mm radius is located at 14 mm distance from the center of the geometry. Table 6 summarizes the electrical properties used for the geometry at 915 MHz. The E-field is calculated by solving matrix equation (5.1) using (5.2.) and (5.4). The FEM solution of the E-field is validated with the analytical solution obtained from the Green's function expansion [50] for a homogeneous and lossy trans-rectal geometry with ε_r =60.5 and σ =1.216 S/m considered everywhere throughout the geometry. Figure 5.5 shows the structure of the homogeneous geometry and figure 5.6 shows the analytical solution of the E-field through y =14 mm cut of the geometry. Figure 5.7 shows both the FEM and analytical solution through y =14 mm cut of the geometry. Both the FEM and analytical solution show good agreement. The Green's function solution of E-field for this geometry is given by [50, 58]

$$E_z = -\frac{\omega\mu_0\mu_r}{4} H_0^{(2)}(k|\vec{r} - \vec{r}'|) \tag{5.5}$$

where $H_0^{(2)}()$ is the Hankel's function of 2nd kind and Zeroth order, k is the complex wave number defined in chapter II and $\vec{r}'$ is the position coordinate of the source.

Figure 5.8 shows a non-homogeneous and lossy trans-rectal geometry with an object located at 4 mm depth from the convex boundary and with a different conductivity profile between the target and background. The FEM solution of the E-field through y=14 mm cut of that geometry is shown in figure 5.9.

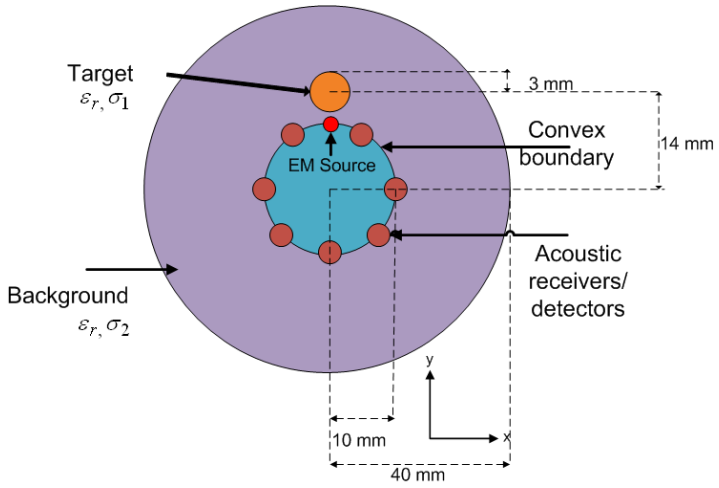

Figure 5.4 Internal imaging geometry along with the dimensions

Table 6: Dimensions and electrical properties used for internal imaging geometry

Medium	Radius (mm)	Relative permeability	Relative permittivity	Conductivity σ (S/m)
Background	40	1	60.5	1.216
Target	3	1	60.5	0.608
Hollow Region	10	1	1	0

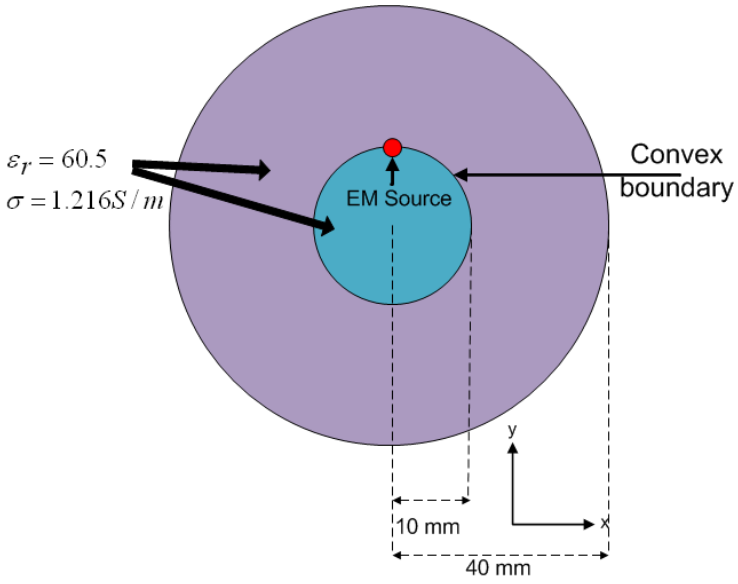

Figure 5.5 Homogeneous and lossy internal imaging or trans-rectal imaging geometry

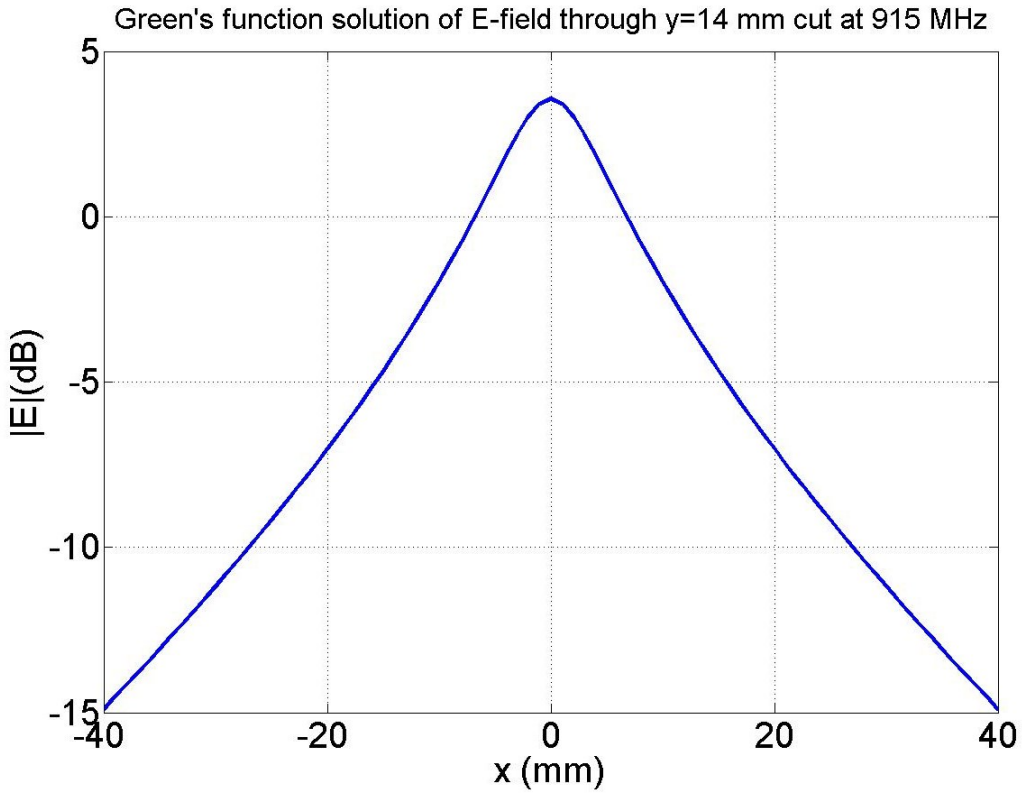

Figure 5.6 Analytical solution of E-field through y =14 mm cut of a point-source stimulated homogeneous geometry.

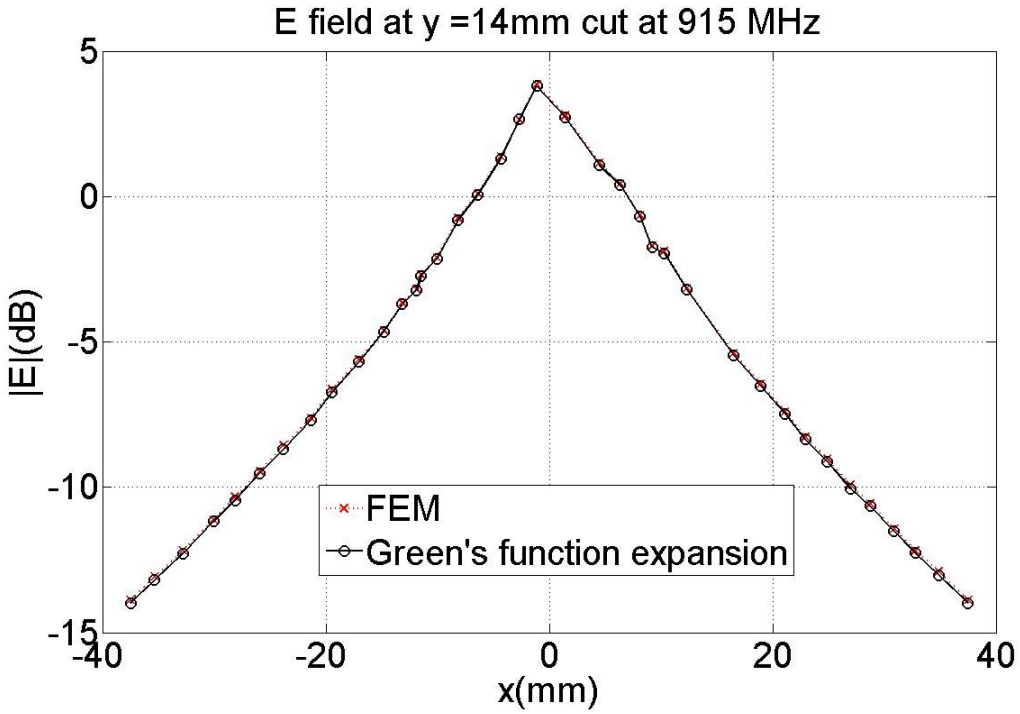

Figure 5.7: FEM and Analytical solution of E-field through y =14 mm cut of a point-source stimulated homogeneous geometry.

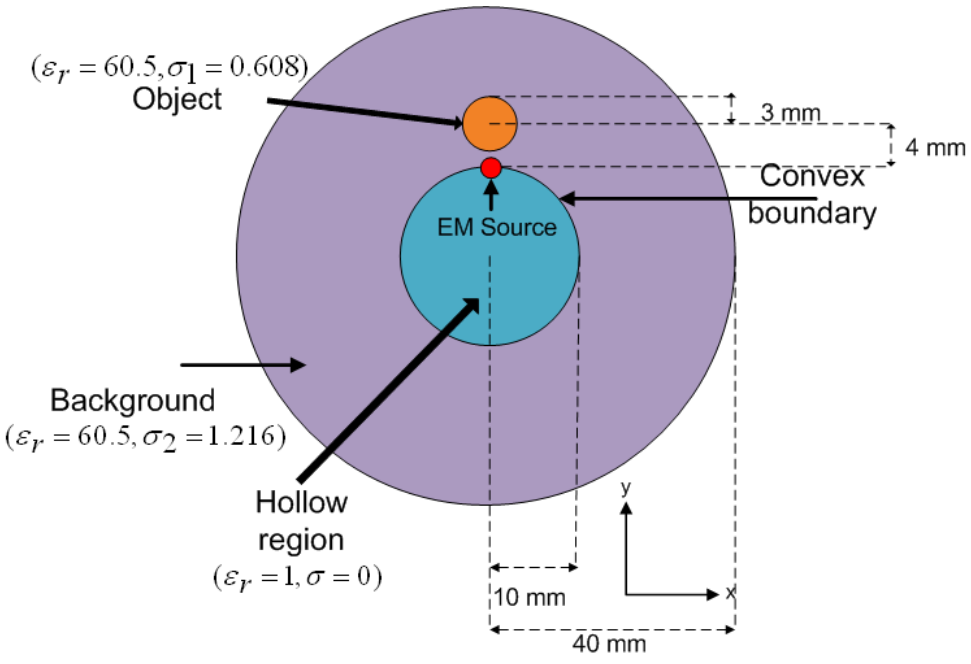

Figure 5.8: Non-homogeneous and lossy trans-rectal geometry with an object located at 4 mm depth

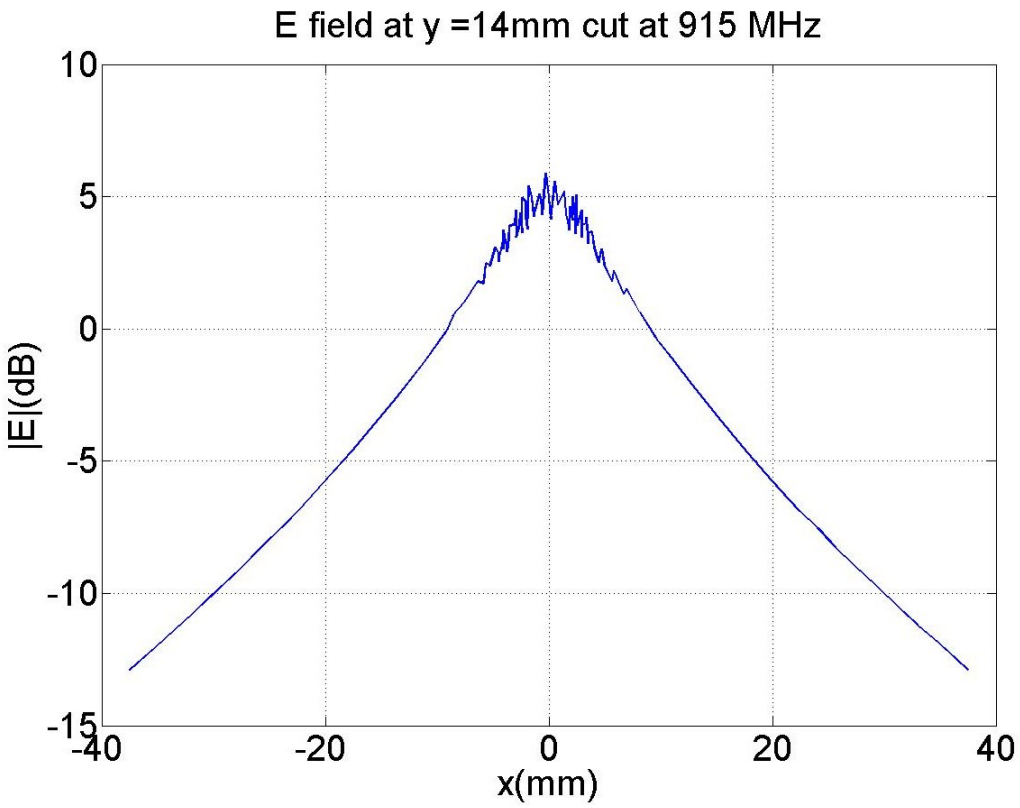

Figure 5.9: FEM Solution of E-field through y =14 mm cut of the non-homogeneous geometry.

5.4. Solution of the thermo-acoustic wave equation in internal imaging geometry

This section shows the solution of the thermo-acoustic wave equation to find the acoustic pressure inside an internal imaging geometry. As for an external imaging geometry described in chapter III, the illumination of internal imaging geometry by an electromagnetic (EM) source gives rise to acoustic/pressure wave inside the geometry via thermo-elastic expansion and follows the same thermo-acoustic wave equation of (3.3). The same procedure as in chapter III is followed to solve the thermo-acoustic wave equation. As for external imaging geometry, solution of this wave equation is the second intermediate step after solving the E-field and power loss density. The finite-element method (FEM) along with Bayliss-Turkel absorbing boundary condition (ABC) is adopted to solve the equation. FEM solution of acoustic pressure is shown at various receiver positions with respect to time.

5.4.1: Results: Solution of the thermo-acoustic wave equation for a target at 4 mm depth

The process of solving thermo-acoustic wave equation for internal or trans-rectal geometry is the same as for external imaging geometry and equations (3.1)-(3.18) are valid for internal imaging geometry as well. So, instead of repeating the entire description of FEM formulation of equation (3.1), only the solution for thermo-acoustic wave equation for internal imaging geometry is shown here.

In this section, the solution of acoustic wave equation for an internal imaging geometry with a target located at 4 mm depth is shown. Figure 5.10 shows the structure of the geometry with a target of 3 mm radius located at 9'o clock position. The distance of the target from the center of the geometry is 14 mm. The radius of the convex boundary is considered as 10 mm. The relative permittivity and conductivity of the target and background is considered as (60.5, 0.608 S/m) and (60.5, 1.216 S/m) respectively at 915 MHz [52]. Three acoustic receivers Rx A, B and C are located at 12'o clock, 9'o clock and 3'o clock position respectively on the convex boundary. Figure 5.11 shows the microwave pulse function that illuminates the geometry. Figure 5.12 shows the calculated acoustic pressure at Rx A, B and C location.

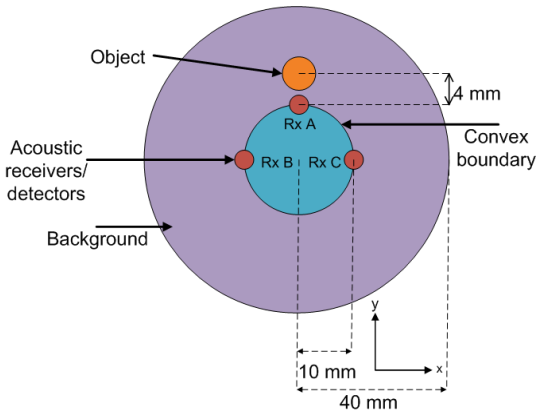

Fig. 5.10 An internal imaging geometry with a target at 4 mm depth and with three receivers located on the convex boundary.

Table 7 summarizes the calculated and actual propagation time of acoustic wave to reach the receivers. The calculated propagation time t_d is determined by $t_d = d / v_{s.}$, where d is the distance from the center of the target to the receiver and $v_{s.}$ = acoustic speed (~1500 m/s is considered). For example, t_d for receiver A is t_d= 4mm/1500e3 ~ 2.7 µs. Actual propagation time is considered after 25 µs when the peak of illuminating pulse occurs. It is worth mentioning that point-receivers are used in this study for feasibility. So, the dimension of the receiver is negligible.

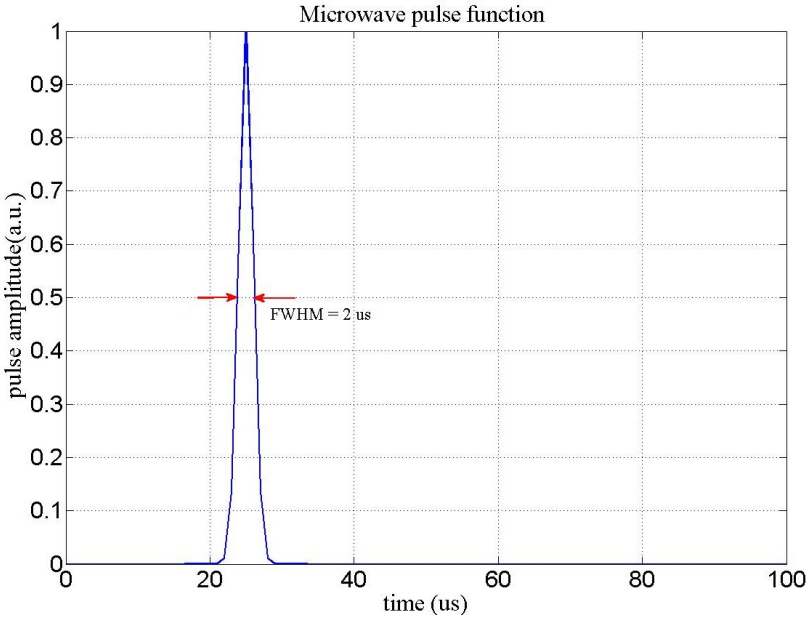

Figure 5.11 Microwave pulse function

Table 7: Calculated and actual propagation time for the acoustic wave to reach different receivers for a target at 4 mm depth

Receivers	Calculated propagation time (µs) from the center of the target to Rx	Actual propagation time (µs) from target to Rx
Rx A	2.7	26-25=1
Rx B	11.5	35-25=10
Rx C	11.5	35-25=10

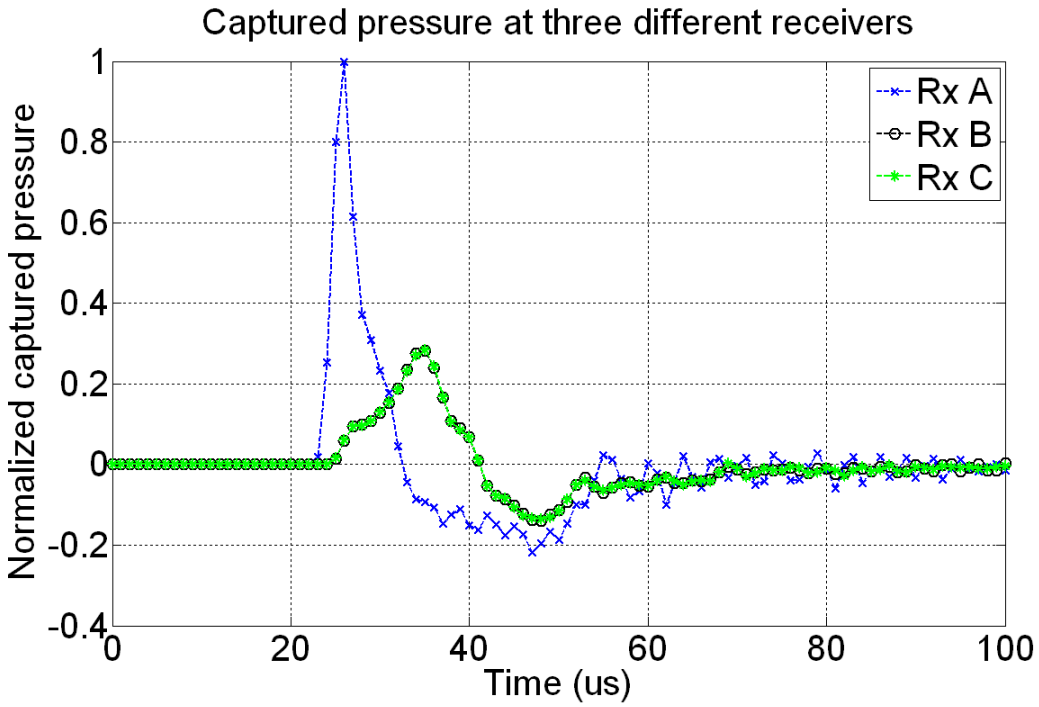

Figure 5.12 Captured acoustic pressure at three receiver locations for a target located at 4 mm depth

Since Rx A is close (4 mm from the center of the target) to the target, acoustic wave generated at the target and captured at Rx A is much stronger and reaches to Rx A earlier (1 μs) than to Rx B or C. Since Rx B and C are located at the same "hypotenuse" distance (~17.2 mm) from the center of the target, the acoustic wave reaches to those receivers at the same time (10 μs). The difference between the actual and calculated propagation time is due to the fact that the calculated propagation time assumes the acoustic wave to propagate from the center of the target, but it actually may propagate from the center or certain point away from the center (e.g. edge) of the target.

5.5. Conclusion

This chapter described the solution of a point source stimulated E-field in an internal-imaging geometry. The scalar EM wave equation was solved using FEM and an absorbing boundary condition. The FEM solution of the E-field was validated with the Green's function solution for a completely homogeneous trans-rectal geometry. As for external imaging geometry, calculation of E-field is the first step of reconstructing conductivity in internal or trans-rectal imaging geometry. This chapter also described the solution of the pressure/acoustic wave using

finite element method (FEM) pertaining to internal-imaging geometry. The calculated acoustic pressure was shown at three different receiver locations. The propagation time of the pressure wave from the object to various receivers varied depending on the distance of the receivers from the object. Since the object/target was considered to be the location from where pressure/acoustic wave was generated, the propagation time of pressure wave to reach the receivers close to the target should be faster than to those located far from the target. The solution of thermo-acoustic wave equation is the second intermediate step after solving the E-field for the TAT image reconstruction algorithm pertaining to the trans-rectal or internal imaging geometry.

CHAPTER VI

RECONSTRUCTION OF CONDUCTIVITY IN AN INTERNAL IMAGING GEOMETRY

6.1. Introduction

This section shows the reconstruction of the conductivity distribution in an internal or trans-rectal imaging geometry. The reconstruction of the conductivity involves finding a "Sensitivity" or "Jacobian" matrix which represents the change in pressure with respect to the change in power loss density. The process of finding the "Jacobian" matrix for internal imaging geometry is the same as for external geometry and follows the same mathematical details. Finding the "Jacobian" and reconstructing the conductivity using the Levenberg-Marquardt regularization technique is the final step to the TAT reconstruction algorithm for an internal imaging geometry. In this chapter, various reconstructed images are shown for single and double objects that are located at different depths from the convex boundary that locates the acoustic receivers and the excitation source. The reconstructed images are shown for excitation frequency of 1 MHz and 915 MHz. The contrast-to-noise ratio or CNR which is an important parameter for determining the detectability of the object is also computed for the object of different radius and with varying ratios of conductivity between the background and object. The effect of various levels of random noise on the reconstructed images is also shown. Finally, certain limitations of the proposed algorithm for detecting the deeper objects are discussed.

6.2. Criterion for choosing the excitation frequency and the dielectric parameters of the object and background

In this in-silico study, an excitation frequency of 915 MHz is used for illuminating the geometry with an EM point source. In TAT, the excitation EM pulses are usually transmitted by a microwave source that operates in the range of microwave frequencies (typically hundreds of MHz to several GHz) [5, 7, 8, 36-38, 40]. It has been reported that the absorption rate of the microwave energy in human tissues at microwave excitation frequencies is substantial [5, 8, 18, 33]. The excitation frequency 915 MHz that is used in this study falls within this frequency range. The conductivity of the object and background is considered as 0.608 S/m and 1.216 S/m respectively. The relative permittivity of both the object and background is considered as 60.5. The conductivity 1.216 S/m and the relative permittivity 60.5 were found [52] for a normal human prostate at an excitation frequency of 915 MHz. However, the exact conductivity and permittivity profile of a cancerous human prostate at microwave excitation frequencies have not been reported so far. Halter et al. [68] reported the exact conductivity profiles of cancerous ex-vivo human prostatic tissues at a frequency range of 10 KHz-1MHz. However, these frequencies fall below the microwave frequency range and at these frequencies, the microwave absorption rate by the tissues is expected to be insignificant and the electrical length (in terms of wavelength) of the EM applicator should be considerably large.

Table 8 lists the reported exact conductivity and relative permittivity profiles of ex-vivo normal and cancerous human prostate for the frequency of 10 KHz and 1 MHz [68]. The ratio of the conductivity and permittivity of normal prostate to cancerous prostate is also shown.

Table 8: Exact permittivity and conductivity of ex-vivo normal and cancerous human prostate at 1 MHz [68]

Frequency (Hz)	Conductivity of normal prostate σ_{nor}	Conductivity of cancerous prostate σ_{can}	$\frac{\sigma_{nor}}{\sigma_{can}}$	Relative permittivity of normal prostate ε_{nor}	Relative permittivity of normal prostate ε_{can}	$\frac{\varepsilon_{nor}}{\varepsilon_{can}}$
10^4	0.901	0.310	2.906	4.49 x 10^5	1.25 x 10^5	3.59
10^6	1.149	0.488	2.35	2180	1880	1.159

It can be observed from table 8 that the normal prostate exhibits higher conductivity and permittivity than the cancerous prostate at 10 KHz and 1 MHz frequency. Also, the ratio of the permittivity and conductivity of normal to cancerous prostate decreases as the excitation frequency increases. As noted earlier, the exact conductivity and relative permittivity of the normal human prostate at 915 MHz is reported as 1.216 S/m and 60.5 respectively. If the conductivity and permittivity of the normal human prostate exhibit the same characteristic (i.e. higher than that of the cancerous prostate with a decreasing ratio) at 915 MHz, the conductivity 0.608 S/m (ratio to the normal prostate is 2.0) and relative permittivity 60.5 (ratio to the normal prostate is 1.0) could be an appropriate choice for cancerous prostate at 915 MHz. However, the measurement of exact conductivity and permittivity profile of the cancerous human prostate at microwave frequencies is subject to further research.

In this chapter, reconstructed images are shown at both 1 MHz and 915 MHz. At 1 MHz, the exact conductivity and permittivity profile of the cancerous and normal human prostate is used. At 915 MHz, the exact conductivity and permittivity profile of the normal prostate and an extrapolated conductivity and permittivity profile of cancerous prostate as discussed before is used.

6.3. The calculation of the contrast-to-noise ratio (CNR)

The contrast-to-noise ratio or CNR is an important parameter that determines the detectability of an object in a reconstructed image. The CNR specific to this study can be defined as

$$\text{CNR}= \frac{CONTRAST}{NOISE} = \frac{|\sigma_{OBJECT} - \sigma_{BACKGROUND}|}{[w_{OBJECT} D_{OBJECT}^2 + w_{BACKGROUND} D_{BACKGROUND}^2]^{1/2}} \tag{6.1}$$

Where σ_{OBJECT} and $\sigma_{BACKGROUND}$ are the mean reconstructed conductivities of the object and background, D_{OBJECT} and $D_{BACKGROUND}$ are the standard deviations of the reconstructed conductivities of the object and background and w_{OBJECT} and $w_{BACKGROUND}$ are the noise weights of the object and background respectively. The noise weights can further be defined as

$$w_{OBJECT} = \frac{AREA_{OBJECT}}{AREA_{OBJECT} + AREA_{BACKGROUND}} \tag{6.2}$$

$$w_{BACKGROUND} = \frac{AREA_{BACKGROUND}}{AREA_{OBJECT} + AREA_{BACKGROUND}} \tag{6.3}$$

Where $AREA_{OBJECT}$ and $AREA_{BACKGROUND}$ are the area of the object and background respectively. In this work, the CNR is shown for the reconstructed images with the objects of different sizes and with different noise levels. A CNR plot is also shown for the objects of different diameters and with varying ratios of conductivity between the object and background.

6.4. Reconstructed conductivity in a trans-rectal geometry

6.4.1: Reconstructed images at 1 MHz with a single target at different depths

In this section, reconstruction of conductivity in an internal imaging geometry at an excitation frequency of 1 MHz is shown. Figure 6.1 A. shows an internal imaging geometry with a single target located 4 mm depth (d). The geometry is illuminated by a point source located at 10 mm on the convex boundary. The excitation frequency is 1 MHz. The FEM mesh used in the geometry is shown in figure 6.1.B.

Table 9 shows the dimensions and electrical properties used for the geometry. The relative permittivity and conductivity that are used for the background and object are reported for an ex-vivo normal and cancerous human prostate respectively at an excitation frequency of 1 MHz.

Table 9: Dimensions and electrical parameters used for the internal imaging geometry with a single target at an excitation frequency of 1 MHz [68]

Medium	Radius (mm)	Relative permeability	Relative permittivity	Conductivity (S/m)
Background	40	1	2180	1.149
Object	3	1	1880	0.488
Hollow region	10	1	1	0

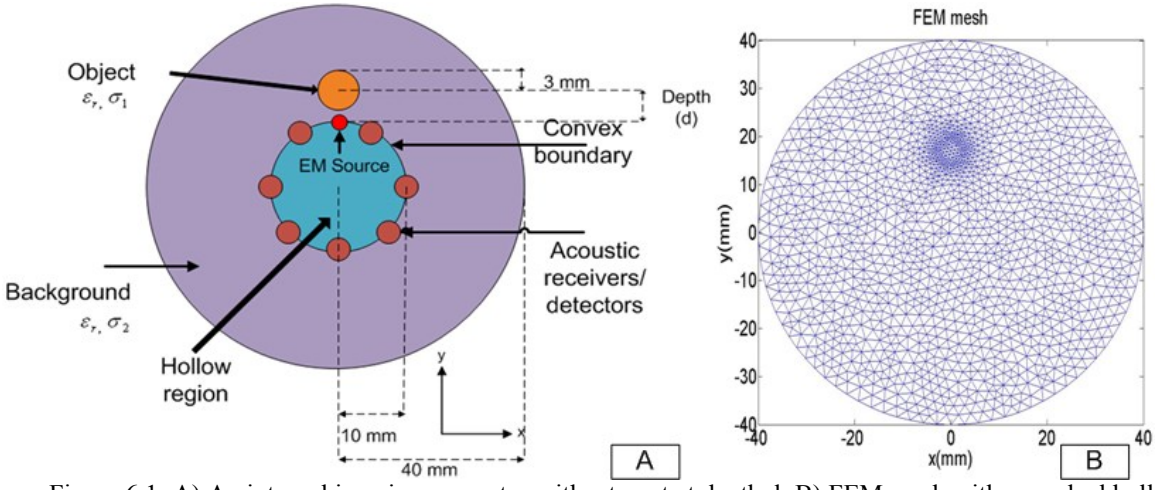

Figure 6.1: A) An internal imaging geometry with a target at depth d. B) FEM mesh with a meshed hollow region

Figures 6.2.A, B, C, and D show the images of true conductivity profile for a single target located at 4 mm, 7 mm, 10 mm and 15 mm depth respectively. The true conductivity profile serves the purpose of calculating the true E-field and hence the power loss density and true or "measured" acoustic pressure p_t^m as described by steps 1.C-D in section 1.7 of chapter I. Figures 6.2 E, F, G and H show the images of corresponding reconstructed conductivity profile and figures 6.2 I, J, K and L show the corresponding line plots of true and reconstructed conductivity profile through y-cut. Table 10 summarizes the maximum reconstructed conductivities and the percentage errors for the object/target at different depths. Maximum reconstructed conductivities are 0.4445 S/m, 0.5257 S/m, 0.6038 S/m and 0.7409 S/m for the object located at 4, 7, 10 and 15 mm depth respectively. For all the reconstructed images as shown in figure 6.2, 1% Gaussian random noise is added to the true or "measured" acoustic pressure p_t^m .

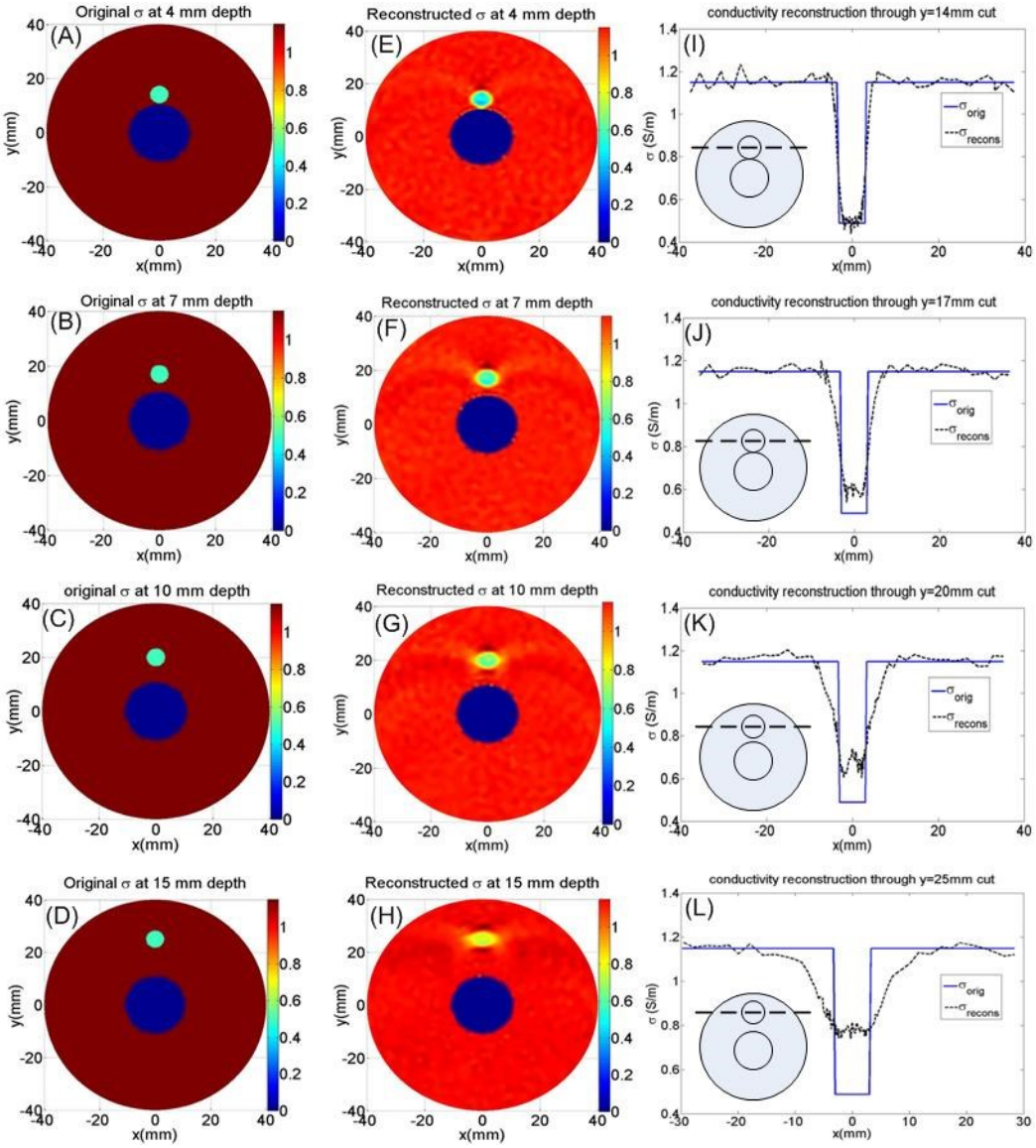

Figures 6.2 (A, B, C and D): Images of true conductivity (σ) profile for object at 4 mm, 7 mm, 10 mm and 15 mm depth (d) respectively. (E, F, G and H): Images of corresponding reconstructed conductivity profile at 1 MHz. (I, J, K and L) : Corresponding line plot of true (solid line) and reconstructed conductivity (dashed line) profile through y =14 mm, 17 mm, 20 mm and 25 mm cut respectively at 1MHz.

Table 10: Reconstructed conductivity and % error at 1 MHz for a single object of 3 mm radius located at different depths

Object depth (mm)	σ_{orig} (S/m)	σ_{recons} (S/m)	% error (absolute)
4	0.488	0.4445	8.91
7	0.488	0.5257	7.73
10	0.488	0.6038	23.73
15	0.488	0.7409	52

6.4.2: Reconstructed images at 1 MHz with double objects/targets at different depths

This section describes the reconstruction of conductivity at 1 MHz in an internal imaging geometry with two targets located at different depths. The dimensions and dielectric properties used for this geometry are the same as for the geometry with a single target as listed in table 8. Both the objects have the same relative permittivity and conductivity.

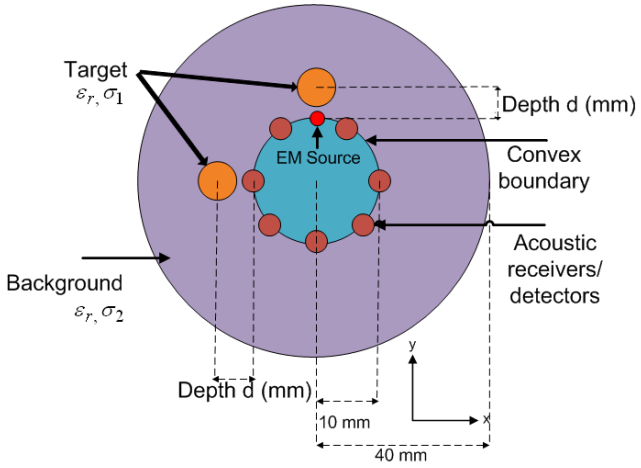

Figure 6.3: An internal imaging geometry with two targets at a depth d

Figure 6.3 shows an internal imaging geometry with two targets at 9'o clock and 12'o clock position at a depth d. Figures 6.4.A, B, C, D show the images of the true conductivity profile for targets located at 4 mm, 7 mm, 10 mm and 15 mm depth respectively. Figures 6.4 E, F, G and H show the images of corresponding reconstructed conductivity profile. Figures 6.5 A-D and E-H show the line plots of true and reconstructed conductivity profile through y and x cut respectively. Maximum reconstructed conductivities are 0.4470 S/m, 0.5260 S/m, 0.6289 S/m and 0.6930 S/m for the object located at 9'0 clock position at 4, 7, 10 and 15 mm depth respectively and 0.4397 S/m, 0.5402 S/m, 0.6216 S/m and 0.7506 S/m for the object located at 12'0 clock position at 4, 7, 10 and 15 mm depth respectively. Table 11 and 12 summarizes maximum reconstructed conductivities and the percentage errors for the two targets at different depths.

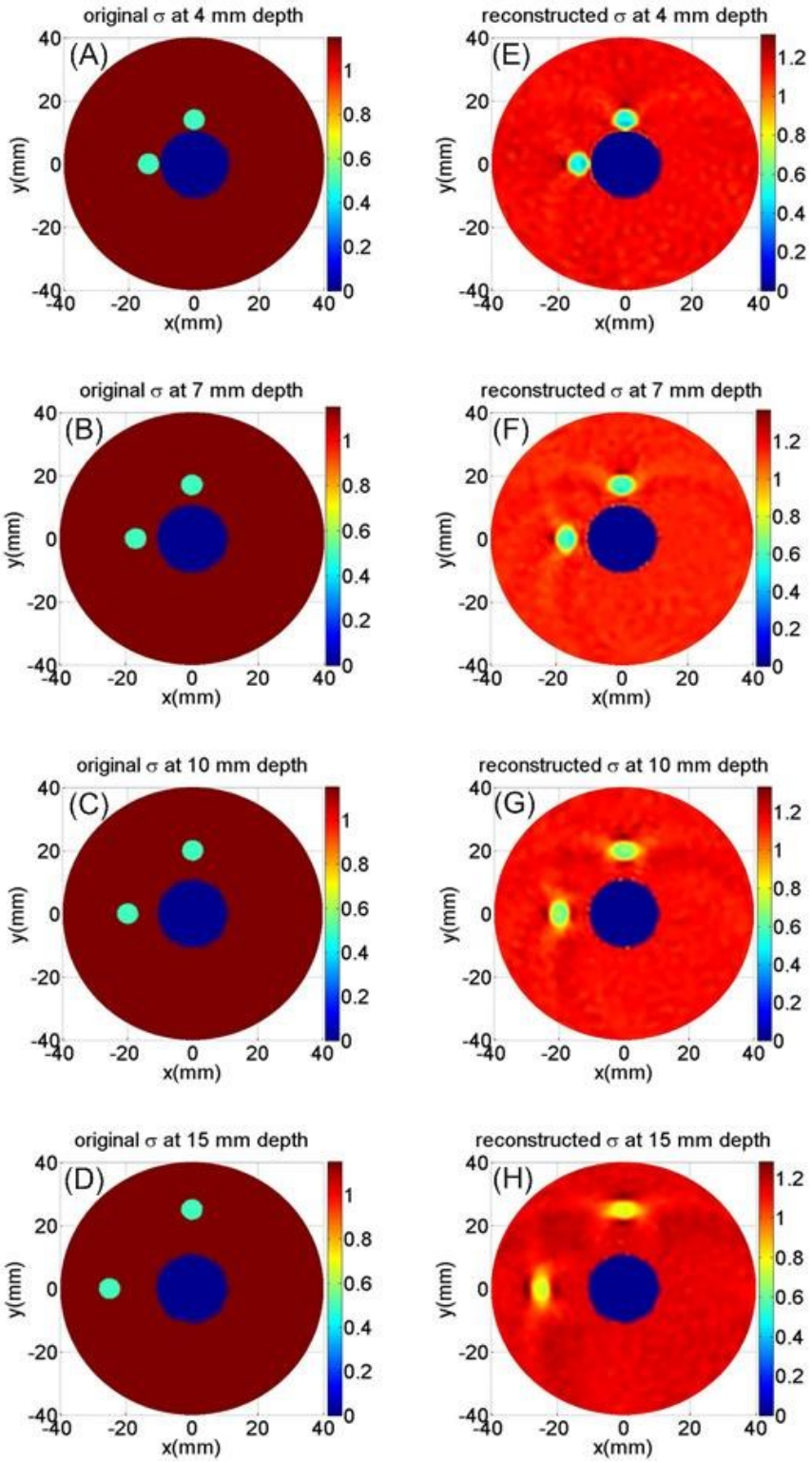

Figures 6.4 (A, B, C and D): Images of the true conductivity (σ) profile for two objects at 4 mm, 7 mm, 10 mm and 15 mm depth (d) respectively. (E, F, G and H): Images of the corresponding reconstructed conductivity profile at 1MHz.

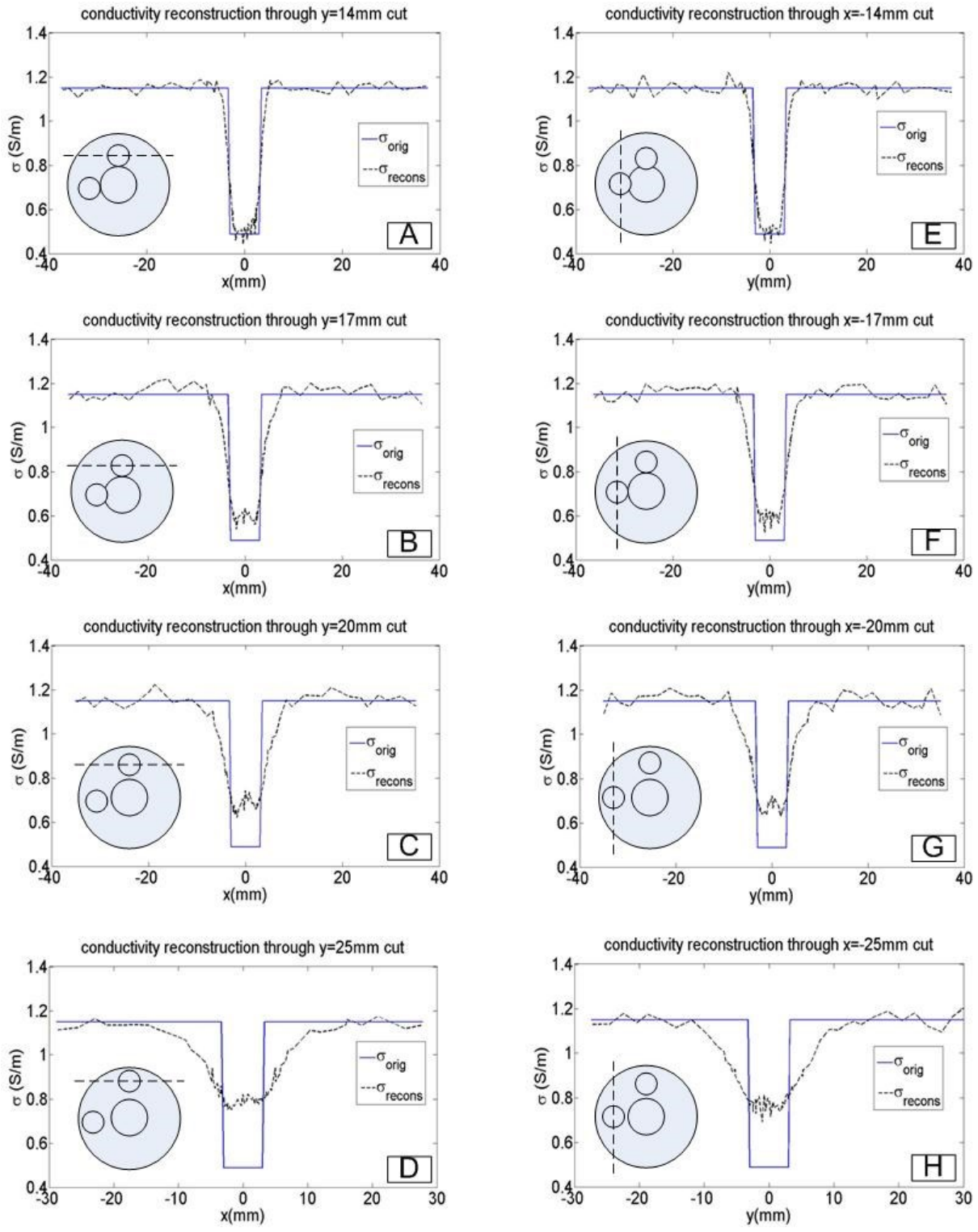

Figures 6.5 (A, B, C and D): Line plots of reconstructed conductivity profile through y =14 mm, 17 mm, 20 mm and 25 mm cut respectively. (E, F, G and H): Line plots of true (solid line) and reconstructed conductivity (dashed line) profile through x = - 14 mm, - 17 mm, - 20 mm and - 25 mm cut respectively.

Table 11: Reconstructed conductivity, % error at 1 MHz for two objects of 3 mm radius and for the object located at 9'0 clock position at different depths

Object depth (mm)	σ_{orig} (S/m)	σ_{recons} (S/m)	% error (absolute)
4	0.488	0.4470	8.40
7	0.488	0.5260	7.79
10	0.488	0.6289	28
15	0.488	0.6930	42

Table 12: Reconstructed conductivity, % error at 1 MHz for two objects of 3 mm radius and for the object located at 12'0 clock position at different depths

Object depth (mm)	σ_{orig} (S/m)	σ_{recons} (S/m)	% error (absolute)
4	0.488	0.4397	9.90
7	0.488	0.5402	10.70
10	0.488	0.6216	27.38
15	0.488	0.7506	53.81

6.4.3: Reconstructed images at 915 MHz with a single target/object at different depths

In this section, reconstruction of conductivity in an internal imaging geometry at an excitation frequency of 915 MHz is shown. Although the dimension of the geometry remains the same, the dielectric parameter (i.e. relative permittivity and conductivity) of the background and object changes along with the excitation frequency. Table 13 listed the dimensions and dielectric parameters used for the geometry at 915 MHz. The chosen dielectric parameters for the background and object at 915 MHz are based on the reported conductivity and permittivity profile for a normal human prostate [52] and the extrapolated conductivity and permittivity profile for a cancerous human prostate as discussed in section 6.2.

Table 13: Dimensions and electrical parameters used for the internal imaging geometry with a single target at an excitation frequency of 915 MHz [52]

Medium	Radius (mm)	Relative permeability	Relative permittivity	Conductivity (S/m)
Background	40	1	60.5	1.216
Object	3	1	60.5	0.608
Hollow region	10	1	1	0

Figures 6.6.A, B, C, and D show the images of true conductivity profile for a single target located at 4 mm, 7 mm, 10 mm and 15 mm depth respectively. Figures 6.6 E, F, G and H show the images of corresponding reconstructed conductivity profile and figures 6.6 I, J, K and L show the corresponding line plots of true and reconstructed conductivity profile through y-cut. Table 14 summarizes the maximum reconstructed conductivities and the percentage errors for the object/target at different depths. Maximum reconstructed conductivities are 0.5592 S/m, 0.6652 S/m, 0.6969 S/m and 0.8237 S/m for the object located at 4, 7, 10 and 15 mm depth respectively. For all the reconstructed images as shown in figure 6.6, 1% Gaussian random noise is added to the true or "measured" acoustic pressure p_t^m .

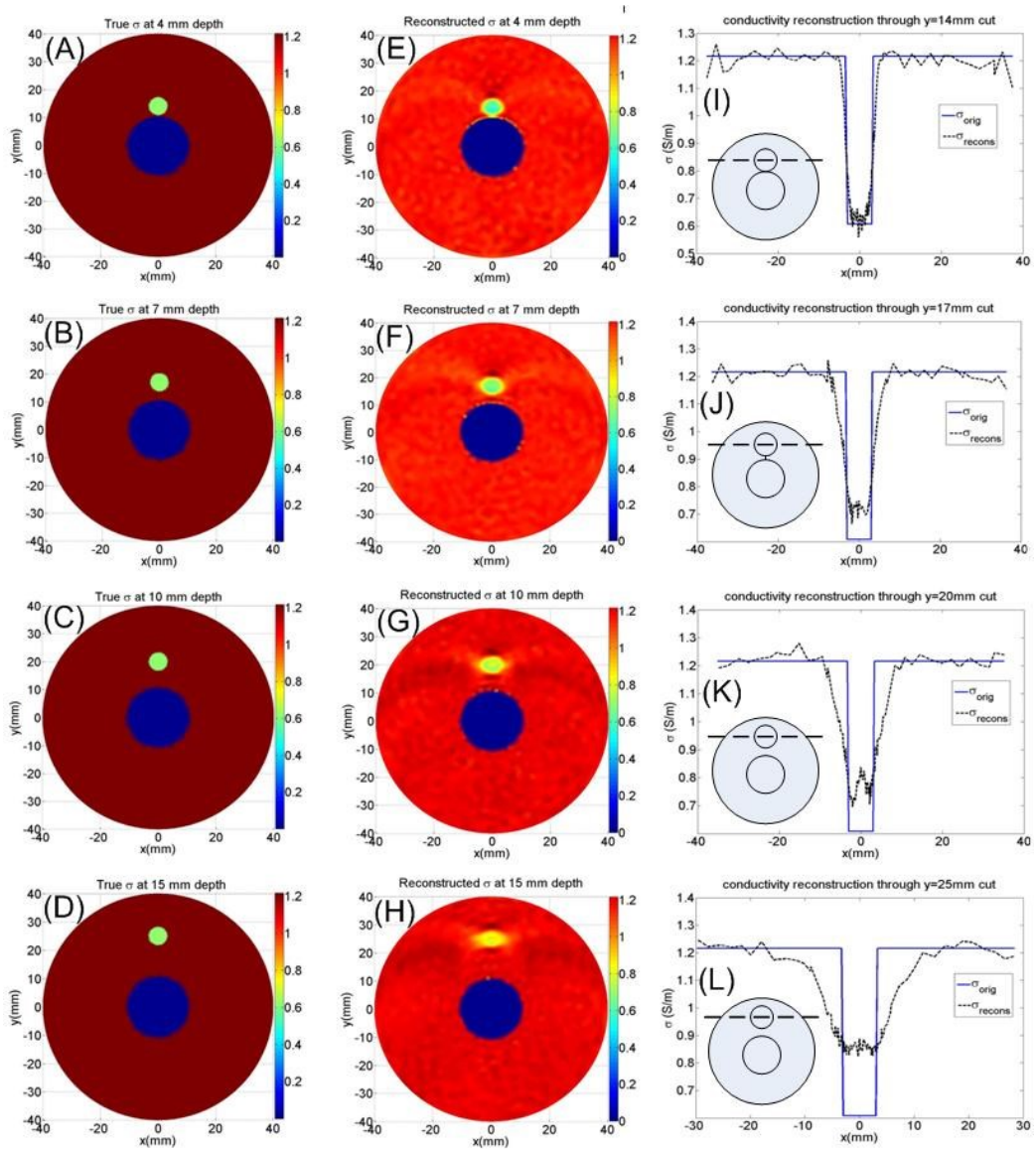

Figures 6.6 (A, B, C and D): Images of true conductivity (σ) profile for object at 4 mm, 7 mm, 10 mm and 15 mm depth (d) respectively. (E, F, G and H): Images of corresponding reconstructed conductivity profile at 915 MHz. (I, J, K and L) : Corresponding line plot of true (solid line) and reconstructed conductivity (dashed line) profile through y =14 mm, 17 mm, 20 mm and 25 mm cut respectively at 915 MHz.

Table 14: Reconstructed conductivity and % error at 915 MHz for a single object of 3 mm radius located at different depths

Object depth (mm)	σ_{orig} (S/m)	σ_{recons} (S/m)	% error
4	0.608	0.5592	8.03
7	0.608	0.6652	9.41
10	0.608	0.6969	14.62
15	0.608	0.8237	35.48

6.4.4: Reconstructed images at 915 MHz with double targets/objects at different depths

This section describes the reconstruction of conductivity at 915 MHz in an internal imaging geometry with two targets located at different depths. The geometry is shown in figure 6.3. The dimensions and dielectric properties used for this geometry are the same as for the geometry with a single target as listed in table 13. Both the objects in the geometry have the same relative permittivity and conductivity.

Figures 6.7.A, B, C and D show the images of the true conductivity profile for targets located at 4 mm, 7 mm, 10 mm and 15 mm depth respectively. Figures 6.7 E, F, G and H show the images of corresponding reconstructed conductivity profile. Figures 6.8 A-D and E-H show the line plots of true and reconstructed conductivity profile through y and x cut respectively. Maximum reconstructed conductivities are 0.5655 S/m, 0.6560 S/m, 0.7159 S/m and 0.7873 S/m for the object located at 9'0 clock position at 4, 7, 10 and 15 mm depth respectively and 0.5487 S/m, 0.6666 S/m, 0.7068 S/m and 0.8306 S/m for the object located at 12'0 clock position at 4, 7, 10 and 15 mm depth respectively. Table 15 and 16 summarizes maximum reconstructed conductivities and the percentage errors for the two targets at different depths.

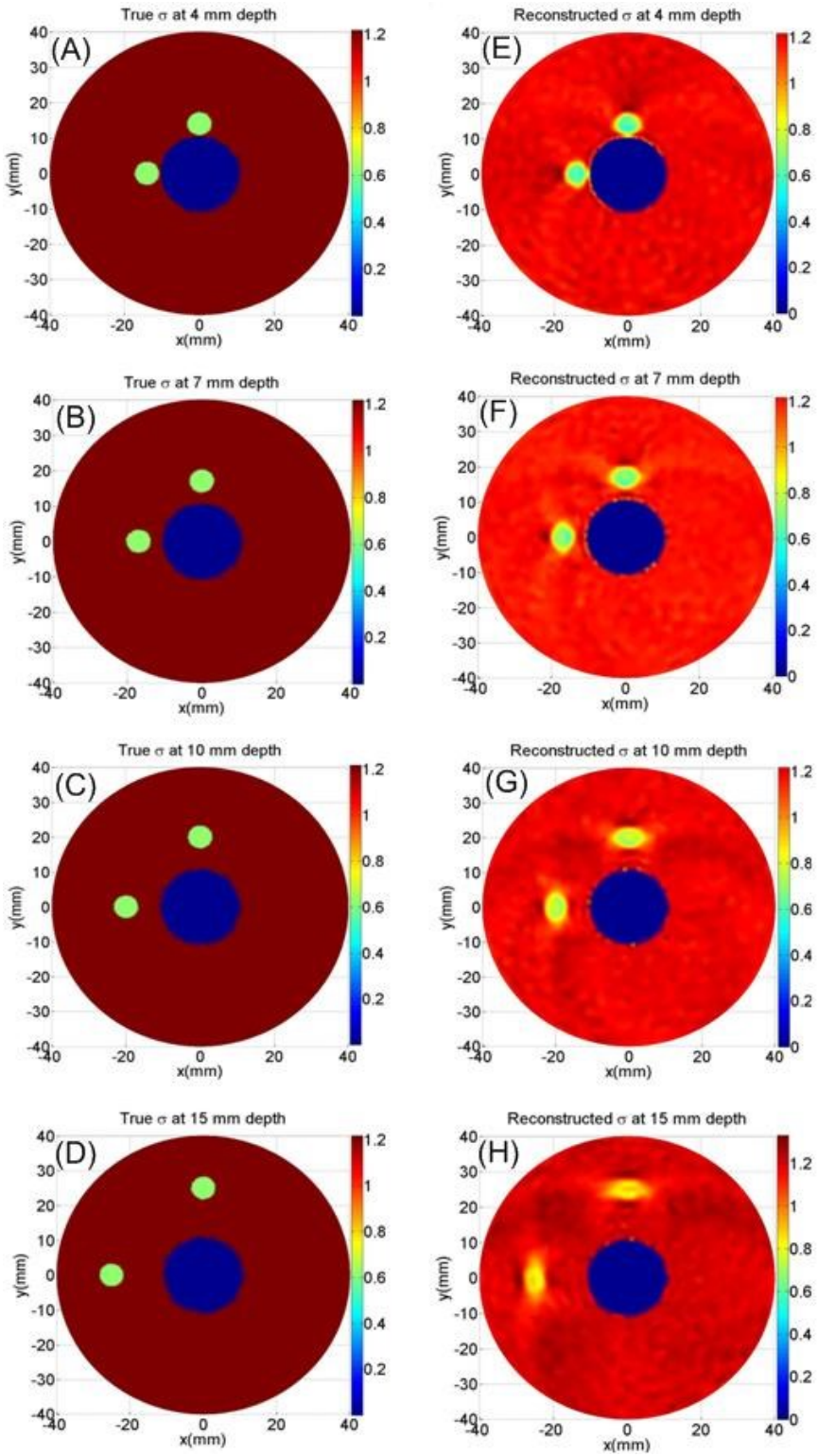

Figures 6.7 (A, B, C and D): Images of the true conductivity (σ) profile for two objects at 4 mm, 7 mm, 10 mm and 15 mm depth (d) respectively. (E, F, G and H): Images of the corresponding reconstructed conductivity profile at 915 MHz.

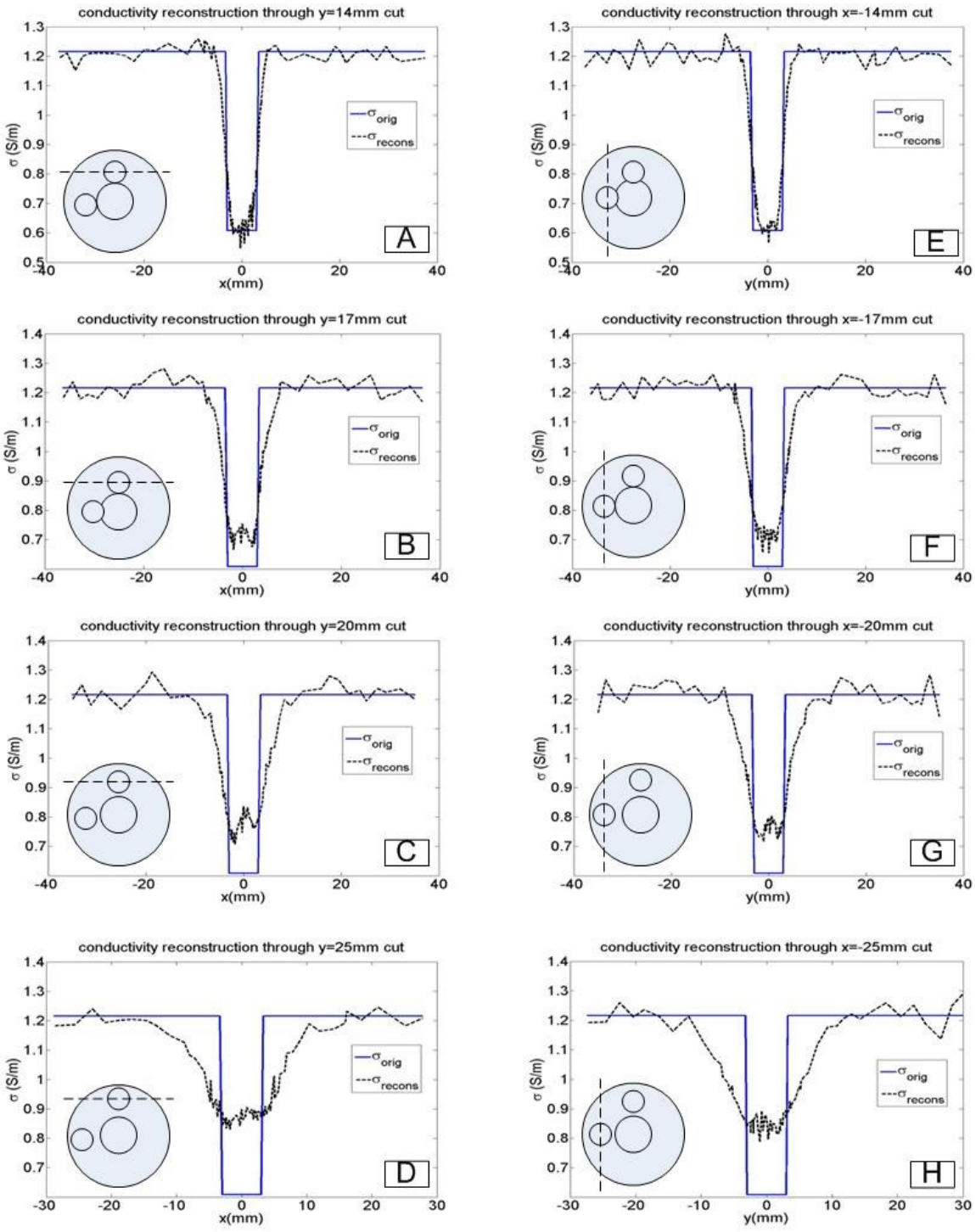

Figures 6.8 (A, B, C and D): Line plots of reconstructed conductivity profile through y =14 mm, 17 mm, 20 mm and 25 mm cut respectively. (E, F, G and H): Line plots of true (solid line) and reconstructed conductivity (dashed line) profile through x = - 14 mm, - 17 mm, - 20 mm and - 25 mm cut respectively.

Table 15: Reconstructed conductivity, % error at 915 MHz for two objects of 3 mm radius and for the object located at 9'0 clock position at different depths

Object depth (mm)	σ_{orig} (S/m)	σ_{recons} (S/m)	% error
4	0.608	0.5655	6.99
7	0.608	0.6560	7.89
10	0.608	0.7159	17.75
15	0.608	0.7873	29.49

Table 16: Reconstructed conductivity, % error at 915 MHz for two objects of 3 mm radius and for the object located at 12'0 clock position at different depths

Object depth (mm)	σ_{orig} (S/m)	σ_{recons} (S/m)	% error
4	0.608	0.5588	8.09
7	0.608	0.6666	9.64
10	0.608	0.7068	16.25
15	0.608	0.8306	36.61

6.5. Criterion for selecting the object radius

In this work, a radius of 3 mm is chosen for the tumor-like objects. This selected radius is based on the contrast-to-noise ratio (CNR) of the reconstructed image. Figures 6.9 A, B and C show the images of the true conductivity profile with a 1:2 ratio of conductivity between the object and background at 915 MHz and with an object of 1 mm, 2 mm and 3 mm radius respectively. Figures 6.9 D, E and F show the corresponding reconstructed images at 915 MHz and figures 6.9 G, H, and I show the corresponding line profiles of the true and reconstructed conductivity through y =12 mm, 13 mm and 14 mm cut respectively. Table 17 shows the calculated percentage error between the true and reconstructed conductivity and the contrast-to-noise ratio (CNR) of the reconstructed images. It can be observed the CNRs that the 3 mm radius provides the highest CNR among 1, 2 and 3 mm objects.

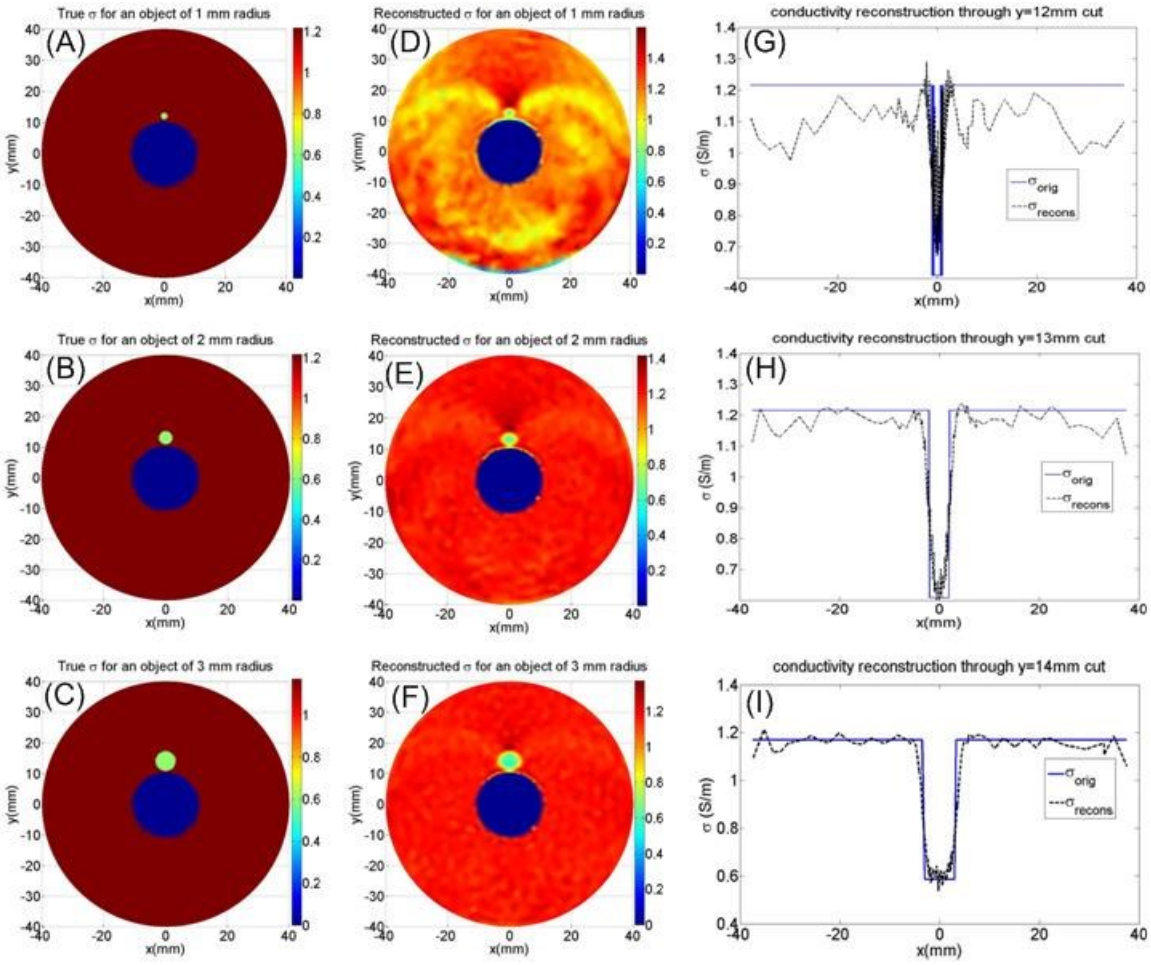

Figure-6.9 (A, B and C): Images of true conductivity profile for a single object of radius 1 mm, 2 mm and 3 mm respectively. (D, E and F): Corresponding images of reconstructed conductivity profile at 915 MHz. (G, H and I): Corresponding line plots of true and reconstructed conductivity profile through y =12 mm, 13 mm and 14 mm cut respectively.

Table 17: Reconstructed conductivity, % error and CNR at 915 MHz for a single object of different sizes

Object radius (mm)	σ_{orig} (S/m)	σ_{recons} (S/m)	% error	CNR
1	0.608	0.6713	10.41	1.1843
2	0.608	0.6007	1.20	1.7307
3	0.608	0.5592	8.03	2.1167

6.6. The effect of random noise on the reconstructed images

For all the reconstructed images pertaining to trans-rectal geometry shown previously, 1% Gaussian noise is added to the forward solution of the true acoustic pressure. Although 1% noise was used as a standard level of noise for the finite element method (FEM) based breast and prostate

simulations [69, 70], the effect of higher levels of noise on the reconstructed images is also explored in this work. Figure 6.10.A shows an image of the true conductivity profile with two objects of 3 mm radius located 4 mm depth and figures 6.10.B, C and D show the reconstructed images at 915 MHz with 1%, 10% and 20% level of Gaussian noise. Table 18 and 19 show the maximum reconstructed conductivities, the percentage errors and the CNRs for the reconstructed images with different levels of noise and for the objects located at 9'o clock and 12'o clock position respectively. It can be observed from the table that the percentage error between the true and reconstructed conductivity increases and the CNR degrades with an increasing level of noise.

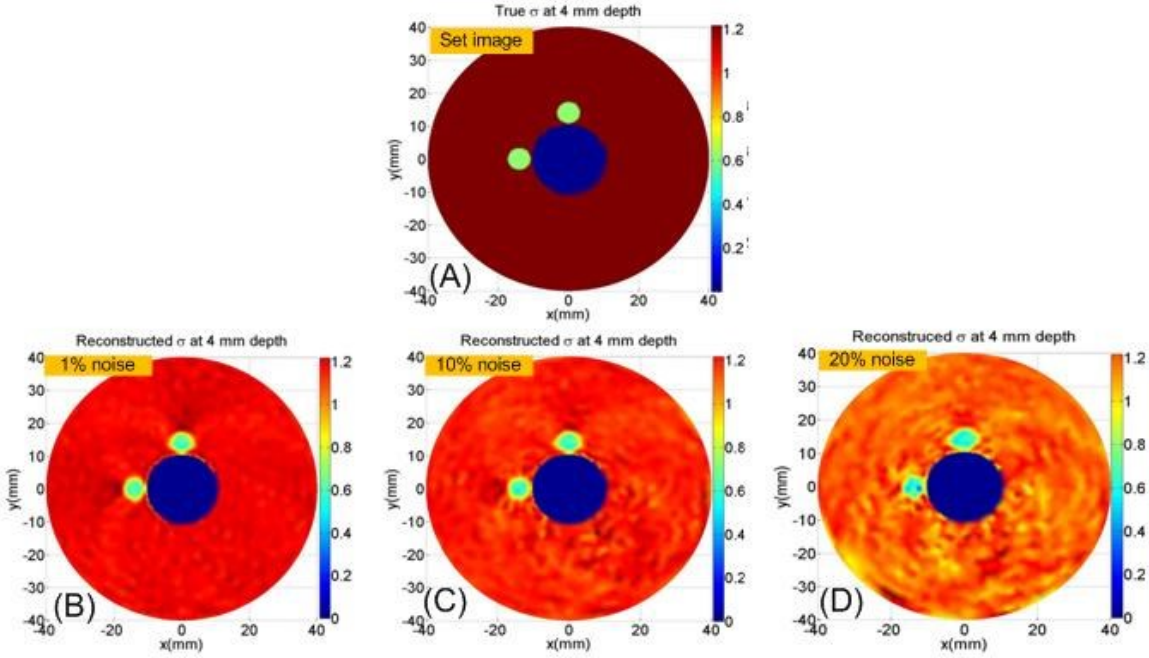

Figure-6.10 (A): Image of true conductivity profile for two objects located at 4 mm depth. (B, C and D): Corresponding images of reconstructed conductivity profile at 915 MHz with 1%, 5% and 10% noise added to the forward solution of the true acoustic pressure.

Table 18: Reconstructed conductivity, % error and CNR at 915 MHz with different noise levels for two objects of 3 mm radius and for the object located at 9'o clock position

Noise level	σ_{orig} (S/m)	σ_{recons} (S/m)	% error	CNR
1%	0.608	0.5655	6.99	2.027
10%	0.608	0.5306	12.73	1.9495
20%	0.608	0.4882	19.70	1.8882

Table 19: Reconstructed conductivity, % error and CNR at 915 MHz with different noise levels for two objects of 3 mm radius and for the object located at 12'o clock position

Noise level	σ_{orig} (S/m)	σ_{recons} (S/m)	% error	CNR
1%	0.608	0.5588	8.09	2.027
10%	0.608	0.5487	9.75	1.9495
20%	0.608	0.5249	13.67	1.8882

6.7. The computation of the contrast-to-noise ratio (CNR)

In this study, the contrast-to-noise ratio (CNR) is calculated at 915 MHz using (6.1)-(6.3) for the reconstructed images pertaining to trans-rectal or internal imaging geometry. A CNR plot is shown in figure 6.11 for a single object of different radii and with varying ratios of conductivity between the object and background. The lower boundary of the object is located at 1 mm distance from the top of the convex boundary. 1% Gaussian noise is added to the forward solution of the true acoustic pressure. A maximum CNR of 3.6797 is computed for an object of 3 mm radius and with a conductivity ratio of 10:1 between the background and object while a minimum CNR of 1.18 is computed for an object of 1 mm radius with a conductivity ratio of 2:1 between the background and object. Upon comparing the detectability of the object in the reconstructed images as shown in figures 6.9 and 6.10 and the calculated CNR as listed in table 16-18, CNRs of 1.7 and 1.9 can be considered as threshold CNRs for an acceptable detectability of single and double objects respectively in a trans-rectal geometry.

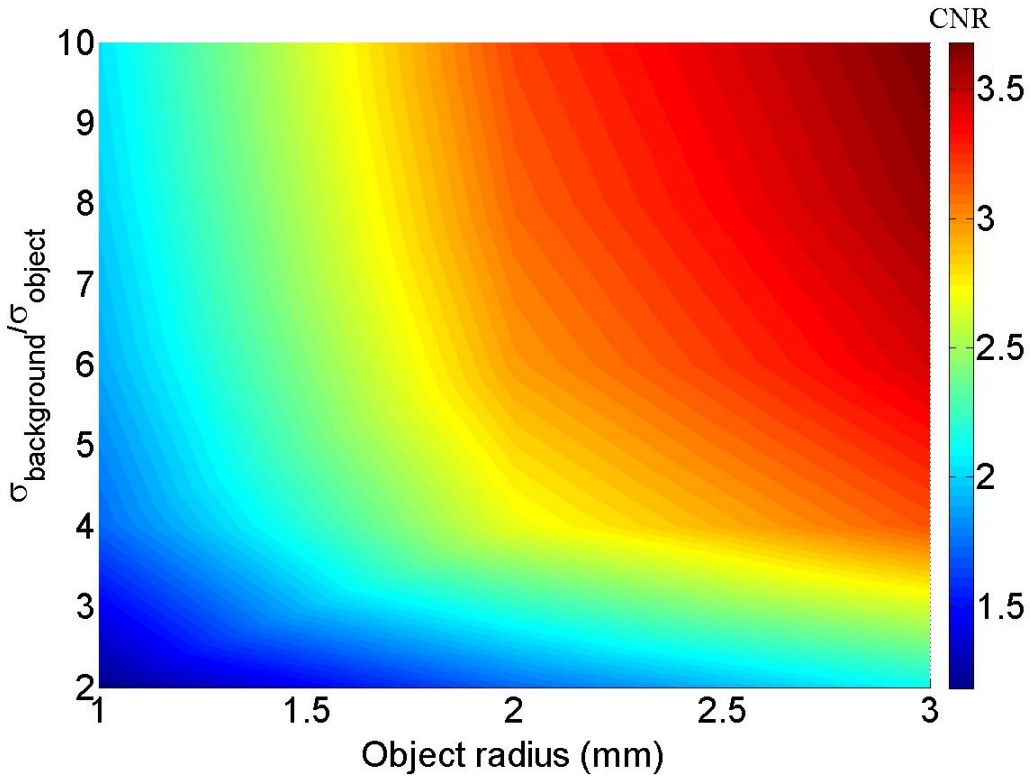

Figure-6.11: Calculated contrast-to-noise ratio (CNR) at 915 MHz for a single object of different diameters and with a different ratios of conductivity between the object and background. The lower boundary of the object is located at 1 mm distance from the top of the convex boundary.

6.8. Discussion

In this study, a TAT based reconstruction algorithm was presented for reconstructing the heterogeneous conductivity distribution in a trans-rectal geometry for potential application in prostate imaging. The geometry was illuminated by an EM point source located on a convex trans-rectal applicator that also houses an array of point ultrasonic receivers. The resultant E-field distribution inside the geometry was computed by solving the scalar EM wave equation using the finite element method (FEM). The captured acoustic pressure generated inside the geometry as a result of EM illumination was also computed in time-domain and various reconstructed images based on different conductivity profiles between the object and background were shown. An object that had a higher conductivity absorbed more microwave energy and was considered to be the origin of the acoustic pressure wave. The propagation time of the acoustic wave to reach a receiver from

an object depended on the distance of that receiver from the object. As shown in figures 5.9 and 5.11, since Rx A was located closest to the object, the acoustic pressure captured at Rx A was much stronger and the peak of the acoustic pressure originated from the object reached Rx A earlier than Rx B or C. Since Rx B and C were located at the same longitudinal distance from the object, both the magnitude of the captured acoustic pressure and the propagation time for the acoustic wave to reach Rx B or C from the object were the same as shown in figure 5.11.

Figures 6.2, 6.4-6.8 showed various images and line-profiles of the reconstructed conductivity for single and double objects of 3 mm radius positioned at different depths and with a 1:2 conductivity ratio between the object and background. As can be seen from the reconstructed images, trans-rectal TAT can locate the position of the tumor-mimicking objects with a high to moderate contrast and resolution depending on the depth of the objects. For the objects that were located closest to the acoustic receiver, the image reconstruction was the most accurate as indicated by the percentage errors between the true and reconstructed conductivity of the object and the contrast-to-noise ratios (CNRs) of the reconstructed images. The difference between the true and reconstructed conductivity increased as the depth of the objects increased or as objects moved away from the receivers. The weakening of the captured acoustic pressure at a fixed receiver with an increasing depth of the object most likely caused an increasing percentage error between the true and reconstructed conductivity.

One limitation of the trans-rectal TAT is the location of the acoustic receivers that affects the quality of the reconstructed image. For TAT pertaining to a trans-rectal or internal imaging geometry as shown in figure 6.1 and 6.3, the acoustic receivers are placed on a convex boundary that is located below the object and is enclosed by the background as opposed to the TAT for breast imaging or external imaging geometry as shown in figure 4.1 where all the acoustic receivers are placed on a boundary that encloses both the object and background.

The effect of the location of the acoustic receivers is explored in figure 6.12. Figure 6.12.A shows a geometry where the EM point source is located on the rectum wall or convex boundary but the acoustic receivers are moved from the rectum wall to a boundary that is enclosing both the object and background. Figure 6.12.B shows an image of the true conductivity profile with an object of 3 mm radius located at 15 mm depth. Figure 6.12.C shows the corresponding reconstructed image at 1MHz. Figure 6.12.D shows a trans-rectal geometry with both the EM point source and acoustic receivers located on the rectum wall below the object. Figure 6.12.E shows the image of the true conductivity profile with the same object located at 15 mm depth and figure 6.12.F shows the corresponding reconstructed image at 1 MHz. Figures 6.12.G and H show the line plots of reconstructed conductivity for the reconstructed images C and F respectively. It can be observed from figures 6.12.C and F that the location of the acoustic receivers impacts the quality of the reconstructed image. For figure 6.12.C, where the acoustic receivers enclose the object and background, the shape of the object is considerably preserved and the artifacts in the background are minimized while for figure 6.12.F, where the acoustic receivers are located below the object, the shape of the object is elongated and the reconstructed image has some visible artifacts.

Positioning the receivers on a boundary that encloses both the object and background gives receivers a better detection view or line-of-sight of the object and background as opposed to the limited view of by the receivers that are located on a convex boundary below the object.

Because of better detection view, the acoustic wave that contains information about the dielectric contrast of the object and background is evenly captured by most of the receivers. This results in a high contrast and spatial resolution of the reconstructed image and the reduced artifacts in the background as shown by figure 6.12.C. The elongation of the object shape is also caused by the limited line-of-sight or detection view of the object by the receivers in a trans-rectal geometry. For acoustic receivers that are not completely out of the sight of the object, the more laterally displaced receivers (e.g. Rx B or C in figure 5.9) with respect to the object have the more limitation

on the line-of-sight of the object boundary. This limited line-of-sight causes an uneven receiving of the acoustic wave by the receivers which in turn changes the temporal profile of the captured acoustic pressure and hence the shape of the reconstructed object. For all the reconstructed images pertaining to trans-rectal geometry described above, two excitation frequencies 1 MHz and 915 MHz are used with a point source located at $\vec{r}'$ = 10 mm from the center of the geometry. A Gaussian shaped pulse of FWHM ~ 2 μs was used as microwave pulse function $\hat{P}(t)$ for the calculation of acoustic pressure. Total 28 acoustic receivers were evenly spaced along the convex boundary for capturing acoustic pressure originated from the object. The regularization parameter λ was determined according to [72]. The entire reconstruction algorithm was developed in MATLAB® and run on an Intel Xeon™ 3 GHz processor with a 3GB of internal memory. Total simulation had 40 iterations and each iteration took ~30 seconds.

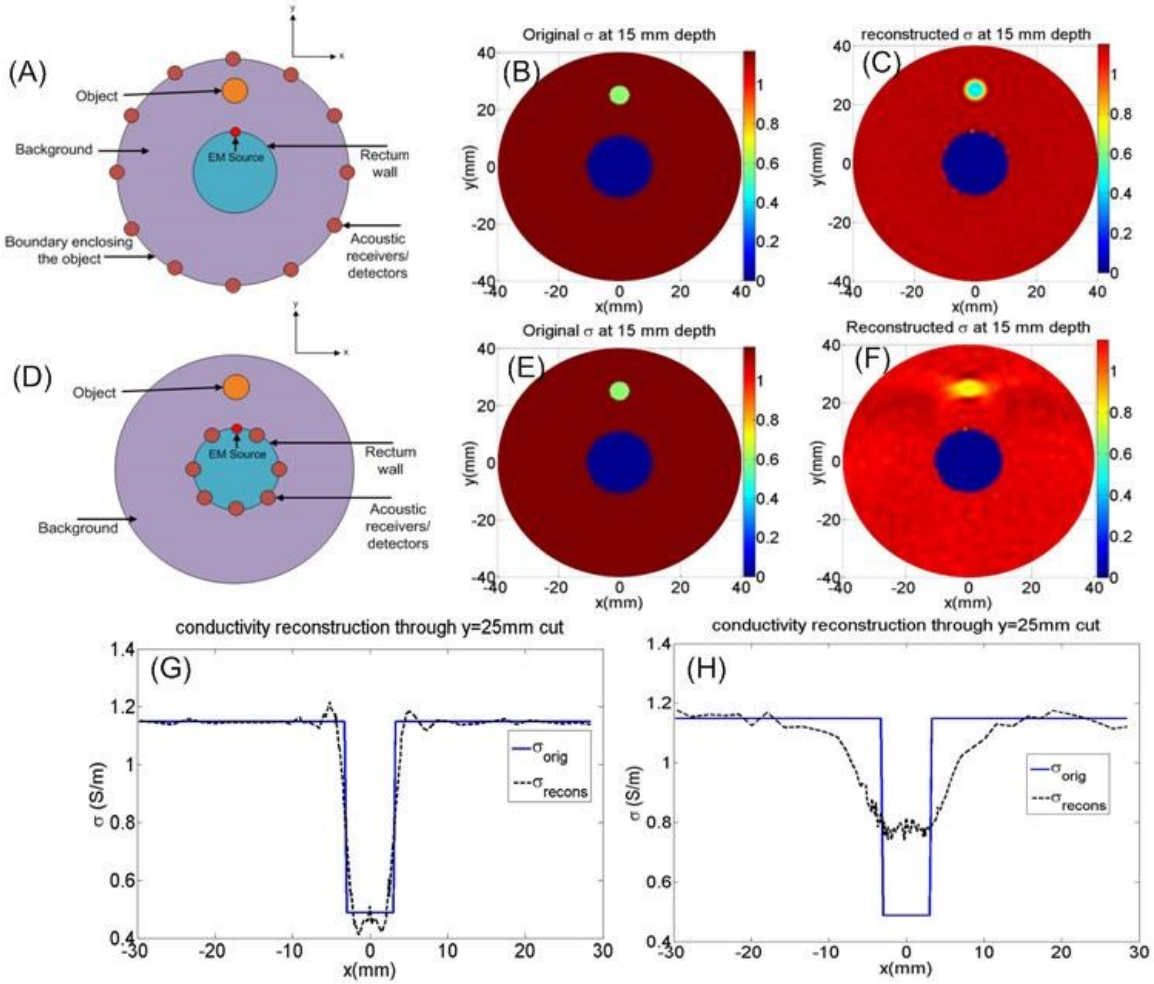

Figure-6.12 (A): Trans-rectal geometry with an EM source located on the rectal wall but the acoustic receivers moved from the rectal wall to a boundary that is enclosing the object and background. (B): Image of the true conductivity profile with an object at 15 mm depth. (C): Corresponding reconstructed image at 1 MHz. (D): Trans-rectal geometry with both the EM source and acoustic receivers located on the rectal wall. (E): Image of the true conductivity profile with an object at 15 mm depth. (F): Corresponding reconstructed image at 1 MHz. (G) Line plot of reconstructed conductivity profile for the reconstructed image C. (H): Line plot of reconstructed conductivity profile for the reconstructed image F.

6.9. Conclusion

Trans-rectal MI-TAT based image reconstruction algorithm for reconstructing the distribution of conductivity within a trans-rectal imaging geometry was presented. The algorithm was implemented using FEM and an absorbing boundary condition. Various simulation results were presented for both one and two tumor-mimicking objects at different depths with a 4:1 ratio of conductivity between the object and background. It was shown that the reconstruction algorithm

can recover the location of the objects at various depths. The quality of the reconstructed image and quantity of the reconstructed conductivity was object-depth dependent and objects closer to the acoustic receivers provided the most accurate reconstruction. The algorithm can readily be applied for multiple objects with different shapes and sizes and with a different dielectric contrast between the object and background. One potential application for this reconstruction algorithm is prostate cancer imaging. Future work related to the presented algorithm involves validating the algorithm with a prostate tissue-mimicking phantom using a trans-rectal EM applicator.

CHAPTER VII

CONCLUSIONS AND FUTURE DIRECTIONS

7.1. Contributions of this work

In this work, trans-rectal thermo-acoustic tomography (TAT) was explored for the first time for a potential application of prostate imaging. Since prostate tumor tissue exhibits different dielectric parameters from normal prostatic tissue, thermo-acoustic tomography has a potential to distinguish between prostate tumor and normal prostatic tissue as was shown by different reconstructed images in the previous chapter. The quality of the reconstructed images was shown to be object-depth dependent. However, it was shown in the reconstructed images that the proposed algorithm could detect the location of both single and multiple objects in a trans-rectal geometry.

This work also explored thermo-acoustic tomography for an external imaging geometry that has been explored by various research groups for a potential application of breast imaging. We have validated the algorithm with the reported data and expanded the algorithm to an internal or trans-rectal imaging geometry that has a different source-receiver configuration.

This work also calculated the E-field and the acoustic pressure that are generated inside the external and internal imaging geometry. The finite element method (FEM) was adopted as a numerical tool for solving the scalar wave equation and thermo-acoustic wave equation to

compute the E-field and acoustic pressure respectively. For the external imaging geometry, the numerically computed E-field was validated with the analytical solution for a single and concentric lossy dielectric as shown in figure 2.3 and 2.5 respectively. Both the FEM and analytical solutions were shown in figure 2.4 and 2.6 respectively. The analytical solutions were obtained for these two geometries using Eigen-function expansions [58, 59] as described in Appendix B. The acoustic pressure that was generated inside the external imaging geometry due to electromagnetic illumination was also computed using the finite element method. The object was considered to be the origin of the acoustic pressure wave. The calculated acoustic pressure was shown at four receivers located at four different locations. The propagation time of the acoustic wave to reach different receivers from a certain point of the object was also computed and compared with the calculated propagation time from the canter of the object. Various reconstructed images pertaining to external imaging geometry were also shown at 1 GHz in figure 4.2 and 4.4 for single and multiple objects respectively. The contrast of the reconstructed image was based on different conductivity profiles between the object and background. The conductivity of the object was considered to be higher than the background since the conductivity of breast tumor is usually higher than that of the normal breast tissues [33]. The percentage error between set and reconstructed conductivity was also computed.

The novelty of this work resided on application of thermo-acoustic tomography (TAT) based conductivity reconstruction algorithm to a trans-rectal or internal imaging geometry. This differs from the reconstruction algorithm that had applied for an external imaging geometry in two ways, 1. In external imaging geometry, an electromagnetic TM^z plane-wave that was impinging on the external boundary of the geometry was considered to be the illuminating EM source, while in trans-rectal or internal imaging geometry, an internally-applicable point electric current density that was located on the rectum wall or convex boundary was considered as the illuminating EM source. 2. In external imaging geometry, the detectors/receivers that captured the acoustic wave, were

located on the external boundary of the geometry and enclosed both the object and background to be imaged while in the trans-rectal geometry, detectors/receivers were located on the rectum wall/convex boundary that was located below object and hence was enclosed by the background. As was shown in the reconstructed images in previous chapter, the location of the receivers in a trans-rectal geometry limited the quality of the reconstructed image and objects closer to the receivers provided the most accurate reconstruction.

As for external imaging geometry and as a first step to the TAT based conductivity reconstruction algorithm, the E-field was computed for a trans-rectal geometry as well. The E-field was computed using the finite element method (FEM) by solving the scalar EM wave equation for a point electric current density. The numerically computed E-field was validated with the analytical solution obtained from homogeneous Green's function expansion [50] for a frequency of 915 MHz. For the validation, a homogeneous trans-rectal geometry as shown in figure 5.5 was considered. The acoustic pressure that was generated inside the geometry due to EM illumination was also computed and shown at three different receiver locations on the rectal wall. The calculated and actual propagation time of the acoustic wave to reach different receivers from the object was also shown.

The reconstructed images pertaining to the trans-rectal geometry were shown at 1 MHz and 915 MHz. It was discussed that at 1 MHz, the exact conductivity and permittivity profile of both the cancerous and normal ex-vivo human prostate were reported [68]. However, 1 MHz frequency was significantly lower than the usual operating frequency (typically starts from 434 MHz [8]) of microwave-induced thermo-acoustic tomography and the electrical dimension (in terms of wavelength) of the EM source (typically an antenna) would be significantly higher than the dimension of the rectum. As per our knowledge, 1 MHz is the highest frequency at which the conductivity and permittivity profile of both the cancerous and normal human prostate are reported. Although 915 MHz falls within the range of microwave frequencies that are used for thermo-

acoustic tomography, the conductivity and permittivity profile of only normal prostate (both human and rat) are reported at this frequency. However, by comparing the conductivity and permittivity profile of prostate at different frequencies, we have extrapolated the conductivity and permittivity profile of cancerous prostate at 915 MHz although these data demand experimental validation.

In this work, various reconstructed images pertaining to the trans-rectal geometry were shown with the objects of different sizes and at different depths. The percentage error between the true and reconstructed conductivity of the object was also computed. It was shown that the quality of the reconstructed images was object-depth dependent and objects closer to the acoustic receivers provided the most accurate reconstruction. The reconstructed images were shown at 1 and 915 MHz. At 1 MHz, the exact reported conductivity and permittivity profile of both the cancerous and normal ex-vivo human prostate [68] were used. At 915 MHz, exact conductivity and permittivity profile of normal human prostate [52] and extrapolated conductivity and permittivity profile of cancerous prostate were used. The percentage errors between the true and reconstructed conductivity for objects at different depths were also computed.

This work also showed the computation of the contrast-to-noise ratio (CNR) for the reconstructed images pertaining to trans-rectal geometry. The effect of the object radius on the reconstructed images was explored and object of 3 mm radius was shown to be the threshold radius than could be detected with an acceptable CNR and percentage error. The effect of various levels of Gaussian white noise on the reconstructed images was also explored. By comparing the reconstructed images for the objects of different depths and different radii and for different noise levels, a CNR of 2.0 was proposed as a threshold CNR for in-silico trans-rectal thermo-acoustic tomography.

7.2. Future Directions

7.2.1. Inhomogeneous dielectric constant

In this work, a homogeneity in dielectric constant or permittivity (ε_r) between the object and background for both external-imaging and internal-imaging geometry was considered i.e. the object and background was assumed to have the same dielectric constant. But because of highly inhomogeneous nature of the dielectric parameters of human tissues, the conductivity as well as the permittivity shows heterogeneity. Future work pertaining to the presented algorithm may include the heterogeneity in both ε_r and σ and reconstruct both. Reconstructing the dielectric constant or permittivity requires an additional computation of the "Jacobian" matrix specific to the dielectric constant (i.e. in addition to "Jacobian" specific to power loss density or conductivity that was calculated in this work). However, this requires the computation of the exact dielectric constant at microwave frequencies for a breast and prostate like geometry. Although a large set of dielectric constant profiles are available for human breast at different frequencies [33], the computation of the dielectric constant for a prostate like geometry at microwave frequencies still needs some attention.

7.2.2. Multi-region inhomogeneous trans-rectal geometry

This work assumes a homogeneous model for the background that was considered as normal tissues that include both the normal prostate and the surrounding tissues (e.g. bladder). However, a more realistic model would be to divide the background into normal prostate and the surrounding tissues. Both the normal prostate and the surrounding tissues can be represented by their respective dielectric constants and conductivities. Figure 7.1 shows an example of such model. The background is divided into normal prostate and the surrounding tissues. The surrounding tissues and the normal "walnut-shaped" prostate are represented by dielectric constants

$(\varepsilon_{r_1}, \varepsilon_{r_2})$ and conductivities (σ_1, σ_2) respectively. The prostate tumor is represented by its dielectric constant ε_{r_3} and conductivity σ_3. The length of the normal prostate can be considered as 40-50 mm while the length of the tumor can be from 1-20 mm, which is the threshold range of length of human prostate tumor for which a modest survival rate was reported [73]. The source and the acoustic receivers should be located on the rectal wall.

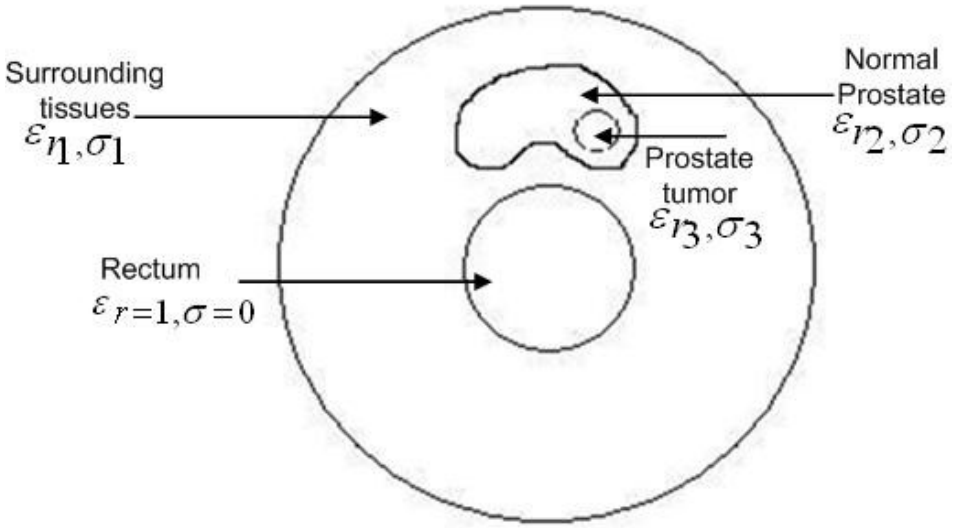

Figure-7.1: Inhomogeneous trans-rectal geometry with the background separated into a normal prostate and the surrounding tissues.

7.2.3. Experimental validation with a prostate tissue-mimicking phantom

The reconstruction algorithm for trans-rectal imaging geometry discussed previously subjects to an experimental validation with a prostate-tissue mimicking phantom. The specific aim is to develop an experimental system to study microwave-induced thermo-acoustic tomography (MI-TAT) in trans-rectal imaging geometry.

REFERENCES

1. D. A. Boas, “Imaging the Body with Diffuse Optical Tomography”, IEEE Signal Processing Mag. **18**, 57-75 (2001).
2. P. M. Meaney, K. D. Paulsen, and T. P. Ryan, “Two-dimensional hybrid element image reconstruction for TM illumination,” IEEE Trans. Ant. Propag. **43**, 239–247(1995).
3. A. E. Souvorov, A. E. Bulyshev, S. Y. Semenov, R. H. Svenson, A. G.Nazarov, Y. E. Sizov, and G. P. Tatsis, “Microwave tomography: A two-dimensional Newton iterative scheme,” IEEE Trans. Microwave Th. & Tech. **46** ,1654–1659(1998).
4. X. Wang, Y. Xu, M. Xu, S. Yokoo, E.S. Fry, L. V. Wang, “Photoacoustic tomography of biological tissues with high cross-section resolution: reconstruction and experiment,” Med Phys. **29**(12):2799-805 (2002).
5. R. A. Kruger, K. K. Kopecky, A. M. Aisen, D. R. Reinecke, G. A. Kruger and W. l. Kiser, “Thermoacoustic CT with radio waves: a medical imaging paradigm,” Radiology, **211,** 275-278 (1999).

6. B. W. Pogue., "Instrumentation and design of a frequency-domain diffuse optical tomography imager for breast cancer detection," Opt. Exp. **13**(1), 391-403(1997).
7. L. Yao, G. Guo, H. Jiang, "Quantitative microwave-induced thermoacoustic tomography," Med. Phys. **37**, 3752-3759 (2010).
8. R. A. Kruger, K. D. Miller, H. E. Reynolds, W. L. Kiser Jr, D. R. Reinecke, G. A. Kruger, "Breast cancer in vivo: contrast enhancement with thermoacoustic CT at 434 MHz-feasibility study," Radiology; **216**(1):279-83 (2000).
9. H. Jiang, K. D. Paulsen, U. L. Osterberg, B. W. Pogue, and M. S. Patterson,"Optical image reconstruction using frequency-domain data: Simulations and experiments," J. Opt. Soc. Am. A **13**, 253–266 (1996).
10. Jiang et al., "In vivo trans-rectal ultrasound-coupled optical tomography of a transmissible venereal tumor model in the canine pelvic canal," J. Biomed Opt, 2009. **14**(3): p. 030506.
11. D. Piao, K. E. Bartels, Z. Jiang, G. R. Holyoak, J. W. Ritchey, G. Xu , C. F. Bunting, G. Slobodov, "Alternative trans-rectal prostate imaging: A diffuse optical tomography method," IEEE Journal of Selected Topics in Quantum Electronics, **16(4)**: 715-729 (2010).
12. R. Siegel, D. Naishadham and A. Jemal, "Cancer Statistics," CA: Cancer J. Clin. **63** (1), 11-30 (2013).
13. http://radlink.com.sg/patient_mammography.aspx
14. http://www.riversideonline.com/health_reference/Womens-Health/PR00053.cfm
15. W. A. Kalender, " X-ray computed tomography," Phys. Med. Biol. **51**, R29-43 (2006)
16. S. C. Bushong , " Magnetic Resonance Imaging," C.V Mosby Co. (MO, USA), 1988.
17. http://www.prostatecentre.ca

18. W. Joines, R. Jirtle, M. Rafal, and D. Schaeffer, “Microwave power absorption differences between normal and malignant tissue,” Int. J. Radiat. Oncol. Biol. Phys. **6**, 681–687 (1980).
19. Y. Xu, L. V. Wang, “Rhesus monkey brain imaging through intact skull with thermoacoustic tomography,” IEEE Trans Ultrason Ferroelectr Freq Control.; **53**(3):542-8 (2006).
20. T. J. Polascik, J. E. Oesterling, and A. W. Partin, "Prostate specific antigen: a decade of discovery--what we have learned and where we are going," J. Urol. **162**, 293-306 (1999).
21. G. D. Grossfeld and P. R. Carroll, "Prostate cancer early detection: a clinical perspective," Epidemiol Rev. **23**, 173-80 (2001).
22. C. R. Porter, “Does the number of prostate biopsies performed affect the nature of the cancer identified?,” Nat. Clin. Pract. Urol. **4**, 132-133 (2007).
23. V. Scattoni, A. Zlotta, R. Montironi, C. Schulman, P. Rigatti, and F. Montorsi, “Extended and saturation prostatic biopsy in the diagnosis and characterisation of prostate cancer: a critical analysis of the literature,” Eur. Urol. **52**, 1309-1322 (2007)
24. A. G. Bell, Am. J. Sci. 20, 305 (1880).
25. T. Bowen, L. Nasoni, A. E. Pifer, and G. H. Sembrosk, “Some experimental results on the thermoacoustic imaging of soft tissue-equivalent phantoms,” Ultrason. Symp. Proc. **2**, 823–827(1981).
26. R. G. Olsen, ‘‘Generation of acoustic images from the absorption of pulsed microwave energy,’’ in *Acoustic Imaging*, edited by J. P. Powers (Plenum, New York, 1982), pp. 53–59.
27. R. G. Olsen and J. C. Lin, ‘‘Acoustic imaging of a model of a human hand using pulsed microwave irradiation,’’ Bio electro-magnetics (N.Y.) **4**, 397–400 (1983).

28. J. C. Lin and K. H. Chan, ‘‘Microwave thermo-elastic tissue imaging system design,’’ IEEE Trans. Microwave Theory and Tech. **32**, 854–860 (1984).

29. R. L. Nasoni, G. A. Evanoff, Jr., P. G. Halverson, and T. Bowen, ‘‘Thermoacoustic emission by deeply penetrating microwave radiation,’’ Proc.- IEEE Ultrason. Symp. **5**, 633–637 (1984).

30. K. H. Chan and J. C. Lin, ‘‘Microwave-induced thermoacoustic tissue imaging,’’ Proc. Engineering in Medicine and Biology Society 10th Annual International Conference, 445–446 (1988).

31. Ke et al., “Photoacoustic and thermoacoustic tomography for dog prostates”, Proc. SPIE , 789938 (2011).

32. Chaudhary et al., “Dielectric properties of normal & malignant human breast tissues at radiowave & microwave frequencies,” Indian J Biochem Biophys, 1984. **21**(1): p. 76-9.

33. Joines et al., “The measured electrical properties of normal and malignant human tissues from 50 to 900 MHz,” Med Phys, 1994. **21**(4): p. 547-50.

34. Surowiec, A.J., et al., “Dielectric properties of breast carcinoma and the surrounding tissues,” IEEE Trans Biomed Eng, 1988. **35**(4): p. 257-63.

35. Lazebnik et al., “A large-scale study of the ultrawideband microwave dielectric properties of normal, benign and malignant breast tissues obtained from cancer surgeries,” Phys. Med. Biol, 2007. **52**(20): p. 6093-6115.

36. Y. Xu, D. Feng and L. V. Wang, ‘‘Exact frequency-domain reconstruction for thermoacoustic tomography—I: Planar Geometry,’’ IEEE Trans. Med. Imaging **21**(7), 823–828 (2002).

37. Y. Xu, M. Xu and L. V. Wang, ‘‘Exact frequency-domain reconstruction for thermoacoustic tomography—II: Cylindrical Geometry,’’ IEEE Trans. Med. Imaging **21**(7), 829–833 (2002).

38. M. Xu and L. V. Wang, ‘‘Time-domain reconstruction for thermoacoustic tomography in a spherical Geometry,’’ IEEE Trans. Med. Imaging **21**(7), 814–822 (2002).
39. S. Mukherjee, C.F. Bunting, and D. Piao, “ Forward model of thermally-induced acoustic signal specific to intralumenal detection geometry,” Proc. SPIE, 789936 (2011).
40. Huang et al., “Quantitative thermo-acoustic tomography: Recovery of conductivity maps of heterogeneous media,” App. Phys. Lett, **101**, 244106 (2012).
41. S. Mukherjee, C.F. Bunting, and D. Piao, “Finite-element-method based reconstruction of heterogeneous conductivity distribution under point-illumination in trans-rectal imaging geometry for thermo-acoustic tomography,” in *BIOMED, OSA*. 2012, Miami, FL.
42. C. Zhang and Y. Wang , “A reconstruction algorithm for thermoacoustic tomography with compensation for acoustic speed heterogeneity,” Phys. Med. Biol. **53**, 4971-4982 (2008).
43. G. Zhu., et al., “Microwave-Induced Thermoacoustics: Assisting Microwave Tomography”. Magnetics, IEEE Transactions on, 2009. **45**(3): p. 1654-1657.
44. L. V. Wang, “Prospects of photoacoustic tomography,” Med Phys.; 35(12):5758-5767 (2008).
45. Andreev VG, Karabutov AA, Oraevsky AA, “Detection of ultrawide-band ultrasound pulses in optoacoustic tomography,” IEEE Trans Ultrason Ferroelectr Freq Control.; 50(10):1383-90 (2003).
46. X. Wang, Y.Pang, G.Ku, X. Xie, G. Stoica and LV Wang, “Noninvasive laser-induced photoacoustic tomography for structural and functional in vivo imaging of the brain”, Nat Biotechnol, **21**(7), 803-806 (2003).
47. Kolkman et al., “Photoacoustic imaging of blood vessels with a double-ring sensor featuring a narrow angular aperture,” J. Biomed. Opt, **9**(6), 1327-1335 (2004).
48. Wang et al., “Photoacoustic tomography: a potential new tool for prostate cancer,” Biomed Opt. Exp. , 1(4), 1117-1126 (2010).

49. H. Jiang, Z. Yuan and X. Gu, “Spatially varying optical and acoustic property reconstruction using finite element photoacoustic tomography,” J. Opt. Soc. Am. A, **23**(4), 2006.

50. A. Ishimaru, *Electromagnetic Wave Propagation, Radiation and Scattering* (Prentice Hall, Inc., New Jersey, 1991).

51. X. Song, B. W. Pogue, S. Jiang, M. M. Doyley, H. Dehghani, T. D. Tosteson and K. D. Paulsen, “ Automated region detection based on the contrast-to-noise ratio in near-infrared tomography,” Applied Optics, **43**(5), 1053-1062 (2004).

52. http://niremf.ifac.cnr.it/tissprop/htmlclie/htmlclie.htm#atsftag.

53. J. H. Richmond, "Scattering from a dielectric cylinder of arbitrary cross section shape." IEEE Trans. Antennas Propag., AP-13: 334-341(1965).

54. A. F. Peterson and S.V. Castillo, “A frequency-domain differential equation formulation for electromagnetic scattering from inhomogeneous cylinders,” IEEE Trans. Antennas Propag. 37, 601–607 (1989).

55. A. Bayliss and E. Turkel, “Radiation boundary conditions for wave-like equations,” Commun. Pure Appl. Math. 33, 707–725 (1980).

56. R. F. Harrington, *Time-Harmonic Electromagnetic Fields* (IEEE press, 2001).

57. A .F. Peterson, Scott L. Ray and Raj Mittra, *Computational Methods for Electromagnetics* (IEEE press, 1997).

58. C. A. Balanis, *Advanced Engineering Electromagnetics* (John Wiley & Sons, Inc. 1989).

59. J. Jing, *Theory and Computation of Electromagnetic Fields* (John Wiley & Sons, Inc. 2010).

60. P. Silvester, R. Ferrari, *Finite elements for electrical engineers,* 3rd ed. (Cambridge University Press, 1996).

61. J. Jing, *The finite element method in Electromagnetics*, 2nd ed. (John Wiley & Sons, Inc. 2002).

62. J. Volakis, A. Chatterjee and L. Kempel, *Finite Element Method for Electromagnetics* (IEEE Press, 1998).

63. L. V. Wang and H. Wu, *Biomedical Optics: Principles and Imaging* (Wiley Publishers, New Jersey, 2007).

64. K. Levenberg , "A Method for the Solution of Certain Non-Linear Problems in Least Squares," Quarterly of Applied Mathematics 2: 164–168(1944).

65. D. Marquardt, "An Algorithm for Least-Squares Estimation of Nonlinear Parameters," SIAM Journal on Applied Mathematics 11 (2): 431–441 (1963).

66. *http://men.webmd.com/picture-of-the-prostate.*

67. *http://www.washington.edu/news/2003/08/04/ultrasound-imaging-advance-improves-prostate-cancer-treatment/.*

68. R. J. Halter, A. Hartov, J. A. Heaney, K. D. Paulsen and A. R. Schned, "Electrical Impedance Spectroscopy of the Human Prostate," IEEE Trans. Biomed. Eng. **54**(7), 1321-1327 (2007).

69. H. Dehghani *et al*., "Near infrared optical tomography using NIRFAST: Algorithm for numerical model and image reconstruction," Commun. Numer. Meth. Eng. **25**, 711-732 (2008).

70. K. Wang and T. C. Zhu, "Reconstruction of in-vivo optical properties for human prostate using interstitial diffuse optical tomography," Opt. Exp. **17**(14), 11665-11672 (2009).

71. M. Abramowitz and I. A. Stegun, *Handbook of Mathematical Functions* (Dover, New York, 1965).

72. Q. Fang, "Computational Methods for Microwave Medical Imaging," Ph.D. dissertation, Dartmouth College, Dec. 2004.

73. R. Vollmer, “Tumor length in Prostate Cancer”, Am. J. Clin. Pathol. 130, 77-82 (2008).

APPENDICES

A. Analytical and numerical solution of surface and boundary integrals for a triangular element used in FEM [57, 60-62]

In chapter II, we have the following form of surface integrals

$$I_{mn} = \iint_{\Gamma} \nabla \psi_m(x,y) \bullet \nabla \psi_n(x,y) dxdy \qquad \text{(A.1)}$$

$$B_{mn} = \iint_{\Gamma} \psi_m(x,y) \psi_n(x,y) dxdy \qquad \text{(A.2)}$$

where $\psi(x,y)$ is a linear basis function.

Both equations (A.1) and (A.2) can be solved analytically for each triangular element as shown in figure A.1 and the solution is

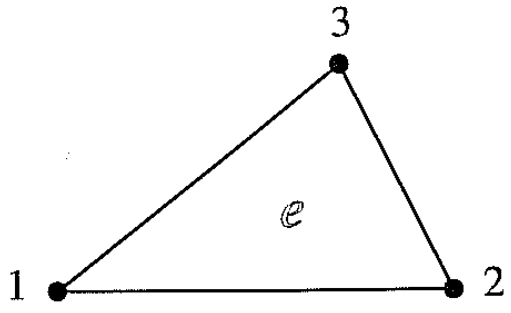

Figure A.1 A linear triangular element

$$I_{mn} = \frac{1}{4\Delta^e}(b_m^e b_n^e + c_m^e c_n^e) \tag{A.3}$$

$$B_{mn} = \frac{\Delta^e}{12}(1 + \delta_{mn}) \tag{A.4}$$

$m, n = 1,2,3$

Where

$$\Delta^e = \frac{1}{2}\begin{vmatrix} 1 & x_1 & y_1 \\ 1 & x_2 & y_2 \\ 1 & x_3 & y_3 \end{vmatrix}$$

=area of each element (A.5)

$$b_1^e = y_2 - y_3 \qquad c_1^e = x_3 - x_2$$

$$b_2^e = y_3 - y_1 \qquad c_2^e = x_1 - x_3$$

$$b_3^e = y_1 - y_2 \qquad c_3^e = x_2 - x_1 \tag{A.6}$$

δ_{mn} is the Kronecker delta function and is defined by

$$\left.\begin{aligned} \delta_{mn} &= 1 \\ \delta_{mn} &= 0 \end{aligned}\right\} \begin{aligned} m &= n \\ m &\neq n \end{aligned} \tag{A.7}$$

and (x_1, y_1), (x_2, y_2) and (x_3, y_3) are the (x, y) co-ordinates of node 1, 2 and 3 of triangular element of figure A.1 respectively.

In Chapter II, We also have three boundary integrals of following form

$$b_{mn} = \int_{\partial\Gamma} \psi_m(\phi)\psi_n(\phi)\rho d\phi \tag{A.8}$$

$$c_{mn} = \int_{\partial\Gamma} \frac{\partial\psi_m(\phi)}{\partial\phi}\frac{\partial\psi_n(\phi)}{\partial\phi}\rho d\phi \tag{A.9}$$

$$d_m = \int_{d\Gamma} \psi_m\left(\frac{\partial E_z^{inc}}{\partial\rho} - \alpha E_z^{inc} - \beta\frac{\partial^2 E_z^{inc}}{\partial\phi^2}\right)\rho d\phi \tag{A.10}$$

Integrals A.8 and A.9 can be solved analytically and the solution is

$$b_{mn} = \begin{cases} \frac{1}{3}w & m = n \\ \frac{1}{6}w & otherwise \end{cases} \tag{A.11}$$

$$c_{mn} = \begin{cases} \frac{1}{w} & m = n \\ -\frac{1}{w} & otherwise \end{cases} \tag{A.12}$$

where w is the length of each boundary segments and is given by

$$w = \phi_2 - \phi_1 \tag{A.13}$$

ϕ_1 and $\phi 2$ is the ϕ coordinate of boundary nodes 1 and 2 respectively.

For $E_z^{inc} = e^{-jk[x\cos\theta + y\sin\theta]} = e^{-jk\rho\cos(\theta-\phi)}$, d_m can be simplified as

$$d_m = \int_{\partial\Gamma} -\psi_m[(\alpha + (1+\beta\rho)jk\cos(\theta-\phi) - \beta k^2\rho^2\sin^2(\theta-\phi)]e^{-jk\rho\cos(\theta-\phi)}\rho d\phi \tag{A.14}$$

With θ is the angle of incidence of any plane wave.

Integral of equation (A.14) can be solved numerically using Gauss quadrature [71].

B. Analytical solution of EM wave Scattering by a circular dielectric cylinder [56-58]

B.1. Analytical solution of Plane wave scattering by a lossless dielectric cylinder

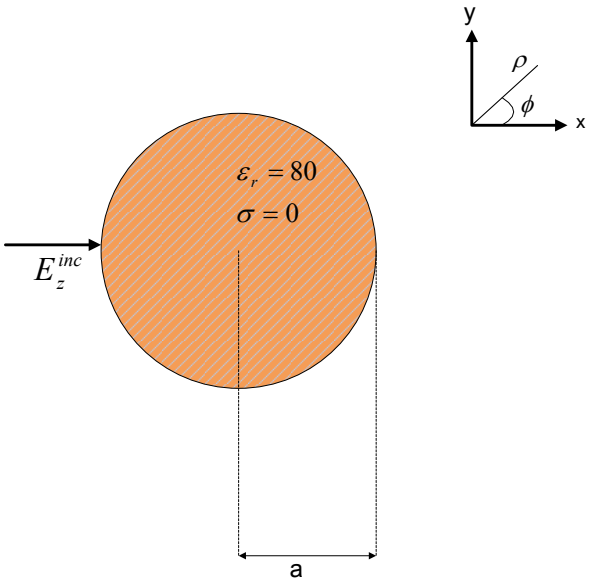

Figure B.1. Plane wave scattering by a lossless dielectric cylinder

Figure B.1 shows a TM^Z plane wave impinging on the boundary of a lossless dielectric of radius a. Since the incident wave is propagating in + x direction, incident E-field can be expressed as

$$E_z^{inc} = E_0 e^{-jk_0 x} \qquad \text{(B.1)}$$

In equation (B.1), E_0 is the amplitude of incident E-field k_0 is the propagation constant in free space and can be written as $k_0 = \omega\sqrt{\mu_0 \varepsilon_0}$

With

ω = angular frequency (Radian/sec)

μ_0 = free space permeability = $4\pi \times 10^{-7}$ (Henry/m)

ε_0 =free space permittivity = 8.8419×10^{-12} (Farad/m)

If we perform cylindrical harmonic expansion [56-58] to incident E-field, it can be expressed as

$$E_z^{inc} = E_0 \sum_{n=-\infty}^{\infty} j^{-n} J_n(k_0 \rho) e^{jn\phi} \tag{B.2}$$

Where J_n is the Bessel function of 1st kind.

Scattered E-field and total E-field inside the dielectric can be expanded in a similar fashion as

$$E_z^s = E_0 \sum_{n=-\infty}^{\infty} a_n H_n^{(2)}(k_0 \rho) e^{jn\phi} \qquad \rho > a \tag{B.3}$$

$$E_z^{tot} = E_0 \sum_{n=-\infty}^{\infty} b_n J_n(k_d \rho) e^{jn\phi} \qquad \rho < a \tag{B.4}$$

In equations (B.3)-(B.4), a_n and b_n is the coefficient that needs to be determined, $H_n^{(2)}()$ is the Hankel function of 2nd kind and k_d is the propagation constant in the dielectric and can be written as

$$k_d = k_0 \sqrt{\varepsilon_r} \tag{B.5}$$

with ε_r is the permittivity of the dielectric.

Since magnetic field H_ϕ is related to E_z as $H_\phi = \frac{1}{j\omega\mu}\frac{\partial E_z}{\partial \rho}$, incident , scattered and total magnetic field (inside the dielectric) can be written as

$$H_\phi^{inc} = \frac{E_0}{j\eta_0}\sum_{n=-\infty}^{\infty} j^{-n} J_n^{'}(k_0\rho)e^{jn\phi} \tag{B.6}$$

$$H_\phi^{s} = \frac{E_0}{j\eta_0}\sum_{n=-\infty}^{\infty} a_n H_n^{(2)'}(k_0\rho)e^{jn\phi} \qquad \rho > a \tag{B.7}$$

$$H_\phi^{tot} = \frac{E_0}{j\eta_d}\sum_{n=-\infty}^{\infty} b_n J_n^{'}(k_d\rho)e^{jn\phi} \qquad \rho < a \tag{B.8}$$

where,

η_0 is the intrinsic impedance of free space and can be written as $\eta_0 = \sqrt{\frac{\mu_0}{\varepsilon_0}}$ (~ 377 ohms).

η_d is the intrinsic impedance of dielectric and can be written as $\eta_d = \sqrt{\frac{\mu_0\mu_r}{\varepsilon_0\varepsilon_r}}$, where μ_r and ε_r is the relative permeability (is taken as 1 in our solution) and permittivity of the dielectric respectively

and $' = \frac{\partial}{\partial(k\rho)}$.

Derivative of Bessel and Hankel function in equations (B.6)-(B.8) can be computed using the relationship [58]

$$\frac{d}{dx}(Z_n(x)) = -Z_{n+1}(x) + \frac{n}{x}Z_n(x) \tag{B.9}$$

where Z can be Bessel or Hankel function.

Applying boundary conditions

$$E_z^{inc} + E_z^s = E_z^{tot} \qquad \text{at } \rho = a \tag{B.10}$$

$$H_\phi^{inc} + H_\phi^s = H_\phi^{tot} \qquad \text{at } \rho = a \tag{B.11}$$

a_n and b_n can be computed as

$$a_n = j^{-n} \frac{\eta_0 J_n'(k_d a) J_n(k_0 a) - \eta_d J_n'(k_0 a) J_n(k_d a)}{n_d J_n(k_d a) H_n^{(2)'}(k_0 a) - \eta_0 J_n'(k_d a) H_n^{(2)}(k_0 a)} \tag{B.12}$$

$$b_n = j^{-n} \eta_d \frac{J_n(k_0 a) H_n^{(2)}{}'(k_0 a) - J_n'(k_0 a) H_n^{(2)}(k_0 a)}{n_d J_n(k_d a) H_n^{(2)'}(k_0 a) - \eta_0 J_n'(k_d a) H_n^{(2)}(k_0 a)} \tag{B.13}$$

Equation (B.4) along with (B.13) can be solved to compute total E-field inside the dielectric.

B.2. Analytical solution of Plane wave scattering by a lossy dielectric cylinder

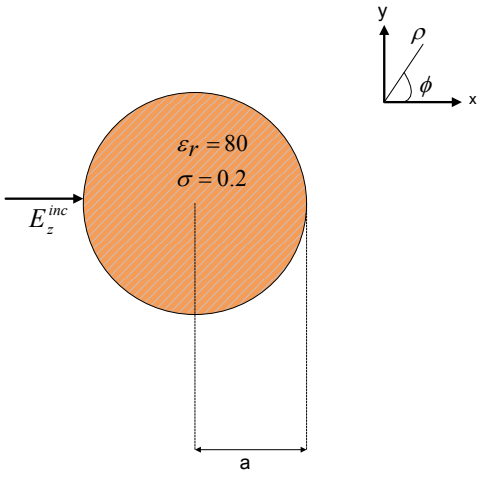

Figure B.2. Plane wave scattering by a lossy dielectric cylinder

Figure B.2 shows a TM^Z plane wave impinging on the boundary of a lossy dielectric of radius a. Analytical solution of total E-field inside a lossy dielectric follows the same procedure as of a lossless dielectric and equations (B.1) –(B.13) is valid for a lossy dielectric also.

The only change is the real permittivity (ε_r) of dielectric which should replaced by a complex permittivity for a lossy dielectric as

$$\varepsilon_c = \varepsilon_r - j\frac{\sigma}{\omega\varepsilon_0} \tag{B.14}$$

where σ is the finite conductivity of a lossy dielectric.

B.3. Analytical solution of Plane wave scattering by a lossy two-layered dielectric cylinder

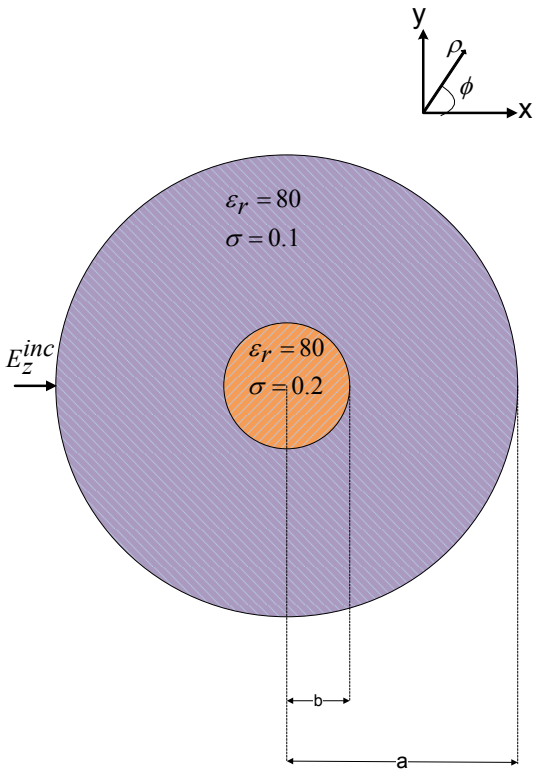

Figure B.3. Plane wave scattering by a two-layered lossy dielectric cylinder

Figure B.3 shows a two-layered lossy dielectric cylinder. Inner and outer dielectric has a radius of b and a respectively. One TM^z plane wave is impinging on the boundary of the outer dielectric. As for a single lossless and lossy dielectric, incident E and H-field for a two-layered dielectric can be written as

$$E_z^{inc} = E_0 e^{-jk_0 x} = E_0 \sum_{n=-\infty}^{\infty} j^{-n} J_n(k_0\rho) e^{jn\phi} \tag{B.15}$$

$$H_\phi^{inc} = \frac{E_0}{j\eta_0} \sum_{n=-\infty}^{\infty} j^{-n} J_n'(k_0\rho) e^{jn\phi} \tag{B.16}$$

Scattered E and H-field outside the outer dielectric and total E and H field inside the outer dielectric can be expressed as

$$E_{zo}^s = E_0 \sum_{n=-\infty}^{\infty} a_n H_n^{(2)}(k_0\rho) e^{jn\phi} \qquad \rho > a \tag{B.17}$$

$$H_{\phi o}^s = \frac{E_0}{j\eta_0} \sum_{n=-\infty}^{\infty} a_n H_n^{(2)'}(k_0\rho) e^{jn\phi} \qquad \rho > a \tag{B.18}$$

$$E_{zo}^{tot} = E_0 \sum_{n=-\infty}^{\infty} b_n J_n(k_{do}\rho) e^{jn\phi} \qquad \rho < a \tag{B.19}$$

$$H_{\phi o}^{tot} = \frac{E_0}{j\eta_{do}} \sum_{n=-\infty}^{\infty} b_n J_n'(k_{d0}\rho) e^{jn\phi} \qquad \rho < a \tag{B.20}$$

where a_n and b_n is given by (B.12) and (B.13) respectively.

Total E-field inside the inner dielectric can be written as

$$E_{zi}^{tot} = E_0 \sum_{n=-\infty}^{\infty} c_n J_n(k_{di}\rho) e^{jn\phi} \qquad 0 < \rho < b \tag{B.21}$$

Applying boundary condition,

$$E_{zo}^{tot} = E_{zi}^{tot} \text{ at } \rho = b \tag{B.22}$$

c_n can be found as,

$$c_n = b_n \frac{J_n(k_{do}b)}{J_n(k_{di}b)} \tag{B.23}$$

In equations (B.19)-(B.21),

$$k_{do} = k_0 \sqrt{\varepsilon_{co}} \tag{B.24}$$

$$k_{di} = k_0 \sqrt{\varepsilon_{ci}} \tag{B.25}$$

$$\eta_{do} = \frac{\eta_0}{\sqrt{\varepsilon_{co}}} \tag{B.26}$$

Where ε_{co} and ε_{ci} is the complex permittivity of outer and inner dielectric respectively and can be written individually as

$$\varepsilon_{co} = \varepsilon_r - j\frac{\sigma_o}{\omega\varepsilon_0} \tag{B.27}$$

$$\varepsilon_{ci} = \varepsilon_r - j\frac{\sigma_i}{\omega\varepsilon_0} \tag{B.28}$$

Where σ_o and σ_i is the finite conductivity of outer and inner dielectric respectively. Equations (B.19) and (B.21) can be solved to find the total E-field inside outer and inner dielectric respectively.

C. MATLAB® codes used for the simulation

C.1. MATLAB® code for solving the E-field in an external imaging geometry with a single target

```
% Calculating TM wave electric field
% for an external imaging geometry with a single target

%Bayliss-Turkel RBC is considered here

% Author : Sovanlal Mukherjee, April,2011

%Ref : A. F. Peterson and S. V. Castillo, "A frequency-domain differential equation
% formulation for electromagnetic scattering from inhomogeneous cylinders,"
% IEEE Trans. Antennas Propag. 37, 601–607 (1989).

function [E_z_abs nn sigma_0]=E_field_exact(FEM_node_coord,...
   conn_array_FEM,conn_array_bnd_new,lamda,...
                    eps_r,mu_r,sigma_bg,...
                    sigma_target,W,c,eps_0,center_target,...
                    center_bg,rad_target,rad_bg,theta,a);
 %% FEM algorithm

n_elem = size(conn_array_FEM,1);    %total number of elements
n_node = size(FEM_node_coord,1);    %total number of nodes

n_bnd_elem=size(conn_array_bnd_new,1); % total number of boundary elements

% initialize FEM matrices
AA = zeros(n_node,n_node);
I1 = zeros(n_node,n_node);
I2= zeros(n_node,n_node);
b= zeros(n_node,1);

kk=0;
MM=0;
NN=0;
sigma_0= sigma_bg*ones(n_node,1);

% FEM algorithm
for elem = 1:n_elem

   %reading 3 local nodes of each element
   n1 = conn_array_FEM(elem,1);
   n2 = conn_array_FEM(elem,2);
   n3 = conn_array_FEM(elem,3);

% x, y coordinates of 3 local nodes
x1=FEM_node_coord(n1,1);
y1=FEM_node_coord(n1,2);

x2=FEM_node_coord(n2,1);
y2=FEM_node_coord(n2,2);
```

```
x3=FEM_node_coord(n3,1);
y3=FEM_node_coord(n3,2);

C_x= (x1+x2+x3)/3;
C_y= (y1+y2+y3)/3;      % centroid of each element

p_T = sqrt((C_x-center_bg)^2+(C_y)^2); %radius of the background

p_T1= sqrt((C_x-center_target)^2+(C_y)^2); % radius of the target

if p_T1<rad_target
% complex wave number inside the target
k= ((W/c)*sqrt(eps_r-j*sigma_target/(W*eps_0)));
n_target(MM+1,:)=[n1 n2 n3];
MM=MM+1;    % this implies the no. of elements inside the target
end

if p_T<rad_bg &&p_T1>rad_target
n11=n1;
%complex wave number outside the target
k= ((W/c)*sqrt(eps_r-j*sigma_bg/(W*eps_0)));                    kk=kk+1;
end

%calculating coeffs of basis function
   b1= y2-y3;
   b2= y3-y1;
   b3= y1-y2;

   c1= x3-x2;
   c2= x1-x3;
   c3= x2-x1;
% area of the triangular element

   delta= 0.5*abs(b1*c2-b2*c1);

% FEM matrices

  A1 = (1/mu_r)*(1/(4*delta))*[b1^2+c1^2   b1*b2+c1*c2 b1*b3+c1*c3;...
                        b2*b1+c2*c1 b2^2+c2^2   b2*b3+c2*c3;...
                        b3*b1+c3*c1 b3*b2+c3*c2 b3^2+c3^2];


   A2 = ((k.^2)*delta/12)*[2 1 1;1 2 1;1 1 2];

   A11 = A1-A2;



% assembling the matrix
```

```
    AA(n1,n1) = AA(n1,n1)+A11(1,1);
    AA(n1,n2) = AA(n1,n2)+A11(1,2);
    AA(n1,n3) = AA(n1,n3)+A11(1,3);

    AA(n2,n1) = AA(n2,n1)+A11(2,1);
    AA(n2,n2) = AA(n2,n2)+A11(2,2);
    AA(n2,n3) = AA(n2,n3)+A11(2,3);

    AA(n3,n1) = AA(n3,n1)+A11(3,1);
    AA(n3,n2) = AA(n3,n2)+A11(3,2);
    AA(n3,n3) = AA(n3,n3)+A11(3,3);


end
    AA;

    %% solving the boundary integral

    % calculating the coeffs of Bayliss-Turkel RBC

    k_bnd= ((W/c)*sqrt(eps_r-j*sigma_bg/(W*eps_0)));

    alpha_num = -j*k_bnd-(3/(2*a))+(j*3/(8*k_bnd*a^2));
    alpha_den = 1-(j/(k_bnd*a));

    alpha = alpha_num/alpha_den;

    beta_num=-(j/(2*k_bnd*a^2));
    beta_den = 1-(j/(k_bnd*a));

    beta =beta_num/beta_den;


    for mm= 1:n_bnd_elem

    % 2 nodes of each boundary element
    n1_bnd = conn_array_bnd_new(mm,1);
    n2_bnd = conn_array_bnd_new(mm,2);

    % x,y coords of each boundary nodes
    x1_bnd=FEM_node_coord(n1_bnd,1);
    y1_bnd=FEM_node_coord(n1_bnd,2);

    x2_bnd=FEM_node_coord(n2_bnd,1);
    y2_bnd=FEM_node_coord(n2_bnd,2);

    % phase angle of each boundary nodes

    phi1 = angle(x1_bnd+1j*y1_bnd);

    phi2 = angle(x2_bnd+1j*y2_bnd);
```

```
% making sure 0<=phi<=2*pi
 if phi1<0

   phi1=2*pi-abs(phi1);

 end

 if phi2<0

   phi2=2*pi-abs(phi2);

 end

 % Orientation of phi (anti-clockwise, increasing order)
 if phi2==0 && phi1>3*pi/2
 phi2= 2*pi;
 end
 if phi2~=0 || (phi2==0 && phi1<pi/2)
 Phi=[phi1,phi2];
 Phi_sort= sort(Phi);
 phi1=Phi_sort(1);
 phi2= Phi_sort(2);
 end
 if phi1==0 && phi2>3*pi/2

    phi1=phi2;
    phi2=2*pi;
 end

 w =(phi2-phi1);

% FEM matrices on boundary
A_pq_3 =alpha*a*w*[1/3 1/6;1/6 1/3];

A_pq_4 =beta*a*(1/w)*[1 -1;-1 1];

A_pq = A_pq_3-A_pq_4;

% assembly of boundary matrix

I1(n1_bnd,n1_bnd) =I1(n1_bnd,n1_bnd)+A_pq(1,1);
I1(n1_bnd,n2_bnd) =I1(n1_bnd,n2_bnd)+A_pq(1,2);
I1(n2_bnd,n1_bnd) =I1(n2_bnd,n1_bnd)+A_pq(2,1);
I1(n2_bnd,n2_bnd) =I1(n2_bnd,n2_bnd)+A_pq(2,2);

% calculating source terms

b1= source_term_test1(phi1,phi2,k_bnd,theta,beta,alpha,a);
b2=source_term_test2(phi1,phi2,k_bnd,theta,beta,alpha,a);
% assembly of source matrix
b(n1_bnd)=b(n1_bnd)+b1;
b(n2_bnd)=b(n2_bnd)+b2;
end
```

```
%% Calculating E Field
   E_z = (AA-I1)\b;     %total electric field

   E_z_abs = abs(E_z);  %magnitude of electric field

   nn= unique(n_target);
   sigma_0(nn) =sigma_target;   % exact conductivity of the target
```

Subroutine source_term_test1

```
function b = source_term_test1(phi1,phi2,k,theta,beta,alpha,a)
b1= quadgk(@(phi)source1_test(phi,phi1,phi2,k,theta,beta,alpha,a),phi1,phi2);

b = b1;
```

Subroutine source1_test

```
function b =source1_test(phi,phi1,phi2,k,theta,beta,alpha,a);

Bm1= (phi2-phi)/(phi2-phi1);
term = (alpha+(beta*a+1)*j*k*cos(theta-phi)-...
      beta*k^2*a^2*((sin(theta-phi)).^2)).*exp(-j*k*a*cos(theta-phi));

b = -a*Bm1.*term;
```

Subroutine source_term_test2

```
function b = source_term_test2(phi1,phi2,k,theta,beta,alpha,a)

b1= quadgk(@(phi)source2_test(phi,phi1,phi2,k,theta,beta,alpha,a),phi1,phi2);

b = b1;
```

Subroutine source2_test

```
function b =source2_test(phi,phi1,phi2,k,theta,beta,alpha,a);
Bm2 = (phi-phi1)/(phi2-phi1);


term = (alpha+(beta*a+1)*j*k*cos(theta-phi)-...
      beta*k^2*a^2*((sin(theta-phi)).^2)).*exp(-j*k*a*cos(theta-phi));

b = -a*Bm2.*term;
```

C.2. MATLAB® code for solving acoustic pressure in an external imaging geometry with a single target

```
function [K M C B dB_ds P_exact P_exact_plot P_exact_Rx] =TAT_FEM_external_geom...
   (FEM_node_coord,conn_array_FEM,conn_array_bnd_new,vs,C_p, beta,...
   s_0,node,rx_points,a,alpha,del,T1,d_t,sigma_2);
```

```
%% finite element model to find the pressure

n_elem= size(conn_array_FEM,1);   %total number of elements

K1 = zeros(node,node);
K2 = zeros(node,node);


C_0 = zeros(node,node);

M= zeros(node,node);

B= zeros(node,1);
dB_ds= zeros(node,node);

r_bnd=a;


n_bnd_elem= size(conn_array_bnd_new,1);

for elem = 1:n_elem

   %reading 3 local nodes of each element
   n1 = conn_array_FEM(elem,1);
   n2 = conn_array_FEM(elem,2);
   n3 = conn_array_FEM(elem,3);

   % x, y coordinates of 3 local nodes

   x1=FEM_node_coord(n1,1);
   y1=FEM_node_coord(n1,2);

   x2=FEM_node_coord(n2,1);
   y2=FEM_node_coord(n2,2);

   x3=FEM_node_coord(n3,1);
   y3=FEM_node_coord(n3,2);

   b1= y2-y3;
   b2= y3-y1;
   b3= y1-y2;

   c1= x3-x2;
   c2= x1-x3;
   c3= x2-x1;

   % area of the triangular element

   delta= 0.5*abs(b1*c2-b2*c1);
```

```
% calculating individual surface matrices

kk= (1/(4*delta))*[b1^2+c1^2   b1*b2+c1*c2 b1*b3+c1*c3;...
                  b2*b1+c2*c1 b2^2+c2^2   b2*b3+c2*c3;...
                  b3*b1+c3*c1 b3*b2+c3*c2 b3^2+c3^2];

mm= (1/(vs^2))*(delta/12)*[2 1 1;1 2 1;1 1 2];


b_0_k1= (beta*delta/C_p)*(1/12)*s_0(n1)*...
[2 1 1];

b_0_k2= (beta*delta/C_p)*(1/12)*s_0(n2)*...
[1 2 1];

b_0_k3= (beta*delta/C_p)*(1/12)*s_0(n3)*...
[1 1 2];

b_0=sum([b_0_k1;b_0_k2;b_0_k3],2);


b1_ds=(beta/C_p)*(delta/12)*[2 1 1;...
                             1 2 1;...
                             1 1 2];


% assembling the matrices
% K matrix
K1(n1,n1) = K1(n1,n1)+kk(1,1);
K1(n1,n2) = K1(n1,n2)+kk(1,2);
K1(n1,n3) = K1(n1,n3)+kk(1,3);

K1(n2,n1) = K1(n2,n1)+kk(2,1);
K1(n2,n2) = K1(n2,n2)+kk(2,2);
K1(n2,n3) = K1(n2,n3)+kk(2,3);

K1(n3,n1) = K1(n3,n1)+kk(3,1);
K1(n3,n2) = K1(n3,n2)+kk(3,2);
K1(n3,n3) = K1(n3,n3)+kk(3,3);

% M matrix
M(n1,n1) = M(n1,n1)+mm(1,1);
M(n1,n2) = M(n1,n2)+mm(1,2);
M(n1,n3) = M(n1,n3)+mm(1,3);

M(n2,n1) = M(n2,n1)+mm(2,1);
M(n2,n2) = M(n2,n2)+mm(2,2);
M(n2,n3) = M(n2,n3)+mm(2,3);

M(n3,n1) = M(n3,n1)+mm(3,1);
M(n3,n2) = M(n3,n2)+mm(3,2);
M(n3,n3) = M(n3,n3)+mm(3,3);
```

```
    % dB_ds matrix
    dB_ds(n1,n1) = dB_ds(n1,n1)+b1_ds(1,1);
    dB_ds(n1,n2) = dB_ds(n1,n2)+b1_ds(1,2);
    dB_ds(n1,n3) = dB_ds(n1,n3)+b1_ds(1,3);

    dB_ds(n2,n1) = dB_ds(n2,n1)+b1_ds(2,1);
    dB_ds(n2,n2) = dB_ds(n2,n2)+b1_ds(2,2);
    dB_ds(n2,n3) = dB_ds(n2,n3)+b1_ds(2,3);

    dB_ds(n3,n1) = dB_ds(n3,n1)+b1_ds(3,1);
    dB_ds(n3,n2) = dB_ds(n3,n2)+b1_ds(3,2);
    dB_ds(n3,n3) = dB_ds(n3,n3)+b1_ds(3,3);

    % B matrix

    B(n1)=B(n1)+b_0(1);
    B(n2)=B(n2)+b_0(2);
    B(n3)=B(n3)+b_0(3);

end

for jj= 1:n_bnd_elem

    % 2 nodes of each boundary element
    n1_bnd = conn_array_bnd_new(jj,1);
    n2_bnd = conn_array_bnd_new(jj,2);

    % x,y coords of each boundary nodes
    x1_bnd=FEM_node_coord(n1_bnd,1);
    y1_bnd=FEM_node_coord(n1_bnd,2);

    x2_bnd=FEM_node_coord(n2_bnd,1);
    y2_bnd=FEM_node_coord(n2_bnd,2);

    %length of each boundary element
    ls = sqrt((x1_bnd-x2_bnd)^2+(y1_bnd-y2_bnd)^2);

    %boundary matrices
    k2= (ls/6)*(1/(2*r_bnd))*[2 1; 1 2];
    C1= (1/vs)*(ls/6)*[2 1; 1 2];

    % assembling the boundary matrices
    K2(n1_bnd,n1_bnd)= K2(n1_bnd,n1_bnd)+k2(1,1);
    K2(n1_bnd,n2_bnd)= K2(n1_bnd,n2_bnd)+k2(1,2);
    K2(n2_bnd,n1_bnd)= K2(n2_bnd,n1_bnd)+k2(2,1);
    K2(n2_bnd,n2_bnd)= K2(n2_bnd,n2_bnd)+k2(2,2);

    C_0(n1_bnd,n1_bnd)= C_0(n1_bnd,n1_bnd)+C1(1,1);
    C_0(n1_bnd,n2_bnd)= C_0(n1_bnd,n2_bnd)+C1(1,2);
    C_0(n2_bnd,n1_bnd)= C_0(n2_bnd,n1_bnd)+C1(2,1);
    C_0(n2_bnd,n2_bnd)= C_0(n2_bnd,n2_bnd)+C1(2,2);
```

```
end


K=K1+K2;
C=C_0;

%% calculating pressure in time-domain

 p_t_e= zeros(node,1);
 p_d_t_e = zeros(node,1);
 p_d_d_t_e= zeros(node,1);


 P_exact=[];
 P_exact_plot=[];
 P_exact_Rx=[];


for t=0:d_t:T1

S_t= exp((-(t-T1/4)^2)/(2*sigma_2));  % Gaussian source
S_d_t= -1e6*S_t*(t-(T1/4))/sigma_2;   % differentiated Gaussian source


    dt=d_t*1e-6;  % time step in second

% calculate acoustic pressure based on % original conductivity profile
 [p_t_exact p_d_t_exact p_d_d_t_exact]= pressure_exact...
 (B,K,M,C,del,alpha,dt,S_t,S_d_t,p_t_e,p_d_t_e,p_d_d_t_e);

 p_t_e= p_t_exact;     % update p at t with that value at t+dt
 p_d_t_e=p_d_t_exact;  % update dp/dt at t with that value at t+dt
 p_d_d_t_e=p_d_d_t_exact;% update d2p/dt2 at t with that value at t+dt


 p_exact=p_t_exact(rx_points);%capturing acoustic pressure at receiver points

 p_exact_plot= p_t_exact;     %capturing all acoustic pressure

P_exact=[P_exact;p_exact]; %accumulating received pressure at different time
P_exact_plot=[P_exact_plot p_exact_plot]; %accumulating all pressure at different time %matrix with a
size of [no. of receiver x total time span]
%can be used for plotting the pressure at a particular receiver
%versus time

P_exact_Rx= [P_exact_Rx p_exact];
 end
```

Subroutine pressure_exact

```
% this code calculates the acoustic pressure based on
```

```
% original conductivity profile

function [p_e,p_d_t,p_d_d_t]= pressure_exact...
   (B_0,K,M,C,del,alpha,dt,S_t,S_d_t,p_t,p_d_t,p_d_d_t);

m1= K+(1/(alpha*dt*dt))*M+(del/(alpha*dt))*C;

m2=(1/(alpha*dt*dt))*p_t+(1/(alpha*dt))*p_d_t+((1/(2*alpha))-1)*...
       p_d_d_t;

m3= (del/(alpha*dt))*p_t+((del/alpha)-1)*p_d_t+((del/(2*alpha))-1)...
        *dt*p_d_d_t;


%% --Newmark's time stepping algorithm-------------------------------------

B_t_dt= B_0*2*S_t*S_d_t;       %B at t+dt


p_t_dt = m1\(B_t_dt+M*m2+C*m3);   % p at t+dt

% d2p/dt2 at t+dt
p_d_d_t_dt=(1/(alpha*dt*dt))*(p_t_dt-p_t)-(1/(alpha*dt))*p_d_t-...
            ((1/(2*alpha))-1)*p_d_d_t;

p_d_t_dt= p_d_t+dt*(1-del)*p_d_d_t+del*dt*p_d_d_t_dt; % dp/dt at t+dt

% update d2p/dt2 at t with that value at t+dt
p_d_d_t =  p_d_d_t_dt;
update dp/dt at t with that value at t+dt                    p_d_t   =  p_d_t_dt;
% update p at t with that value at t+dt                     p_t    =   p_t_dt;

%% ------------------------------------------------------------------------
p_e=p_t;   % exact pressure
```

C.3. MATLAB® code for reconstructing conductivity in an external imaging geometry with a single target

```
% Thermo-acoustic tomography for external imaging geometry
% Reconstruction of conductivity
% Author : Sovanlal Mukherjee, Sept 2011
% Ref : Lei Yao, Gaofeng Guo and Huabei Jiang, “Quantitative
% microwave-induced thermoacoustic tomography,” Med. Phys. 37, 3752-3759 (2010).


clear all;
close all;
clc;
% Reading FEM mesh from COMSOL
%% single target
```

```
FEM_node_coord = comsol_node_read('FEM_mesh_single_target.mphtxt');        % x,y coords for each
node

conn_array_FEM = comsol_fem_node_read('FEM_mesh_single_target.mphtxt')+1;  % FEM connectivity
array

conn_array_bnd = comsol_bnd_node_read('FEM_mesh_single_target.mphtxt')+1;  % boundary
connectivity

%% initializing different parameters
eps_r=80;                                % relative permittivity
mu_r = 1;                    % relative permeability
mu_0=4*pi*1e-10;             %permeability of free space (H/mm)
eps_0= 8.854e-15;            %permittivity of free space (F/mm)
c = 3e11;                    % speed of light in free space (mm/sec)
f= 1e9;                      % frequency of operation (in Hz)
% f=9e8;
w=2*pi*f;                    % radian frequency (rad/s)
lamda = c/f;                 % wavelength (in mm)
sigma_bg= 0.1e-3;            %exact conductivity (S/mm)of the background
sigma_guess = 0.001e-3; %initial conductivity (in S/mm)

%time-stepping parameters
alpha= 0.25;
del=0.5;



T1 = 100;              %time period (us)
d_t= 1;               %time step (us)
sigma_2=1;             %Gaussian pulse width

vs= 1500e3;            %   speed of sound in water (mm/sec)
beta= 4e-4;            %   thermal coeff of vol. expansion (K^-1)
C_p= 4000;         %   specific heat capacity @const pressure (in J/(kg K))
 %% Exact electric field and Pressure

n_elem= size(conn_array_FEM,1);       %total number of elements
node= size(FEM_node_coord,1);         %total number of nodes



%distance of each boundary nodes from center
bnd_radius = (sqrt(FEM_node_coord(conn_array_bnd(:,1),1).^2+...
          FEM_node_coord(conn_array_bnd(:,1),2).^2));

a=max(bnd_radius);  %radius of the geometry

% index of the outer bnd only
index_bnd_radius = find(abs(bnd_radius-a)<1e-6);

%taking outer boundary only
conn_array_bnd_new = conn_array_bnd(index_bnd_radius,:);
```

```
n_bnd_elem= size(conn_array_bnd_new,1);

bnd_nodes= unique(conn_array_bnd_new); %Arrange boundary nodes

no_Rx= length(bnd_nodes);           %no. of acoustic detectors

rx_points= bnd_nodes;           %location of acoustic receivers

%% Exact electric field for single target
center_target=20;     %center of the target (mm)
center_bg=0;          %center of the background(mm)
rad_target=5;         %radius of the target(mm)
rad_bg=a;          %radius of the background(mm)

%% ------------------------------------------------------------------------
sigma_target=0.3e-3;       %exact conductivity (S/mm) of the target
theta=0;                   %angle of plane wave incidence

[E_z_abs_exact n_target sigma_0]=E_field_exact(FEM_node_coord,...
    conn_array_FEM,conn_array_bnd_new,lamda,...
                    eps_r,mu_r,sigma_bg,...
                    sigma_target,w,c,eps_0,center_target,...
                    center_bg,...
                    rad_target,rad_bg,theta,a);


s_0 = sigma_0.*((E_z_abs_exact).^2);   % exact power loss density


%calculating original acoustic pressure
[K M C B dB_ds P_exact P_exact_plot P_exact_Rx] =TAT_FEM_external_geom...
   (FEM_node_coord,...
   conn_array_FEM,conn_array_bnd_new,vs,C_p, beta,...
s_0,node,rx_points,a,alpha,del,T1,d_t,sigma_2);

sigma_g= sigma_guess*ones(node,1);  % assumed conductivity vector

err=[];   % initialized RMS error

%% calculating Jacobian or Sensitivity matrix

[J] =Jacobian_TAT_external_geom(K,M,C,dB_ds,alpha,...
   del,d_t,T1,sigma_2,rx_points,node);


% 2D image of power loss density and E field

node_x= FEM_node_coord(:,1);
node_y= FEM_node_coord(:,2);
node_z=zeros(size(node_x,1),1);

fwd_mesh.nodes= [node_x node_y node_z];
```

```
% fwd_mesh.elements=delaunay(node_x,node_y);
fwd_mesh.elements=conn_array_FEM;

figure;
h= trisurf(fwd_mesh.elements,...
      fwd_mesh.nodes(:,1),...
      fwd_mesh.nodes(:,2),...
      fwd_mesh.nodes(:,3),...
      E_z_abs_exact);

shading interp;
view(2);
axis equal;
axis ([-a a -a a]);
axis on;
colormap hot;
title('|Ez|','FontSize',20);
colorbar('vert');

figure;

   h1= trisurf(fwd_mesh.elements,...
      fwd_mesh.nodes(:,1),...
      fwd_mesh.nodes(:,2),...
      fwd_mesh.nodes(:,3),...
      s_0);
shading interp;
view(2);
axis equal;
axis ([-a a -a a]);
colormap hot;
title('original power loss density','FontSize',24);
colorbar('vert');
%% plotting the forward image
figure;
h2= trisurf(fwd_mesh.elements,...
      fwd_mesh.nodes(:,1),...
      fwd_mesh.nodes(:,2),...
      fwd_mesh.nodes(:,3),...
      sigma_0/1e-3);
shading interp;
view(2);
axis equal;
axis ([-a a -a a]);
colormap hot;
title('\sigma_o_r_i_g','FontSize',24);
colorbar('vert');


%% finite element model to find the pressure

for ii=1:50
```

```
%% calculated E field
k_g= ((w/c)*sqrt(eps_r-j*sigma_g/(w*eps_0)));   %initial wave number

%calculated electric field based on assumed conductivity profile

[E_z_abs_calc ]=...
E_field_calc(FEM_node_coord,conn_array_FEM,conn_array_bnd_new,lamda,...
                    eps_r,mu_r,k_g,theta,a);

%% calculate power loss density

s_c = sigma_g.*((E_z_abs_calc).^2);   % calculated power loss density

%% finite element model to find the pressure
%calculate acoustic pressure based on assumed conductivity profile
[P_calc] =TAT_FEM_1_ext_geom(FEM_node_coord,conn_array_FEM,...
                C_p,beta,s_c,node,rx_points,...
                K,M,C,alpha,del,T1,d_t,sigma_2);

%% Levenberg-Marquardt algorithm
hess= J*J';    % hessian matrix
reg=0.8;       % regularization parameter

JJ = hess+reg*eye(size(hess,1),size(hess,2));

P_diff= (P_exact-P_calc);% difference of Exact and Calculated pressure

del_s= JJ\(J*P_diff);

s_calc=s_c+del_s;   % update calculated power loss density

sigma_update= s_calc./(E_z_abs_calc.^2);% update conductivity
sigma_g= sigma_update;

err_rms= sqrt(sum(((sigma_0-sigma_g)./sigma_0).^2)/node)   % RMS error

err=[err err_rms];

 if err_rms<=0.04

    break;

 end
 ii
end

%% plotting reconstructed conductvity
figure;
h= trisurf(fwd_mesh.elements,...
       fwd_mesh.nodes(:,1),...
       fwd_mesh.nodes(:,2),...
       fwd_mesh.nodes(:,3),...
```

```
        sigma_g/1e-3);
shading interp;
view(2);
axis equal;
axis ([-a a -a a]);
colormap hot;
title('\sigma_r_e_c_o_n','FontSize',24);
colorbar('vert');

%% plotting reconstructed power loss density
figure;
h= trisurf(fwd_mesh.elements,...
        fwd_mesh.nodes(:,1),...
        fwd_mesh.nodes(:,2),...
        fwd_mesh.nodes(:,3),...
        s_calc);
shading interp;
view(2);
axis equal;
axis ([-a a -a a]);
colormap hot;
title('reconstructed power loss density','FontSize',24);
colorbar('vert');
```

Subroutine Jacobian_TAT_external_geom

```
% this code calculates Jacobian

function [J] =Jacobian_TAT_external_geom(K,M,C,dB_ds,alpha,...
    del,d_t,T1,sigma_2,rx_points,node);

%% finite element model to find Jacobian

 dp_ds_t= zeros(node,node);
 dp_d_ds_t = zeros(node,node);
 dp_d_d_ds_t= zeros(node,node);

 J=[];




for t=0:d_t:T1

 S_t= exp((-(t-T1/4)^2)/(2*sigma_2));  % Gaussian source
 S_d_t= -1e6*S_t*(t-(T1/4))/sigma_2; % differentiated Gaussian source

%% --Newmark's time stepping algorithm-------------------------------------
    dt=d_t*1e-6;       % time steps in second

    m1= K+(1/(alpha*dt*dt))*M+(del/(alpha*dt))*C;
```

```
    m2_ds=(1/(alpha*dt*dt))*dp_ds_t+(1/(alpha*dt))*dp_d_ds_t+...
       ((1/(2*alpha))-1)*dp_d_d_ds_t;

    m3_ds= (del/(alpha*dt))*dp_ds_t+((del/alpha)-1)*dp_d_ds_t+...
       ((del/(2*alpha))-1)*dt*dp_d_d_ds_t;

   dB_ds_t_dt= dB_ds*2*S_t*S_d_t;   % dB/ds at t+dt

   dp_ds_t_dt = m1\(dB_ds_t_dt+M*m2_ds+C*m3_ds); % dp/ds at t+dt

   % (d/ds)(d2p/dt2)at t+dt
   dp_d_d_ds_t_dt=(1/(alpha*dt*dt))*(dp_ds_t_dt-dp_ds_t)-...
       (1/(alpha*dt))*dp_d_ds_t-...
       ((1/(2*alpha))-1)*dp_d_d_ds_t;

   % (d/ds)(dp/dt) at t+dt
   dp_d_ds_t_dt= dp_d_ds_t+dt*(1-del)*dp_d_d_ds_t...
              +del*dt*dp_d_d_ds_t_dt;

    %update(d/ds)(d2p/dt2) at t with that value at t+dt
    dp_d_d_ds_t =  dp_d_d_ds_t_dt;
    %update (d/ds)(dp/dt) at t with that value at t+dt
    dp_d_ds_t   =  dp_d_ds_t_dt;
    %update dp/ds at t with that value at t+dt
    dp_ds_t    =   dp_ds_t_dt;
%% ------------------------------------------------------------------------
    dp_ds=dp_ds_t(:,rx_points);   %extracting dp/ds at receivers

    J=[J dp_ds];   % accumulating Jacobian for all time steps

 end
```

Subroutine E_field_calc

```
% Calculating TM wave electric field
% for a dielectric cylinder with an
% incident uniform plane wave

%Bayliss-Turkel RBC is considered here

% Author : Sovanlal Mukherjee, April,2011

%Ref : A. F. Peterson and S. V. Castillo, "A frequency-domain differential equation
% formulation for electromagnetic scattering from inhomogeneous cylinders,"
% IEEE Trans. Antennas Propag. 37, 601–607 (1989).

function [E_z_abs]= E_field_calc(FEM_node_coord,conn_array_FEM,conn_array_bnd_new,lamda,...
                    eps_r,mu_r,k_g,theta,a);

%% FEM algorithm

n_elem = size(conn_array_FEM,1);     %total number of elements
n_node = size(FEM_node_coord,1);     %total number of nodes
```

```
n_bnd_elem=size(conn_array_bnd_new,1);%total number of boundary elements

% initialize FEM matrices
AA = zeros(n_node,n_node);
I1 = zeros(n_node,n_node);

b= zeros(n_node,1);

% FEM algorithm
for elem = 1:n_elem

   %reading 3 local nodes of each element
   n1 = conn_array_FEM(elem,1);
   n2 = conn_array_FEM(elem,2);
   n3 = conn_array_FEM(elem,3);

   % x, y coordinates of 3 local nodes

   x1=FEM_node_coord(n1,1);
   y1=FEM_node_coord(n1,2);

   x2=FEM_node_coord(n2,1);
   y2=FEM_node_coord(n2,2);

   x3=FEM_node_coord(n3,1);
   y3=FEM_node_coord(n3,2);

  %calculating coeffs of basis function
   b1= y2-y3;
   b2= y3-y1;
   b3= y1-y2;

   c1= x3-x2;
   c2= x1-x3;
   c3= x2-x1;

   % area of the triangular element

   delta= 0.5*abs(b1*c2-b2*c1);

   % FEM matrices

  A1 = (1/mu_r)*(1/(4*delta))*[b1^2+c1^2   b1*b2+c1*c2 b1*b3+c1*c3;...
                        b2*b1+c2*c1 b2^2+c2^2   b2*b3+c2*c3;...
                        b3*b1+c3*c1 b3*b2+c3*c2 b3^2+c3^2];

%     A2 = ((k.^2)*eps_r*delta/12)*[2 1 1;1 2 1;1 1 2];

   A2_n1= (k_g(n1)^2*(delta/60))*[6 2 2;2 2 1;2 1 2];
   A2_n2= (k_g(n2)^2*(delta/60))*[2 2 1;2 6 2;1 2 2];
   A2_n3= (k_g(n3)^2*(delta/60))*[2 1 2;1 2 2;2 2 6];
  A2= A2_n1+A2_n2+A2_n3;
```

```
    A11 = A1-A2;

    % assembling the matrix

    AA(n1,n1) = AA(n1,n1)+A11(1,1);
    AA(n1,n2) = AA(n1,n2)+A11(1,2);
    AA(n1,n3) = AA(n1,n3)+A11(1,3);

    AA(n2,n1) = AA(n2,n1)+A11(2,1);
    AA(n2,n2) = AA(n2,n2)+A11(2,2);
    AA(n2,n3) = AA(n2,n3)+A11(2,3);

    AA(n3,n1) = AA(n3,n1)+A11(3,1);
    AA(n3,n2) = AA(n3,n2)+A11(3,2);
    AA(n3,n3) = AA(n3,n3)+A11(3,3);


end

    %% solving the boundary integral

    % calculating the coeffs of Bayliss-Turkel RBC

    for mm= 1:n_bnd_elem

    % 2 nodes of each boundary element
    n1_bnd = conn_array_bnd_new(mm,1);
    n2_bnd = conn_array_bnd_new(mm,2);

    k_bnd=(k_g(n1_bnd)+k_g(n2_bnd))/2;
    alpha_num = -j*k_bnd-(3/(2*a))+(j*3/(8*k_bnd*a^2));
    alpha_den = 1-(j/(k_bnd*a));

    alpha = alpha_num/alpha_den;
    beta_num=-(j/(2*k_bnd*a^2));
    beta_den = 1-(j/(k_bnd*a));

    beta =beta_num/beta_den;
    % x,y coords of each boundary nodes
    x1_bnd=FEM_node_coord(n1_bnd,1);
    y1_bnd=FEM_node_coord(n1_bnd,2);

    x2_bnd=FEM_node_coord(n2_bnd,1);
    y2_bnd=FEM_node_coord(n2_bnd,2);

    % phase angle of each boundary nodes

    phi1 = angle(x1_bnd+1j*y1_bnd);

    phi2 = angle(x2_bnd+1j*y2_bnd);
```

```
% making sure 0<=phi<=2*pi
 if phi1<0

   phi1=2*pi-abs(phi1);
end

 if phi2<0

   phi2=2*pi-abs(phi2);

 end

 % Orientation of phi (anti-clockwise, increasing order)
 if phi2==0 && phi1>3*pi/2
 phi2= 2*pi;
 end
 if phi2~=0 || (phi2==0 && phi1<pi/2)
 Phi=[phi1,phi2];
 Phi_sort= sort(Phi);
 phi1=Phi_sort(1);
 phi2= Phi_sort(2);
 end
 if phi1==0 && phi2>3*pi/2

    phi1=phi2;
    phi2=2*pi;
 end

 w =(phi2-phi1);

% FEM matrices on boundary
A_pq_3 =alpha*a*w*[1/3 1/6;1/6 1/3];

A_pq_4 =beta*a*(1/w)*[1 -1;-1 1];

A_pq = A_pq_3-A_pq_4;

% assembly of boundary matrix

I1(n1_bnd,n1_bnd) =I1(n1_bnd,n1_bnd)+A_pq(1,1);
I1(n1_bnd,n2_bnd) =I1(n1_bnd,n2_bnd)+A_pq(1,2);
I1(n2_bnd,n1_bnd) =I1(n2_bnd,n1_bnd)+A_pq(2,1);
I1(n2_bnd,n2_bnd) =I1(n2_bnd,n2_bnd)+A_pq(2,2);

% calculating source terms

b1= source_term_test1(phi1,phi2,k_bnd,theta,beta,alpha,a);
b2=source_term_test2(phi1,phi2,k_bnd,theta,beta,alpha,a);

% assembly of source matrix
b(n1_bnd)=b(n1_bnd)+b1;
b(n2_bnd)=b(n2_bnd)+b2;
end
```

```
  %% Calculating E Field
E_z = (AA-I1)\b;        %total electric field

E_z_abs = abs(E_z);     %magnitude of electric field
```

Subroutine TAT_FEM_1_ext_geom

```
function [P_calc] =TAT_FEM_1_ext_geom(FEM_node_coord,conn_array_FEM,...
                    C_p, beta,s_c,...
                    node,rx_points,K,M,C,alpha,del,T1, d_t,sigma_2);

%% finite element model to find the pressure
n_elem= size(conn_array_FEM,1);

B_c= zeros(node,1);

for elem = 1:n_elem

   %reading 3 local nodes of each element
   n1 = conn_array_FEM(elem,1);
   n2 = conn_array_FEM(elem,2);
   n3 = conn_array_FEM(elem,3);

   % x, y coordinates of 3 local nodes

   x1=FEM_node_coord(n1,1);
   y1=FEM_node_coord(n1,2);

   x2=FEM_node_coord(n2,1);
   y2=FEM_node_coord(n2,2);

   x3=FEM_node_coord(n3,1);
   y3=FEM_node_coord(n3,2);
   b1= y2-y3;
   b2= y3-y1;
   b3= y1-y2;

   c1= x3-x2;
   c2= x1-x3;
   c3= x2-x1;

   % area of the triangular element

   delta= 0.5*abs(b1*c2-b2*c1);

   % calculating individual surface matrices
   b_c_k1= (beta*delta/C_p)*(1/12)*s_c(n1)*...
   [2 1 1];
```

```
    b_c_k2= (beta*delta/C_p)*(1/12)*s_c(n2)*...
    [1 2 1];

    b_c_k3= (beta*delta/C_p)*(1/12)*s_c(n3)*...
    [1 1 2];

    b_c=sum([b_c_k1;b_c_k2;b_c_k3],2);

    B_c(n1)=B_c(n1)+b_c(1);
    B_c(n2)=B_c(n2)+b_c(2);
    B_c(n3)=B_c(n3)+b_c(3);
end
%% calculating acoustic pressure in time domain

 p_t_c= zeros(node,1);
 p_d_t_c = zeros(node,1);
 p_d_d_t_c= zeros(node,1);

 P_calc=[];


 for t=0:d_t:T1

 S_t= exp((-(t-T1/4)^2)/(2*sigma_2));    % Gaussian source
 S_d_t= -1e6*S_t*(t-(T1/4))/sigma_2;   % differentiated Gaussian source

 dt=d_t*1e-6;                    % time steps in second
  % calculate acoustic pressure based on assumed conductivity profile
     [p_t_calc p_d_t_calc p_d_d_t_calc]= pressure_c...
     (B_c,K,M,C,del,alpha,dt,S_t,S_d_t,p_t_c,p_d_t_c,p_d_d_t_c);

    p_t_c= p_t_calc;      %update p at t with that value at t+dt
    p_d_t_c=p_d_t_calc;   %update dp/dt at t with that value at t+dt
    p_d_d_t_c=p_d_d_t_calc; update d2p/dt2 at t with that va;ue at t+dt


     p_calc=p_t_calc(rx_points); % Extract acoustic pressure at receiver points
     P_calc=[P_calc;p_calc];     % accumulating acoustic pressure at all time steps
 end
```

Subroutine pressure_c

```
% this code calculates the acoustic pressure based on
%assumed conductivity profile
function [p_o,p_d_t,p_d_d_t]=pressure_c...
    (B,K,M,C,del,alpha,dt,S_t,S_d_t,p_t,p_d_t,p_d_d_t);

     m1= K+(1/(alpha*dt*dt))*M+(del/(alpha*dt))*C;

     m2=(1/(alpha*dt*dt))*p_t+(1/(alpha*dt))*p_d_t+((1/(2*alpha))-1)*...
       p_d_d_t;
```

```
    m3= (del/(alpha*dt))*p_t+((del/alpha)-1)*p_d_t+((del/(2*alpha))-1)...
       *dt*p_d_d_t;


    %% --Newmark's time stepping algorithm----------------------------------

    B_t_dt= B*2*S_t*S_d_t;     %B at t+dt


    p_t_dt = m1\(B_t_dt+M*m2+C*m3);  % p at t+dt


% d2p/dt2 at t+dt
  p_d_d_t_dt=(1/(alpha*dt*dt))*(p_t_dt-p_t)-(1/(alpha*dt))*p_d_t-...
             ((1/(2*alpha))-1)*p_d_d_t;

% dp/dt at t+dt
  p_d_t_dt= p_d_t+dt*(1-del)*p_d_d_t+del*dt*p_d_d_t_dt;

% update d2p/dt2 at t with that value at t+dt
  p_d_d_t =  p_d_d_t_dt;
% update dp/dt at t with that value at t+dt
  p_d_t   =  p_d_t_dt;
% update p at t with that value at t+dt
  p_t     =  p_t_dt;

%% ------------------------------------------------------------------------
    p_o=p_t;              % calculated acoustic pressure
```

C.4. MATLAB® code for reading COMSOL® mesh

```
% clc;clear;
function data=comsol_node_read(filename)
fid=fopen(filename);

%nodes coord starts
start='# Mesh point coordinates';
finish='';

data=[];

sta=0;%status flag
i=1;

while(not(feof(fid)))
   if sta==0
      line=fgetl(fid);
      if isequal(start,line)
         sta=1;
      end
   elseif sta==1
      line=fgetl(fid);
```

```
        if isequal(finish,line)
            sta=2;
        else
            data(i,:)=str2num(line);
            i=i+1;
        end
    elseif sta==2
        break;
    end
end

% save 'data';
```

C.5. MATLAB® code for reconstructing conductivity in an internal imaging geometry with a single target

```
%% TAT for intra-lumenal geometry
% this includes a complete circular geometry
clear all;
close all;
clc;

%% read the mesh from COMSOL

x_target=0;
y_target=25;    %distance of target from the center of inner region
a_in_bnd= 10;   %radius of inner region
rad_target=3;   %radius of target
center_out_bnd=0;  %center (0,0) of outer boundary
sigma_target=0.608e-3; %exact conductivity (S/mm) of the target
sigma_bg= 1.216e-3;    %exact conductivity (S/mm)of the background
sigma_guess = 0.001e-3; %initial conductivity (S/mm)


FEM_node_coord = comsol_node_read...
('FEM_mesh_single_target_12_mm_depth.mphtxt');% x,y coords for each node

conn_array_FEM = comsol_fem_node_read...
('FEM_mesh_single_target_12_mm_depth.mphtxt')+1; % FEM connectivity array

conn_array_bnd =...
comsol_bnd_node_read('FEM_mesh_single_target_12_mm_depth.mphtxt')+1;

% boundary connectivity array

%% ---------------------------------------------------------------------
% distance of each nodes from center(0,0)
rho= (sqrt(FEM_node_coord(:,1).^2+...
        (FEM_node_coord(:,2)-center_out_bnd).^2));

% distance of each boundary nodes from center (0,0)
bnd_radius = (sqrt(FEM_node_coord(conn_array_bnd(:,1),1).^2+...
```

```
        (FEM_node_coord(conn_array_bnd(:,1),2)-center_out_bnd).^2));

x_coord=FEM_node_coord(:,1); % x-coordinate of each nodes
y_coord= FEM_node_coord(:,2); % y-coordinate of each nodes

a_out_bnd =max(rho);    %radius (mm) of the outer boundary
source_pos=a_in_bnd;

%% find the nodes on inner and outer boundary
index_out_bnd_radius = find(abs(bnd_radius-a_out_bnd)<1e-6);
index_in_bnd_radius = find(abs(bnd_radius-a_in_bnd)<1e-6);
% boundary connectivity array for outer bnd
conn_array_out_bnd = conn_array_bnd(index_out_bnd_radius,:);
% boundary connectivity array for inner bnd
conn_array_in_bnd = conn_array_bnd(index_in_bnd_radius,:);
conn_array_rx_point=unique(conn_array_in_bnd);

%% if rx placed over the inner half-annular region
% bnd_rx=y_coord(conn_array_rx_point);
% rx_points= conn_array_rx_point(bnd_rx>=0);

%% if rx placed over the entire inner annular region
rx_points= conn_array_rx_point;

%% initializing different parameters

eps_r =60.5;          %relative permittivity of target
eps_bg=60.5;          %relative permittivity of background
mu_r = 1;           %relative permeability
mu_0=4*pi*1e-10;     %permeability of free space (H/mm)
eps_0= 8.854e-15;    %permittivity of free space (F/mm)
c = 3e11;           %speed of light in free space (mm/sec)
f= 9.15e8;            %frequency of operation (in Hz)
w=2*pi*f;           %radian frequency (rad/s)
lamda = c/f;        %wavelength (in mm)



vs= 1500e3;         %speed of sound in water (mm/sec)
beta= 4e-4;         %thermal coeff of vol. expansion (K^-1)
C_p= 4000;        %specific heat capacity @const pressure (in J/(kg K))

%time-stepping parameters
alpha= 0.25;
del=0.5;

T1 = 100;         %time period (us)
d_t= 1;           %time step (us)

sigma_2=1;        % variance(sigma^2)of Gaussian source

%angle of plane wave incidence
theta= 3*pi/2;
```

```
sigma_0=[];

node= size(FEM_node_coord,1);                                   %total number of nodes

sigma_g= sigma_guess*ones(node,1);

err=[];

%% calculating original E field and acoustic pressure
%% for single target
%calculating original E-field
[E_z_abs n11 sigma]= E_exact_prostate_updated(FEM_node_coord,...
    conn_array_FEM,conn_array_out_bnd,conn_array_in_bnd,...
    lamda,x_target,y_target,...
    rad_target, eps_r,eps_bg,mu_r,sigma_bg,sigma_target,w,c,eps_0,a_out_bnd,rho,...
    source_pos,theta);


s_0 = sigma.*((E_z_abs).^2);     %original power loss density

%calculating original acoustic pressure

[K M C B dB_ds P_e P_exact_plot P_exact_Rx] =TAT_FEM(FEM_node_coord,...
    conn_array_FEM,conn_array_out_bnd,conn_array_in_bnd,vs,C_p, beta,...
    s_0,node,rx_points,a_out_bnd,a_in_bnd,alpha,del,T1, d_t,sigma_2);

E_z_abs_exact=E_z_abs;
P_exact=P_e;
sigma_0= sigma;


%% Imaging E-field,original conductivity and absorbed energy density/
%% power loss profile

z_coord=zeros(length(x_coord),1);

fwd_mesh.nodes= [x_coord y_coord z_coord];
fwd_mesh.elements=conn_array_FEM;

% imaging E-field
figure;

h= trisurf(fwd_mesh.elements,...
       fwd_mesh.nodes(:,1),...
       fwd_mesh.nodes(:,2),...
       fwd_mesh.nodes(:,3),...
       E_z_abs_exact(:,1));
shading interp;
view(2);
axis equal;
axis ([-a_out_bnd a_out_bnd -a_out_bnd a_out_bnd]);
xlabel('x(mm)','Fontsize', 24);
ylabel('y(mm)','Fontsize', 24);
```

```
colormap hot;
title('Exact E-field','FontSize',24);
colorbar('vert');

% imaging Original conductivity profile

 figure;
   h= trisurf(fwd_mesh.elements,...
       fwd_mesh.nodes(:,1),...
       fwd_mesh.nodes(:,2),...
       fwd_mesh.nodes(:,3),...
       s_0);
shading interp;
view(2);
axis equal;
axis ([-a_out_bnd a_out_bnd -a_out_bnd a_out_bnd]);
xlabel('x(mm)','Fontsize', 24);
ylabel('y(mm)','Fontsize', 24);
colormap hot;
title('Absorbed energy','FontSize',24);
colorbar('vert');

% imaging original absorbed energy density/power loss profile
figure;
h= trisurf(fwd_mesh.elements,...
       fwd_mesh.nodes(:,1),...
       fwd_mesh.nodes(:,2),...
       fwd_mesh.nodes(:,3),...
       sigma(:,1)/1e-3);
shading interp;
view(2);
axis equal;
axis ([-a_out_bnd a_out_bnd -a_out_bnd a_out_bnd]);
xlabel('x(mm)','Fontsize', 24);
ylabel('y(mm)','Fontsize', 24);
colormap hot;
title('\sigma_o_r_i_g','FontSize',24);
colorbar('vert');

%% finding Jacobian
%
 [J] =Jacobian_TAT(K,M,C,dB_ds,alpha,...
    del,d_t,T1,sigma_2,rx_points,node);
%
hess= J*J';               %hessian matrix
reg= 0.01;
% %% calculated E field

for ii=1:50

%% calculated E field
eps_complex=eps_bg-(j*sigma_g/(w*eps_0));  %complex permittivity
k_0= w/c;                          %wave number of free space
```

```
k_g= k_0*sqrt(eps_complex);              %initial wave number

%calculating E-field
[E_z_abs_calc ]=...
E_field_calc_prostate_updated(FEM_node_coord,conn_array_FEM,...
conn_array_out_bnd,...
lamda,conn_array_in_bnd,rad_target,...
eps_r,mu_r,k_g,a_out_bnd,source_pos,w,c,k_0,eta,theta);


%% calculate power loss density

s_c = sigma_g.*(E_z_abs_calc.^2);  %calculated power loss density
%% finite element model to find the pressure
%calculate acoustic pressure
[P_cal] =TAT_FEM_1(FEM_node_coord,conn_array_FEM,...
                   C_p,beta,s_c,node,rx_points,...
                   K,M,C,alpha,del,T1,d_t,sigma_2);
P_calc=P_cal;

%calculate the difference between exact and calculated pressure
P_diff= (P_exact-P_calc);

%Regularize hessian matrix
JJ = hess+reg*eye(size(hess,1),size(hess,2));
 del_s= JJ\(J*P_diff);     %calculate update vector

 s_calc=s_c+del_s;         %update power loss density

 sigma_update= s_calc./(E_z_abs_calc.^2);  %update conductivity
 sigma_g= sigma_update;


err_rms= sqrt(sum(((sigma-sigma_g)./sigma).^2)/node) %calculate RMS error


 err=[err err_rms];

 if err_rms<=0.04                %stopping criterion

    break;

 end
 ii
end
%% plotting the inverse image

% imaging reconstructed conductivity profile
figure;
h= trisurf(fwd_mesh.elements,...
       fwd_mesh.nodes(:,1),...
       fwd_mesh.nodes(:,2),...
```

```
        fwd_mesh.nodes(:,3),...
        sigma_g/1e-3);
shading interp;
view(2);
axis equal;
axis ([-a_out_bnd a_out_bnd -a_out_bnd a_out_bnd]);
xlabel('x(mm)','Fontsize', 24);
ylabel('y(mm)','Fontsize', 24);
colormap hot;
title('\sigma_r_e_c_o_n','FontSize',24);
colorbar('vert');

% imaging reconstructed power-loss/absorbed energy profile
figure;
h= trisurf(fwd_mesh.elements,...
        fwd_mesh.nodes(:,1),...
        fwd_mesh.nodes(:,2),...
        fwd_mesh.nodes(:,3),...
        s_calc);
shading interp;
view(2);
axis equal;
axis ([-a_out_bnd a_out_bnd -a_out_bnd a_out_bnd]);
xlabel('x(mm)','Fontsize', 24);
ylabel('y(mm)','Fontsize', 24);
colormap hot;
title('reconstructed energy density','FontSize',24);
colorbar('vert');
```

VITA

Sovanlal Mukherjee

Candidate for the Degree of

Doctor of Philosophy

Thesis: AN IN-SILICO STUDY OF THERMO-ACOUSTIC COMPUTED TOMOGRAPHY FOR EXTERNAL AND INTERNAL IMAGING GEOMETRY

Major Field: Electrical Engineering

Biographical:

Education:

Completed the requirements for the Doctor of Philosophy in Electrical Engineering at Oklahoma State University, Stillwater, Oklahoma in December, 2013.

Completed the requirements for the Master of Science in Electrical Engineering at Indian Institute of Technology, Kanpur, India in 2005.

Completed the requirements for the Bachelor of Science in Electronics and Communication Engineering at University of Burdwan, Burdwan, India in 2002.

Experience:

Research Scholar, Oklahoma State University, Stillwater, OK, 2008-2013.
Teaching Assistant, Oklahoma State University, Stillwater, OK, 2008-2013.
Project Engineer, Wipro Technology, Bangalore, India, 2005-2007.
Graduate Assistant, Indian Institute of Technology, Kanpur, India, 2003-2005.

Professional Memberships:

Student Member: SPIE, Optical Society of America (OSA).
Member of Honor Societies: Phi Kappa Phi, Eta Kappa Nu.